國立台灣大學工程學院土木工程學系

碩士論文

Department of Civil Engineering

College of Engineering

National Taiwan University

Master Thesis

利用空間位移訊號進行結構局部／系統損壞評估

Application of Spatial Displacement Measurement on Damage

Assessment from both Local and Global Structural System

李其航

Chi-Hang Li

指導教授：羅俊雄 教授

Advisor: Chin-Hsiung Loh, Ph.D.

中華民國 101 年 6 月

June, 2012

國立臺灣大學碩士學位論文
口試委員會審定書

利用空間位移訊號進行結構局部／系統損壞評估
Application of Spatial Displacement Measurement
for Local Damage Assessment of Structural System

本論文係李其航君（R99521224）在國立臺灣大學土木工
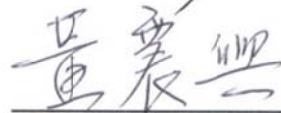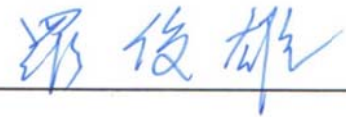程學系碩士班完成之碩士學位論文，於民國 101 年 06 月 26
日承下列考試委員審查通過及口試及格，特此證明

口試委員：

羅　俊　雄 （指導教授）	*(簽名)*
田　堯彰	*(簽名)*
黃　震　興	*(簽名)*

系主任　　　呂　良　正　　　　*(簽名)*

（簽名）

i

Acknowledgement

本論文得以順利完整，首先要感謝恩師　羅俊雄教授的細心指導與教誨。承蒙老師在學業上不厭其煩地提供的建議與幫助，學生在此向羅老師致上由衷的謝意。另外也感謝　田堯彰教授與　黃震興教授於論文口試期間不吝指正並提供寶貴建議，使本研究內容在最終能更加充實完整，在此特別致謝。

研究期間，感謝學長趙書賢、盧恭君在研究遇到難題時給予的各項協助。也感謝同窗陳明徹、陳立豪、杜進國在學習過程中互相扶持與鼓勵。以及學弟曾敏軒和劉建榮在研究上提供的幫忙。另外在求學期間還有許多值得感謝的人，礙於篇幅無法一一列舉，但真的發自內心感謝你們。

最後要特別感謝我親愛的家人，多謝你們在背後的支持，使得我能無後顧之憂地專心求學與研究，僅以本文獻給你們表達我的感謝之意。

Abstract (in Chinese)

　　現今結構物健康監測技術多經由普通接觸式量測計（如：加速度規、速度規…等）裝設於結構物量取反應訊號進行分析判斷。為獲取結構細部反應資訊而大量安裝儀器的情況下，此種量測法將會有佈線繁雜以及裝設位置選項過少等問題產生。然而受惠於光學科技之進步，此問題可有效解決。光學量測方法是將待量測位置標示上一可經由影像辨識之目標點，藉由攝影裝置觀測目標移動情況進行三維動態分析。只要目標位於裝置監控範圍內，此方法將能進行大規模位置點計算。

　　本研究重點在探討此光學量測位移訊號應用於結構系統識別及破壞診斷的適用性。分析方法分為兩大類。第一類是整體系統識別方法，對於 1.只需結構反應的斜方差型隨機子空間識別 (Covariance driven Stochastic Subspace Identification, SSI-COV)，和 2.需系統輸入輸出資訊的子空間識別 (Subspace Identification, SI) 作探討，應用光學多維訊號進行自然頻率與阻尼比分析。再來是研究 3.主成分分析 (Principal component analysis, PCA) 應用此訊號進行結構模態識別。第二類是局部系統評估，在將光學量測點網格化為數個單元後，應用幾何分析概念進行 4.奇異譜分析 (Singular spectral analysis, SSA) 獲取單元之主要動態做進一步幾何處理。另外應用 5.連續小波轉換 (Continuous Wavelet Transform, CWT) 分析訊號不連續性，對破裂做動時間點進行判斷。單元也可由 6.有限元素法 (Finite element method, FEM) 計算其應變動態行為。本研究將會針對單層雙垮鋼筋混凝土桁架的振動台實驗進行實際應用。此實驗使用集成式光學量測儀器 DMM (Dynamic Measuring Machine) 量測中間柱三維位移訊號。分析結果顯示應用此種空間位移訊號，整體系統識別方法可有效的獲取結構物資訊，並對結構變化進行描述；網格化之動態行為分析也能為結構局部破壞提供重要資訊。

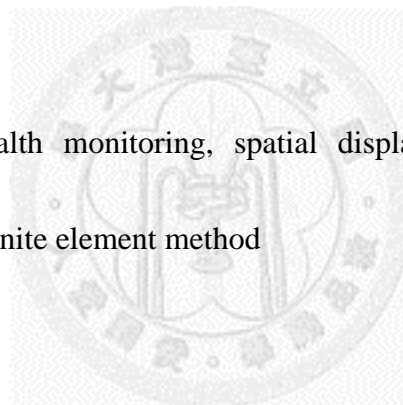**關鍵詞：**結構健康監測、空間位移、訊號處理、奇異譜分析、有限元素

Abstract

In this research, the capability of advance spatial displacement measurement for structural health monitoring (SHM) is studied. The method for obtaining this kind of data is different from regular measuring system. It utilizes the optical processing technique to calculate the specific particles' locations (called targets) within an image. While taking image and compute the locations over time, the dynamic motion can be estimated. This research employed the three dimensional displacement from optical sensors to identify system and perform damage assessment.

The applied signal analysis methodologies can separate into two categories, global system identification and local element motion detection. For global system, two subspace methods including 1.covariance-driven stochastic subspace identification (SSI-COV) and 2.recursive subspace identification (RSI) are examined. They can obtain the system natural frequency and damping ratio based on different condition. The other method is 3.principal component analysis (PCA), which the system normal modes can be briefly calculated while the measured locations are distributed along the system. For local motion, we can discretize the targets into a set of local elements. These elements motion is detect by 4.singular spectral analysis (SSA), 5.continuous wavelet transform (CWT), and 6.finite element method (FEM). The extracted information is used to

describe the structural local properties and detect the damage occurrence. To examine the applications of these methodologies on real three dimensional displacement data, a shake table test of one-story two-bay RC frame performed in the NCREE is selected. This experiment installed a totally integrated optical measuring system (DMM, by NDI Inc.) on its central column to obtain the displacement. The analysis results show that this kind of data is capable for system identification, and the detection of damage is also feasible. Detail analyzes the discrete elements. The damage location may be obtained.

Keywords: Structural Health monitoring, spatial displacement, signal processing, singular spectral analysis, finite element method
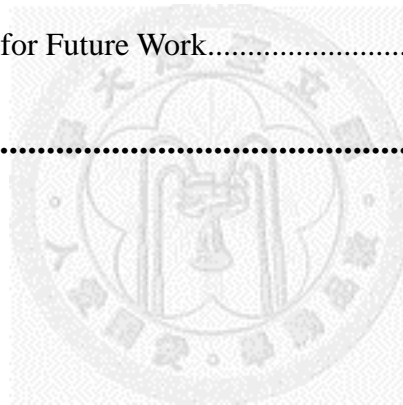
Contents

Table List

Figure List

Chapter 1. Introduction

1.1 Motivation

Structure health monitoring (SHM) has become more and more important in the civil engineering structure. Since the structures are deteriorated under service condition, it is recommended observing the structure health over time. The structure dynamic response measurement is very useful information. These measured signals contain the system response properties. Base on signal processing techniques, one can extract the signal feature for structure health monitoring and damage assessment.

The vibration-based SHM framework not only relies on the signal processing techniques but also the sensor arrangement. The recent structure measuring system utilizes normal contact sensors, for example accelerometers, placed on specific locations to represent the structure DOFs. These locations are mostly selected the floor slabs according to structural analysis concept. But if we want a more detail information within the floors, these sensors are not suitable because of installation difficulty. A measuring technique on this kind of location is needed. We discover that a novel technique utilized the optical processing method can measure particles' motions within an image over time with a reliability accuracy. This optical measuring technique can

implement on the locations that the normal contact sensors are difficult to install. Therefore, we can extract both global and local information from the structure by combining the optical and normal contact sensors.

These optical sensors are distributed within a region of local structure. The research on the application of presents signal processing techniques is needed. It is believed that the measured information can be used to identify the system and perform local damage assessment for structure health monitoring.

1.2 Literature Review

There have already lots of researches of signal processing methodologies on damage detection and system identification. Science the optical measuring system measures a large amount of sensor locations over time, methodologies with multivariate techniques are more suggested in this research.

For system identification, the subspace identification method is proved that its capability to observe the structure characteristics [15, 26]. With recursive updating the measurement data, an on-line system monitoring is obtained. Moreover, the method relies on the singular value decomposition (SVD). Since the system information is contained in the singular vectors of SVD, damage assessment can achieve by observing

the vector space expanded by singular vectors. There are researches utilize the space projection theorem to detect damage according to the change point of dataset [17, 23].

The principal component analysis (PCA) is another signal feature extraction technique. It is one of the well-known methods for multivariate analysis. Originally, the PCA are used to perform data compression [18]. Feeny [7] conducted the applicability of structural dynamic response with PCA to real experiment test. It is proved that PCA has the ability to express the structural normal modes under some condition [3]. While the sensors are arrange into an array form, the PCA can be applied on the data to detect the damage location [5]. The advantage is that the PCA is straight forward and has capability for nonlinear applications.

The singular spectral analysis (SSA) can extract not only features of one signal but also mutual features of signals with multivariate. It has been proved that it can decompose the data into trend, harmonic wave, and noise term [24]. The SSA has a widely application. In the civil engineering scope, there are studies on the analysis of seismic response data [11, 21] to grab site vibration information. The concept of SSA is relative to PCA. It is like analysis the signal with the embedding theorem [20] using PCA. And the decomposed results are the signal principal feature that can represent the original signal.

The analysis methods mentioned above are capable for multivariate data analysis. But they are still some processes need to study for the real application on damage assessment with the array of optical sensors. The explanation is in remaining chapters.

1.3 Research Objective

The objective of this research is to conduct a survey on the applications of the spatial displacement data and provides to a series of shake table test of the RC frame to check the capability. The displacement data measure the structure three dimensional motions over time with large amount of the sensing locations. It is expected that one can perform the system identification and detect the damage using this detail spatial displacement information.

The organization of this research is briefly described as follows:

Chapter 1: Describe the research motivation and literature review of some present system identification and damage assessment techniques.

Chapter 2: Introduce the signal processing methodologies used in this research. The introduced methodologies can perform system identification and feature extraction on the spatial displacement data.

Chapter 3: Perform the methods on the seismic response of a one-story two-bay RC frame. The analysis is separated into two categories: global system identification and local motion detection. The selected parameters and results of each method are discussed. Finally, the analysis results will be compared to each other.

Chapter 4: Summaries for the use of the proposed techniques are listed in this chapter, and the potential research topics are indicated at the end.

Chapter 2. Signal Analysis Methodology

2.1 Introduction

In this chapter, the algorithm of signal analysis methodologies used in this research will be introduced. These methodologies are separated into two categories according to their application, which are global system characteristics identification and local element motion analysis. After introduction, all of the analysis methodologies will be applied on the spatial displacement signals acquired from the experiment mentioned in the next chapter to identify the system parameters and detect the damage occurrence.

2.2 Global System Characteristics Identification

Nowadays, there are several signal processing techniques can perform global system characteristics identification. These methods can be categorized into parametric and non-parametric methods, or model based and non-model based. To choose reliable methods for this study, there are three different methods are selected. Two of them are subspace methods (SSI-COV and RSI) based on the discrete time state space model and can identify system natural properties including frequency, damping, and mode shape. The other is principal component analysis (PCA) which is a time series decomposition

technique that can briefly obtain the system normal modes. Detail introductions of these methodologies are mentioned in the following sections.

2.2.1 Covariance-Driven Stochastic Subspace Identification (SSI-COV)

The SSI-COV algorithm is an expansion of the stochastic subspace identification (SSI) technique which identifies stochastic state space model using output only data. Instead of the original SSI algorithm [22, 26], the SSI-COV calculates the system via assemble of block covariance matrices. Since these SSI algorithms based on concepts from linear algebra, state space model, and statistics, they have been proven to perform on the structure identification [15, 28]. Only one restrict of the SSI based algorithms is the output measurement should be ambient response of structure because of the assumption of noise input. The derivation of SSI-COV is as follows:

Stochastic Discrete Time State Space Model

For a system motion equation $\mathbf{M\ddot{x}} + \mathbf{C\dot{x}} + \mathbf{Kx} = \mathbf{F} = \mathbf{Lu}$, where $\mathbf{M}$, $\mathbf{C}$, and $\mathbf{K} \in \mathbb{R}^{n \times n}$ are system mass, damping and stiffness matrix; $\mathbf{x} \in \mathbb{R}^{n \times 1}$ and $\mathbf{u} \in \mathbb{R}^{m \times 1}$ are displacement and input force vector; n and m represent number of DOFs and number of inputs. The state space equation is written as

$$\mathbf{\dot{X}}(t) = \mathbf{A}_c \mathbf{X}(t) + \mathbf{B}_c \mathbf{u}(t), \tag{2.1}$$

$$\mathbf{A}_c = \begin{bmatrix} \mathbf{0} & \mathbf{I}_n \\ -\mathbf{M}^{-1}\mathbf{K} & -\mathbf{M}^{-1}\mathbf{C} \end{bmatrix} \in \mathbb{R}^{2n \times 2n}, \text{ and } \mathbf{B}_c = \begin{bmatrix} \mathbf{0} \\ -\mathbf{M}^{-1}\mathbf{L} \end{bmatrix} \in \mathbb{R}^{2n \times m}, \qquad (2.2)$$

where $\mathbf{X}(t) = \begin{bmatrix} \mathbf{x}^T(t) & \dot{\mathbf{x}}^T(t) \end{bmatrix}^T \in \mathbb{R}^{2n \times 1}$ is the state vector at continuous time t and

$\mathbf{A}_c(t)$, $\mathbf{B}_c(t)$ are continuous time state matrix and input matrix. If there are only l

DOFs has been measured, and the measurement response can be acceleration, velocity

or displacement. The output observation vector $\mathbf{y}(t) \in \mathbb{R}^{l \times 1}$ can be written as

$\mathbf{y}(t) = \mathbf{C}_a \ddot{\mathbf{x}}(t) + \mathbf{C}_v \dot{\mathbf{x}}(t) + \mathbf{C}_d \mathbf{x}(t)$, where $\mathbf{C}_a$, $\mathbf{C}_v$, and $\mathbf{C}_d \in \mathbb{R}^{l \times n}$ are output location

matrices. To transform $\mathbf{y}(t)$ into state space representation, it becomes

$$\mathbf{y}(t) = \mathbf{C}_c \mathbf{X}(t) + \mathbf{D}_c \mathbf{u}(t), \qquad (2.3)$$

$$\mathbf{C}_c = \begin{bmatrix} \mathbf{C}_d - \mathbf{C}_a \mathbf{M}^{-1}\mathbf{K} & \mathbf{C}_v - \mathbf{C}_a \mathbf{M}^{-1}\mathbf{C} \end{bmatrix} \in \mathbb{R}^{l \times 2n}, \text{ and } \mathbf{D}_c = \mathbf{C}_a \mathbf{M}^{-1}\mathbf{L} \in \mathbb{R}^{l \times m}. \qquad (2.4)$$

This equation is called observation equation. The $\mathbf{C}_c$ is output matrix and $\mathbf{D}_c$ is direct

transmission matrix. Since all data are measured in discrete time, Eq.(2.1) and Eq.(2.3)

need to be transformed into discrete time state space model, that is

$$\begin{aligned} \mathbf{X}_{k+1} &= \mathbf{A}_d \mathbf{X}_k + \mathbf{B}_d \mathbf{u}_k + \mathbf{w}_k, \\ \mathbf{y}_k &= \mathbf{C}_c \mathbf{X}_k + \mathbf{D}_c \mathbf{u}_k + \mathbf{v}_k, \end{aligned} \qquad (2.5)$$

with the $\mathbf{A}_d = e^{\mathbf{A}_c \Delta t}$, $\mathbf{B}_d = (\mathbf{A}_d - \mathbf{I})\mathbf{A}_c^{-1}\mathbf{B}_c$, and $\mathbf{X}_k = \mathbf{X}(k\Delta t)$. The terms $\mathbf{w}_k$ and $\mathbf{v}_k$

at the end of equations are the error from noise and measurement. If the input force

satisfies the stochastic expression, the discrete time state space mode can be further

transformed into

$$\begin{aligned} \mathbf{X}_{k+1}^s &= \mathbf{A}_d \mathbf{X}_k^s + \mathbf{w}_k^s, \\ \mathbf{y}_k^s &= \mathbf{C}_c \mathbf{X}_k^s + \mathbf{v}_k^s. \end{aligned} \qquad (2.6)$$

This equation is called stochastic state space model. The SSI-COV identifies the system

matrices ($\mathbf{A}_d$ and $\mathbf{C}_c$) of Eq.(2.6) only using the output measurement $\mathbf{y}_k^s$.

Hankel Covariance Matrix of SSI-COV

Assume the output measurement $\mathbf{y}(t)$ is $\begin{bmatrix} \mathbf{y}_1 & \mathbf{y}_2 & \cdots & \mathbf{y}_N \end{bmatrix}$, the first step of the

SSI-COV is to gather the measurement vectors into a data Hankel matrix that is

$$\begin{bmatrix} \mathbf{Y}_p \\ \hline \mathbf{Y}_f \end{bmatrix} = \begin{bmatrix} \mathbf{y}_1^s & \mathbf{y}_2^s & \cdots & \mathbf{y}_j^s \\ \mathbf{y}_2^s & \mathbf{y}_3^s & \cdots & \mathbf{y}_{j+1}^s \\ \vdots & \vdots & \ddots & \vdots \\ \mathbf{y}_i^s & \mathbf{y}_{i+1}^s & \cdots & \mathbf{y}_{i+j-1}^s \\ \hline \mathbf{y}_{i+1}^s & \mathbf{y}_{i+2}^s & \cdots & \mathbf{y}_{i+j}^s \\ \mathbf{y}_{i+2}^s & \mathbf{y}_{i+3}^s & \cdots & \mathbf{y}_{i+j+1}^s \\ \vdots & \vdots & \ddots & \vdots \\ \mathbf{y}_{2i}^s & \mathbf{y}_{2i+1}^s & \cdots & \mathbf{y}_N^s \end{bmatrix}, \tag{2.7}$$

where $\mathbf{Y}_p \in \mathbb{R}^{li \times j}$ denotes the past measurements and $\mathbf{Y}_f \in \mathbb{R}^{li \times j}$ is the future

measurements. After this, the block Toeplitz matrix is obtained by

$$\mathbf{T} = \begin{bmatrix} \mathbf{R}_i & \mathbf{R}_{i-1} & \cdots & \mathbf{R}_1 \\ \mathbf{R}_{i+1} & \mathbf{R}_i & \cdots & \mathbf{R}_2 \\ \vdots & \vdots & \ddots & \vdots \\ \mathbf{R}_{2i-1} & \mathbf{R}_{2i-2} & \cdots & \mathbf{R}_i \end{bmatrix} = \frac{1}{N} \mathbf{Y}_f \mathbf{Y}_p^T. \tag{2.8}$$

Each $\mathbf{R}_i$ defines an output covariance between two time instant with lag i.

Extended Observability Matrix and Singular Value Decomposition

According to the derivation based on stochastic properties [15], the block Toeplitz

matrix $\mathbf{T}$ can be decomposed into the multiplication of the extended observability

matrix $\mathbf{O}_i \in \mathbb{R}^{li \times 2n}$ and the reversed extended stochastic controllability matrix $\mathbf{\Gamma}_i \in \mathbb{R}^{2n \times li}$ as follows

$$\mathbf{T} = \mathbf{O}_i \mathbf{\Gamma}_i = \begin{bmatrix} \mathbf{C} \\ \mathbf{CA} \\ \vdots \\ \mathbf{CA}^{i-1} \end{bmatrix} \begin{bmatrix} \mathbf{A}^{i-1}\mathbf{G} & \cdots & \mathbf{AG} & \mathbf{G} \end{bmatrix}, \tag{2.9}$$

where the i here denotes the order of the Toeplitz matrix $\mathbf{T}$. The singular value decomposition (SVD) is utilized to perform this factorization. Representation of SVD is

$$\mathbf{T} = \mathbf{USV}^T = \begin{bmatrix} \mathbf{U}_1 & \mathbf{U}_2 \end{bmatrix} \begin{bmatrix} \mathbf{S}_1 & \mathbf{0} \\ \mathbf{0} & \mathbf{S}_2 \end{bmatrix} \begin{bmatrix} \mathbf{V}_1^T \\ \mathbf{V}_2^T \end{bmatrix} \cong \mathbf{U}_1 \mathbf{S}_1 \mathbf{V}_1^T, \tag{2.10}$$

where $\mathbf{U} \in \mathbb{R}^{li \times li}$ and $\mathbf{V} \in \mathbb{R}^{li \times li}$ are the orthogonormal matrices, and $\mathbf{S}$ is the diagonal singular values. To perform data compression from $\mathbf{USV}^T$ to $\mathbf{U}_1 \mathbf{S}_1 \mathbf{V}_1^T$, the C_{svd} defined the percentage of preservation is determined. Assume the diagonal terms of $\mathbf{S}$ are $\begin{bmatrix} s_1 & s_2 & \cdots & s_{li} \end{bmatrix}$. Size N of $\mathbf{S}_1$ is the minimum even number satisfied

$$\sum_{i=1}^{N} s_i \geq C_{svd} \times \text{trace}(\mathbf{S}). \tag{2.11}$$

After the data compression, we can compare the form between Eq.(2.9) and Eq.(2.10). The extended observability matrix $\mathbf{O}_i$ can be defined as

$$\mathbf{O}_i = \mathbf{U}_1 \mathbf{S}_1^{1/2}. \tag{2.12}$$

State Matrix and System Properties

The system matrices $\mathbf{A}_d$ and $\mathbf{C}_c$ can be easily extracted from $\mathbf{O}_i$. We can compare to Eq.(2.9) for the elements of matrix $\mathbf{O}_i$, the system matrices are

11

$$\mathbf{C}_c = \mathbf{O}_i\left(1:l,:\right),$$
$$\mathbf{A}_d = \mathbf{O}_i\left(1:l\left(i-1\right),:\right)^+ \mathbf{O}_i\left(1+l:li,:\right),$$

(2.13)

where $\left(\cdot\right)^+$ denotes pseudo inverse. As soon as the discrete state matrix $\mathbf{A}_d$ is derived, we can transform it into the continuous form $\mathbf{A}_c$ following the relation in Eq.(2.5) and apply eigen-decomposition of it that

$$\mathbf{A}_c^m = \mathbf{\Lambda} = \mathbf{\Psi}^{-1}\mathbf{A}_c\mathbf{\Psi},$$
$$\mathbf{C}_c^m = \mathbf{C}_c\mathbf{\Psi}.$$

(2.14)

The superscript m denotes the matrices in modal coordinate. Each eigenvalue λ_k in $\mathbf{\Lambda}$ is a complex number and has its conjugate value λ_k'. After eigenvalues are determined, the system natural frequency f_k and damping ratio ξ_k can be solved as

$$f_k = \frac{1}{2\pi}\sqrt{\mathrm{Re}\left(\lambda_k\right)^2 + \mathrm{Im}\left(\lambda_k\right)^2}, \text{ and } \xi_k = \frac{-\mathrm{Re}\left(\lambda_k\right)}{2\pi f_k}.$$

(2.15)

Derivation from Eq.(2.7) to Eq.(2.15) represents the SSI-COV algorithm of system identification. Flowchart of the SSI-COV algorithm can be concluded as Figure 2-1.

2.2.2 Recursive Subspace Identification (RSI)

Different from the SSI-COV based on the noise property of input data, the subspace identification (SI) method utilizes both input and output signals to perform the system identification [26]. This makes the identified system properties more reliable while the measurements are not satisfying the ambient condition. Moreover if the

12

system varies over time, the SI algorithm should analysis with a moving window to perform on-line system identification (Figure 2-2). To speed up the repeating calculation of the SI, a recursive algorithm that solves equation based on the previous information is needed. This section will explain the algorithm of the SI technique first, and then introduce the recursive algorithm of LQ factorization briefly. The procedures of the recursive-SI (RSI) are as follows:

Hankel Matrices of Subspace Identification

The origin of the SI algorithm is based on state space model shown in Eq.(2.5). Since we already defined an output data Hankel matrix Eq.(2.7) at the SSI-COV algorithm, the input data $\mathbf{u}(t)$ can also be arrange in the Hankel form that is

$$\left[\frac{\mathbf{U}_p}{\mathbf{U}_f}\right] = \begin{bmatrix} \mathbf{u}_1 & \mathbf{u}_2 & \cdots & \mathbf{u}_j \\ \mathbf{u}_2 & \mathbf{u}_3 & \cdots & \mathbf{u}_{j+1} \\ \vdots & \vdots & \ddots & \vdots \\ \mathbf{u}_i & \mathbf{u}_{i+1} & \cdots & \mathbf{u}_{i+j-1} \\ \mathbf{u}_{i+1} & \mathbf{u}_{i+2} & \cdots & \mathbf{u}_{i+j} \\ \mathbf{u}_{i+2} & \mathbf{u}_{i+3} & \cdots & \mathbf{u}_{i+j+1} \\ \vdots & \vdots & \ddots & \vdots \\ \mathbf{u}_{2i} & \mathbf{u}_{2i+1} & \cdots & \mathbf{u}_N \end{bmatrix}, \tag{2.16}$$

where $\mathbf{U}_p \in \mathbb{R}^{mi \times j}$ denotes the past input measurements and $\mathbf{U}_f \in \mathbb{R}^{mi \times j}$ is the future input measurements. Furthermore, the special Hankel matrix can be defined as

$$\mathbf{\Xi}_p = \begin{bmatrix} \mathbf{U}_p \\ \mathbf{Y}_p \end{bmatrix} \in \mathbb{R}^{(m+l)i \times j}. \tag{2.17}$$

13

Extended Observability Matrix and LQ Factorization

For system characteristics identification, the extended observability matrix $\mathbf{O}_i$ is needed. The SI algorithm utilizes both oblique projection theorem and the MOESP theorem [25] of LQ factorization to extract the matrix $\mathbf{O}_i$. The procedures are

$$\begin{bmatrix} \mathbf{U}_f \\ \mathbf{\Xi}_p \\ \mathbf{Y}_f \end{bmatrix} = \begin{bmatrix} \mathbf{L}_{1,1} & \mathbf{0} & \mathbf{0} \\ \mathbf{L}_{2,1} & \mathbf{L}_{2,2} & \mathbf{0} \\ \mathbf{L}_{3,1} & \mathbf{L}_{3,2} & \mathbf{L}_{3,3} \end{bmatrix} \begin{bmatrix} \mathbf{Q}_{1,1}^T \\ \mathbf{Q}_{2,1}^T \\ \mathbf{Q}_{3,1}^T \end{bmatrix}, \tag{2.18}$$

$$\left(\mathbf{Y}_f \big/_{\mathbf{U}_f} \mathbf{\Xi}_p \right) \Big/ \mathbf{U}_f^{\perp} = \mathbf{O}_i \tilde{\mathbf{X}}_i \Big/ \mathbf{U}_f^{\perp} = \mathbf{L}_{3,2} \mathbf{Q}_{2,1}^T, \tag{2.19}$$

$$\text{column space} \left(\mathbf{L}_{3,2} \right) = \text{column space} \left(\mathbf{O}_i \right). \tag{2.20}$$

where $\cdot/\cdot^{\perp}$ and $\cdot/\cdot$ are orthogonal projection and oblique projection operator; Eq.(2.18) is LQ factorization and Eq.(2.19) is oblique projection of Hankel matrices. According to derivation [27], the relation between the oblique projection and the LQ factorization is defined and they can connect with the extended observability matrix $\mathbf{O}_i$ in Eq.(2.19). Following this equation, only $\mathbf{L}_{3,2}$ of LQ factorization is needed for system identification. Furthermore, column space of it can obtained from SVD, that is

$$\mathbf{L}_{3,2} = \mathbf{U}\mathbf{S}\mathbf{V}^T = \begin{bmatrix} \mathbf{U}_1 & \mathbf{U}_2 \end{bmatrix} \begin{bmatrix} \mathbf{S}_1 & \mathbf{0} \\ \mathbf{0} & \mathbf{S}_2 \end{bmatrix} \begin{bmatrix} \mathbf{V}_1^T \\ \mathbf{V}_2^T \end{bmatrix} \cong \mathbf{U}_1 \mathbf{S}_1 \mathbf{V}_1^T,$$

$$\mathbf{O}_i = \mathbf{U}_1. \tag{2.21}$$

In this equation, the C_{svd} defines in Eq.(2.11) is also introduced to denoise the SVD result.

State Matrix and System Properties

After the system extended observability matrix $\mathbf{O}_i$ is obtained, the same

procedures introduced in the SSI-COV algorithm from Eq.(2.13) to Eq.(2.15) can be

applied to obtain the system natural properties. Besides, another parameter C_{omac} is

taken to filter out the noise modes. The idea is based on the matrix $\mathbf{O}_i$ can be

reconstructed from two different approaches. First is direct calculation that

$$\overline{\mathbf{O}}_i^m = \begin{bmatrix} \mathbf{C}_c^m \\ \mathbf{C}_c^m \mathbf{A}_c^m \\ \vdots \\ \mathbf{C}_c^m \left(\mathbf{A}_c^m \right)^{i-1} \end{bmatrix} = \begin{bmatrix} \overline{\boldsymbol{\varphi}}_1 & \overline{\boldsymbol{\varphi}}_2 & \cdots & \overline{\boldsymbol{\varphi}}_N \end{bmatrix}. \tag{2.22}$$

The other is based on the idea of data composition of Eq.(2.12), that is

$$\tilde{\mathbf{O}}_i^m = \mathbf{O}_i \boldsymbol{\Psi} = \mathbf{U}_1 \boldsymbol{\Psi} = \begin{bmatrix} \tilde{\boldsymbol{\varphi}}_1 & \tilde{\boldsymbol{\varphi}}_2 & \cdots & \tilde{\boldsymbol{\varphi}}_N \end{bmatrix}. \tag{2.23}$$

Therefore, the coherence between the vectors $\overline{\boldsymbol{\varphi}}_i$ and $\tilde{\boldsymbol{\varphi}}_i$ are defined as

$$\mathrm{OMAC}_i = \frac{\left| \left(\overline{\boldsymbol{\varphi}}_i^* \right)^T \tilde{\boldsymbol{\varphi}}_i \right|}{\sqrt{\left(\overline{\boldsymbol{\varphi}}_i^* \right)^T \overline{\boldsymbol{\varphi}}_i} \sqrt{\left(\tilde{\boldsymbol{\varphi}}_i^* \right)^T \tilde{\boldsymbol{\varphi}}_i}}, \quad \text{for} \quad i = 1 \ldots N. \tag{2.24}$$

The larger OMAC_i value reflects the higher correlation. It means the identification of

i-th mode will be more reliable. Therefore the criterion is set as

$$\mathrm{OMAC}_i \geq C_{omac}. \tag{2.25}$$

Based on Eq.(2.25), we can just preserve the modes satisfied this condition and employ

these remaining modes for system identification through Eq.(2.15).

Given Rotation of Recursive SI

To identify system on-line and keep a fast calculation speed, a recursive algorithm is needed. The recursive-SI algorithm can be separated into following three parts:

1. Calculate the SI for the initial round and keep the LQ factorization result.

2. For the following cases, the Hankel matrix in Eq.(2.18) should be updated with new measurement and eliminate the old data with the same size.

3. The LQ factorization of the new Hankel matrix can be replaced by applying a recursive algorithm, named given rotation, two times on the previous LQ result for updating and eliminating the data.

Thus, the calculation of LQ factorization of the whole new Hankel matrix is omitted. It will not only save lots of computation time but also preserve the accuracy. Detail introduction of the processes of RSI algorithm can refer to [26, 27].

2.2.3 Principal Component Analysis (PCA)

The PCA also known as Karhunen–Loève transform is first introduced by Pearson [18] as a line fitting algorithm in data space. The concept of PCA is to find orthogonal bases called principal components (PCs) which represented the largest possible variance direction of the data. Moreover, the PCs are arranged in descending order which means

the first PC has largest data variance. For dynamic analysis, PCs can represent system normal modes based on few assumptions. Therefore, it is also called proper orthogonal decomposition (POD) and the extracted PCs are called proper orthogonal modes (POMs). The procedures of PCA algorithm for structural analysis are as follows:

Data Ensemble Matrix and Correlation Representation

The PCA starts from the construction of the ensemble data matrix $\mathbf{X}$ of all measured response signals, that is

$$\mathbf{X} = \begin{bmatrix} x_1(t_1) & x_1(t_2) & \cdots & x_1(t_N) \\ x_2(t_1) & x_2(t_2) & \cdots & x_2(t_N) \\ \vdots & \vdots & \ddots & \vdots \\ x_m(t_1) & x_m(t_2) & \cdots & x_m(t_N) \end{bmatrix}, \tag{2.26}$$

each x_i represents a time series measurement of acceleration, velocity, or displacement on a particular position of the structure. The suffix m means total number of measurement. After the ensemble matrix $\mathbf{X}$ is arranged, the covariance matrix $\mathbf{C} \in \mathbb{R}^{m \times n}$ can be derived as

$$\mathbf{C} = \frac{1}{N} \mathbf{X} \mathbf{X}^T. \tag{2.27}$$

Orthogonal basis of Principal Components

Based on the derivation [13], the orthogonal basis of PCs can be derived from the eigen-decomposition of matrix $\mathbf{C}$ that is

$$\mathbf{C} = \mathbf{\Psi} \mathbf{\Lambda} \mathbf{\Psi}^{-1}, \tag{2.28}$$

17

where the eigenvectors $\boldsymbol{\Psi}$ are the PCs of matrix $\mathbf{X}$.

Normal Modes and Principal Components

Assume ensemble matrix $\mathbf{X}$ of structural response satisfies modal combination theorem. Therefore, $\mathbf{X}$ could be written as the combination of normal modes that

$$\mathbf{X} = \boldsymbol{\Phi}\mathbf{Q}^T = \sum_{i=1}^{m} \boldsymbol{\varphi}_i \mathbf{q}_i^T, \qquad (2.29)$$

where the $\boldsymbol{\varphi}_i$, $\mathbf{q}_i$, and m are normal modes, general coordinates, and number of modes can be extracted. Assume the structural mass matrix is homogeneous that $\mathbf{M} = m\mathbf{I}$ and satisfies $\boldsymbol{\varphi}_i^T \mathbf{M} \boldsymbol{\varphi}_j = \delta_{ij}$. Combine Eq.(2.27) and Eq.(2.29) together with right multiple $\boldsymbol{\varphi}_i$, it will become

$$\mathbf{C}\boldsymbol{\varphi}_k = \frac{1}{N} \sum_{i=1}^{m} \sum_{j=1}^{m} \boldsymbol{\varphi}_i \mathbf{q}_i^T \mathbf{q}_j \boldsymbol{\varphi}_j^T \boldsymbol{\varphi}_k = \frac{1}{N} \sum_{i=1}^{m} \boldsymbol{\varphi}_i \mathbf{q}_i^T \mathbf{q}_k \frac{\delta_{kk}}{m}. \qquad (2.30)$$

Furthermore, assume the damping ratio is relatively small. Eq.(2.30) can be rewritten as

$$\begin{cases} \lim_{N \to \infty} \dfrac{\mathbf{q}_i \mathbf{q}_k^T}{N} = 0, & \text{for } i = k \\ \lim_{N \to \infty} \dfrac{\mathbf{q}_i \mathbf{q}_k^T}{N} \neq 0, & \text{for } i = k \end{cases} \rightarrow \mathbf{C}\boldsymbol{\varphi}_k = \frac{1}{N} \boldsymbol{\varphi}_k \mathbf{q}_k^T \mathbf{q}_k \frac{\delta_{kk}}{m}. \qquad (2.31)$$

In this equation, $\dfrac{1}{N} \mathbf{q}_k^T \mathbf{q}_k \dfrac{\delta_{kk}}{m}$ is constant and can be assumed as λ_k. Therefore, we get

$$\mathbf{C}\boldsymbol{\varphi}_k = \lambda_k \boldsymbol{\varphi}_k. \qquad (2.32)$$

Eq.(2.32) is equivalent to Eq.(2.28) as eigen-decomposition of matrix $\mathbf{C}$. Thus, we have proven that PCs $\boldsymbol{\Psi}$ are the same as structural normal modes $\boldsymbol{\Phi}$.

Through the derivation [3], three conditions need to be guaranteed for the equivalent of normal modes. There are 1.the structural damping ratio is small in all cases, 2.number of observation is large enough, and 3.the mass distribution is homogenous. If the mass are not uniform distribution, a modified correlation matrix is suggested [10] to improve the analysis result, that is

$$\mathbf{C}_m = \frac{1}{N}\mathbf{X}\mathbf{X}^T\mathbf{M}. \tag{2.33}$$

The mass matrix $\mathbf{M}$ should be determined first to do the modification. According to numerical survey [2], PCA though may lose some precision; it can obtain the structural normal modes very briefly.

2.3 Local Element Motion Analysis

Since the spatial displacement data can represent an object motion very detail, there must have some local information according to the mesh elements of these sensors. To get the information from elements' three dimensional motion, the singular spectral analysis (SSA) as powerful multivariate signal decomposition technique is introduced. Moreover, the signal discontinuity is detected by continuous wavelet transform (CWT) to find the crack effect. Finally, finite element method (FEM) which is well defined in mesh filed will also be discussed.

2.3.1 Singular Spectral Analysis (SSA)

The SSA as a linear time series feature extraction technique is similar to apply the PCA on the time series with the embedding theorem [24] which combines lagged copies of the original data from lag 1 to k time steps. By performing the SSA, time series will be decomposed into several feature components that can be treat as trend, oscillation, or noise components [6, 9]. The procedures of SSA can be separated into four steps, which are (1) embedding, (2) SVD, (3) grouping, and (4) reconstruction. Details introduction are described as follows:

Embedding Theorem

Consider a time series $\mathbf{y}(t) = \begin{bmatrix} y_0 & y_1 & \cdots & y_{N-1} \end{bmatrix}$ of length N. The embedding theorem maps the time series into a sequence of multi-dimensional lagged vectors. In this step, the only SSA parameter L called window length should be determined, where the range is $2 \leq L \leq N/2$. Then $K = N - L + 1$ lagged vectors are embedded to form the trajectory matrix $\mathbf{X}$,

$$\mathbf{X} = \left(x_{i,j} \right)_{i,j=1}^{L,K} = \begin{bmatrix} y_0 & y_1 & y_2 & \cdots & y_{K-1} \\ y_1 & y_2 & y_3 & \cdots & y_K \\ y_2 & y_3 & y_4 & \cdots & y_{K+1} \\ \vdots & \vdots & \vdots & \ddots & \vdots \\ y_{L-1} & y_L & y_{L+1} & \cdots & y_{N-1} \end{bmatrix}_{L \times K} = \begin{bmatrix} \mathbf{x}_1 & \mathbf{x}_2 & \cdots & \mathbf{x}_K \end{bmatrix}, \qquad (2.34)$$

where $\mathbf{x}_i = \begin{bmatrix} y_{i-1} & y_i & \cdots & y_{i+L-2} \end{bmatrix}^T$ for $1 \le i \le K$ is the i-th lagged vector. One of the

properties of trajectory matrix is that it is Hankel matrix which the skew diagonal terms

($i + j =$ const.) are equal. If the analysis data are multivariate, each component of $y(t)$

should be treated as a vector form that $y_i \Rightarrow \{\mathbf{y}_i\} = \begin{bmatrix} y_{1,i} & y_{2,i} & \cdots & y_{n,i} \end{bmatrix}^T$ where n is

the total number of variate.

Singular Value Decomposition (SVD)

The second step is to perform SVD to the trajectory matrix $\mathbf{X}$. First define a

matrix $\mathbf{S} = \mathbf{X}\mathbf{X}^T$. The eigenvalues of matrix $\mathbf{S}$ are denoted by $\lambda_1, \ldots, \lambda_n$ in the

descending order ($\lambda_1 \ge \ldots \ge \lambda_n \ge 0$) and the corresponding eigenvectors are $\mathbf{u}_1, \ldots, \mathbf{u}_L$.

Then, define vector $\mathbf{v}_i = \mathbf{X}^T \mathbf{u}_i / \sqrt{\lambda_i}$. The SVD of the trajectory matrix $\mathbf{X}$ can be

written as

$$\mathbf{X} = \sum_{i=1}^{d} \sqrt{\lambda_i} \mathbf{u}_i \mathbf{v}_i^T = \mathbf{X}_1 + \mathbf{X}_2 + \ldots + \mathbf{X}_d. \tag{2.35}$$

Each $\mathbf{X}_i = \sqrt{\lambda_i} \mathbf{u}_i \mathbf{v}_i^T$ is a rank 1 elementary matrix and d is $\max(i)$ with $\lambda_i > 0$.

The set of $\sqrt{\lambda_i}$ is called singular values (SVs). It contains the important information of

decomposition quality and should be plotting out as singular spectrum.

Grouping

After the SVD is applied, the trajectory matrix $\mathbf{X}$ has been decomposed into

several components. The grouping step is to select the appropriate elementary matrices

to form an approximate trajectory matrix $\tilde{\mathbf{X}}$. Decision-making of which components

should be selected can refer to the singular spectrum. The singular spectrum shows brief

decomposed properties [6] that oscillation comes with two closed SVs in a pair; trend

component has a lonely SV in a certain amount; series of low value SVs may represent

signal noise. Therefore through singular spectrum, one can group correlative

eigentriples ($\sqrt{\lambda_i}\,\mathbf{u}_i\mathbf{v}_i^T$) following the type of components would like to reconstruct.

Reconstruction (Diagonal Averaging)

Since approximate trajectory matrix $\tilde{\mathbf{X}}$ is no longer kept the property that skew

diagonal terms are equal, new time series $\tilde{\mathbf{y}}(t)$ should be reconstructed by diagonal

averaging the matrix $\tilde{\mathbf{X}}$ based on this property. The scheme of diagonal averaging is

shown as

$$\tilde{\mathbf{X}} = \begin{bmatrix} x_{1,1} & x_{1,2} & x_{1,3} & \cdots & x_{1,K} \\ x_{2,1} & x_{2,2} & x_{2,3} & \cdots & x_{2,K} \\ x_{3,1} & x_{3,2} & x_{3,3} & \cdots & x_{3,K} \\ \vdots & \vdots & \vdots & \ddots & \vdots \\ x_{L,1} & x_{L,2} & x_{L,3} & \cdots & x_{L,K} \end{bmatrix} \xrightarrow{\text{Dgnl. Avg.}} \tilde{\mathbf{y}}(t) = \begin{bmatrix} x_{1,1} & \dfrac{1}{2}(x_{1,2} + x_{2,1}) & \cdots \end{bmatrix}, \quad (2.36)$$

where $\tilde{\mathbf{y}}(t)$ is the reconstructed time signal of length N. If the approximate trajectory

matrix $\tilde{\mathbf{X}}$ is selected to be an elementary matrix of the SVD result, the reconstructed

signal $\tilde{\mathbf{y}}_i(t)$ will also be called principal component. Equation form [9] of diagonal

averaging can be written as

$$\tilde{y}_i = \begin{cases} \dfrac{1}{i+1}\displaystyle\sum_{m=1}^{i+1} x_{m,i-m+2}, & \text{for } 0 \le i \le L' \\[3mm] \dfrac{1}{L'}\displaystyle\sum_{m=1}^{L'} x_{m,i-m+2}, & \text{for } L'-1 \le i < K', \\[3mm] \dfrac{1}{N-i}\displaystyle\sum_{m=i-K'+2}^{N-K'+1} x_{m,i-m+2}, & \text{for } K' \le i < N \end{cases} \qquad (2.37)$$

where $L' = \min(L,K)$ and $K' = \max(L,K)$. By selecting the different grouping components, the original time series can be decomposed into additive components represented the data feature.

2.3.2 Continuous Wavelet Transform (CWT)

The wavelet transform is a signal processing technique that decomposes the signal into the combination of wavelets. Different from the well-known STFT, the wavelet transform is believed that it offers more suitable time frequency decomposition. The CWT is a division of wavelet transform that divides a continuous time series into wavelets. In the wavelet analysis, the CWT starts from selecting a wavelet function called mother wavelet. The mother wavelet should satisfy some criteria that it's narrow band, zero-mean, and with boundary value zero. In this research, the mother wavelet is selected the 'bior6.8' of MATLAB build-in wavelet function. The algorithm of CWT only contains two steps. They are briefly described as follows:

Wavelet Kernel and CWT

The CWT starts with the selection of mother wavelet and the definition of wavelet kernel. Assume the mother wavelet is $\psi(t)$. The wavelet kernel is defined as

$$\psi_{a,b}(t) = \frac{1}{\sqrt{|a|}} \psi\left(\frac{t-b}{a}\right). \tag{2.38}$$

The parameter $a > 0$ is called scale value, and b is called translation value. Since the mother wavelet is a narrow-band function and only has a central frequency f. The value a will scale the mother wavelet's central frequency, and value b defines the mother wavelet's location. Eq.(2.38) transforms the time function of mother wavelet into a two dimensional time-scale wavelet kernel function which can obtain the CWT.

Define a square integrable time signal $x(t)$. The second step of CWT is to transform $x(t)$ into time-scale plane with the help of wavelet kernel, that is

$$X(a,b) = \int_{-\infty}^{\infty} x(t) \psi_{a,b}^*(t) dt, \tag{2.39}$$

where the $(\cdot)^*$ represents the operator of complex conjugate. By using the Eq.(2.39), the time function $x(t)$ has becomes a time-scale function $X(a,b)$. The value of $X(a,b)$ is called wavelet coefficient. It is likes a shifting processing that using the mother wavelet to fit the input signal with corresponding a and b. This two variates function can plot a figure called scalogram. The higher value in scalogram means the energy concentration region of the signal $x(t)$. For a signal with non-continuity, the

24

scalogram of CWT will present a high value in the non-continuous time instance with a very long scale range. So, we can detect the signal non-continuity using the output time-scale scalogram via this property.

2.3.3 Finite Element Method (FEM)

The finite element analysis is a numerical approach that the partial differential equations (PDEs) can be solved approximately via discrete equations [19]. It is first invented for civil engineering problem, and now successfully employed in vast area. The concept of FEM is to transform the boundary value problems (BVPs) called strong form into equivalent integral equations called weak form, and then discretize the weak form into the finite domain space [8]. Following this way, the numerical integration to solve the discretized problem becomes possible. In this research, the measured spatial locations can be treated as the nodes of discretized element. Since the displacement is measured directly, the strain field can be derived following a more general representation without solving BVPs. For this analysis, we define the discretized element is a four nodes quadrilateral (Q4) element. The derivation of strain field via the FEM is as follows:

Natural Coordinate and Element Shape Function

To develop the properties of the Q4 element, first we consider the coordinate representation. Though the element shape can be well defined in the physical coordinate, it is hard to perform calculation while the orientation is arbitrary. Therefore, the natural coordinate is obtained. The natural coordinate lies in (ξ, η) plane that the boundary is $-1 \leq \xi, \eta \leq +1$. With the mapping technique, we can depict the Q4 element into the natural coordinate for more clear representation (Figure 2-3). Based on the natural coordinate system, the element shape function N_i^{4Q} (Figure 2-4) in (ξ, η) plane is obtained as

$$N_i^{4Q}(\xi, \eta) = \frac{1}{4}(1 + \xi_i \xi)(1 + \eta_i \eta). \tag{2.40}$$

Moreover, the displacement field $\mathbf{u}(\xi, \eta) = \begin{bmatrix} u_x & u_y \end{bmatrix}_{(\xi, \eta)}^T$ can also be represented as

$$\mathbf{u}(\xi, \eta) = \mathbf{N}^{4Q}(\xi, \eta)\mathbf{d}^e, \tag{2.41}$$

where the shape matrix $\mathbf{N}^{4Q}(\xi, \eta)$ and displacement vector $\mathbf{d}^e$ are

$$\mathbf{d}^e = \begin{bmatrix} u_1 & v_1 & u_2 & v_2 & u_3 & v_3 & u_4 & v_4 \end{bmatrix}^T, \tag{2.42}$$

$$\mathbf{N}^{4Q}(\xi, \eta) = \begin{bmatrix} N_1^{4Q} & 0 & N_2^{4Q} & 0 & N_3^{4Q} & 0 & N_4^{4Q} & 0 \\ 0 & N_1^{4Q} & 0 & N_2^{4Q} & 0 & N_3^{4Q} & 0 & N_4^{4Q} \end{bmatrix}_{(\xi, \eta)}. \tag{2.43}$$

Kinematic Equation and Strain Field

The kinematic equation between displacement field and strain field is defined as

$$\boldsymbol{\varepsilon} = \nabla_s \mathbf{u} \Leftrightarrow \begin{bmatrix} \varepsilon_{xx} \\ \varepsilon_{yy} \\ \gamma_{xy} \end{bmatrix} = \begin{bmatrix} \dfrac{\partial}{\partial x} & 0 \\ 0 & \dfrac{\partial}{\partial y} \\ \dfrac{\partial}{\partial y} & \dfrac{\partial}{\partial x} \end{bmatrix} \begin{bmatrix} u_x \\ u_y \end{bmatrix}. \tag{2.44}$$

Combines the Eq.(2.41) and Eq.(2.44) together, we have

$$\boldsymbol{\varepsilon} = \nabla_s \mathbf{u} = \nabla_s \mathbf{N}^{4Q} \mathbf{d}^e = \mathbf{B}^e \mathbf{d}^e, \tag{2.45}$$

$$\mathbf{B}^e = \begin{bmatrix} \dfrac{\partial N_1^{4Q}}{\partial x} & 0 & \dfrac{\partial N_2^{4Q}}{\partial x} & 0 & \dfrac{\partial N_3^{4Q}}{\partial x} & 0 & \dfrac{\partial N_4^{4Q}}{\partial x} & 0 \\ 0 & \dfrac{\partial N_1^{4Q}}{\partial y} & 0 & \dfrac{\partial N_2^{4Q}}{\partial y} & 0 & \dfrac{\partial N_3^{4Q}}{\partial y} & 0 & \dfrac{\partial N_4^{4Q}}{\partial y} \\ \dfrac{\partial N_1^{4Q}}{\partial y} & \dfrac{\partial N_1^{4Q}}{\partial x} & \dfrac{\partial N_2^{4Q}}{\partial y} & \dfrac{\partial N_2^{4Q}}{\partial x} & \dfrac{\partial N_3^{4Q}}{\partial y} & \dfrac{\partial N_3^{4Q}}{\partial x} & \dfrac{\partial N_4^{4Q}}{\partial y} & \dfrac{\partial N_4^{4Q}}{\partial x} \end{bmatrix}_{(\xi,\eta)}. \tag{2.46}$$

The matrix $\mathbf{B}^e$ is called the strain-displacement matrix. According to this matrix, we found out it is necessary to compute the differentials in terms of physical coordinate. Since the shape function N_i^{4Q} is obtained in (ξ, η) plane, the chain rule is utilized to perform the differentials, that is

$$\begin{bmatrix} \dfrac{\partial N_i^{4Q}}{\partial \xi} \\ \dfrac{\partial N_i^{4Q}}{\partial \eta} \end{bmatrix} = \begin{bmatrix} \dfrac{\partial x}{\partial \xi} & \dfrac{\partial y}{\partial \xi} \\ \dfrac{\partial x}{\partial \eta} & \dfrac{\partial y}{\partial \eta} \end{bmatrix} \begin{bmatrix} \dfrac{\partial N_i^{4Q}}{\partial x} \\ \dfrac{\partial N_i^{4Q}}{\partial y} \end{bmatrix} = \mathbf{J}^e \begin{bmatrix} \dfrac{\partial N_i^{4Q}}{\partial x} \\ \dfrac{\partial N_i^{4Q}}{\partial y} \end{bmatrix}, \tag{2.47}$$

$$\begin{bmatrix} \dfrac{\partial N_1^{4Q}}{\partial x} & \dfrac{\partial N_2^{4Q}}{\partial x} & \dfrac{\partial N_3^{4Q}}{\partial x} & \dfrac{\partial N_4^{4Q}}{\partial x} \\ \dfrac{\partial N_1^{4Q}}{\partial y} & \dfrac{\partial N_2^{4Q}}{\partial y} & \dfrac{\partial N_3^{4Q}}{\partial y} & \dfrac{\partial N_4^{4Q}}{\partial y} \end{bmatrix} = \left(\mathbf{J}^e\right)^{-1} \begin{bmatrix} \dfrac{\partial N_1^{4Q}}{\partial \xi} & \dfrac{\partial N_2^{4Q}}{\partial \xi} & \dfrac{\partial N_3^{4Q}}{\partial \xi} & \dfrac{\partial N_4^{4Q}}{\partial \xi} \\ \dfrac{\partial N_1^{4Q}}{\partial \eta} & \dfrac{\partial N_2^{4Q}}{\partial \eta} & \dfrac{\partial N_3^{4Q}}{\partial \eta} & \dfrac{\partial N_4^{4Q}}{\partial \eta} \end{bmatrix}. \tag{2.48}$$

The matrix $\mathbf{J}^e$ is called the Jacobian matrix and can also be derived follows

$$\mathbf{J}^e = \begin{bmatrix} \displaystyle\sum_{i=1}^{4} \frac{x_i^e \partial N_i^{4Q}}{\partial \xi} & \displaystyle\sum_{i=1}^{4} \frac{y_i^e \partial N_i^{4Q}}{\partial \xi} \\ \displaystyle\sum_{i=1}^{4} \frac{x_i^e \partial N_i^{4Q}}{\partial \eta} & \displaystyle\sum_{i=1}^{4} \frac{y_i^e \partial N_i^{4Q}}{\partial \eta} \end{bmatrix} = \begin{bmatrix} \dfrac{\partial N_1^{4Q}}{\partial \xi} & \dfrac{\partial N_2^{4Q}}{\partial \xi} & \dfrac{\partial N_3^{4Q}}{\partial \xi} & \dfrac{\partial N_4^{4Q}}{\partial \xi} \\ \dfrac{\partial N_1^{4Q}}{\partial \eta} & \dfrac{\partial N_2^{4Q}}{\partial \eta} & \dfrac{\partial N_3^{4Q}}{\partial \eta} & \dfrac{\partial N_4^{4Q}}{\partial \eta} \end{bmatrix} \begin{bmatrix} x_1^e & y_1^e \\ x_2^e & y_2^e \\ x_3^e & y_3^e \\ x_4^e & y_4^e \end{bmatrix}, \quad (2.49)$$

where the x_i^e and y_i^e are the initial nodal positions. Therefore, the differentials of

shape functions in terms of physical coordinate can be transformed into the differentials

in terms of (ξ, η) plane following Eq.(2.47) and Eq.(2.49). After solving the

differentials, they can be arranged to get the strain-displacement matrix $\mathbf{B}^e$. It should

be mention that the matrix $\mathbf{B}^e$ is a function of (ξ, η) since $\partial N_i^{4Q}/\xi$ and $\partial N_i^{4Q}/\eta$

are not constant. It means the strain field $\boldsymbol{\varepsilon}$ in Q4 element is not a constant, either. For

a normal FE representation, we usually calculate the strain field on the location of the

2×2 Gauss points where are

$$(\xi_1, \xi_2) = \left(+\frac{1}{\sqrt{3}}, -\frac{1}{\sqrt{3}} \right), \text{ and } (\eta_1, \eta_2) = \left(+\frac{1}{\sqrt{3}}, -\frac{1}{\sqrt{3}} \right). \quad (2.50)$$

Hence, we can derive strain fields on the four points within the Q4 element. That is

$$\begin{aligned} \boldsymbol{\varepsilon}_1 &= \mathbf{B}^e(\xi_1, \eta_1)\mathbf{d}^e, \quad \boldsymbol{\varepsilon}_2 = \mathbf{B}^e(\xi_1, \eta_2)\mathbf{d}^e, \\ \boldsymbol{\varepsilon}_3 &= \mathbf{B}^e(\xi_2, \eta_1)\mathbf{d}^e, \quad \boldsymbol{\varepsilon}_4 = \mathbf{B}^e(\xi_2, \eta_2)\mathbf{d}^e. \end{aligned} \quad (2.51)$$

The average strain field of Q4 element can be obtained as

$$\boldsymbol{\varepsilon}_{avg} = \sum_{i=1}^{4} \boldsymbol{\varepsilon}_i. \quad (2.52)$$

28

The above procedures can be performed onto different meshes just use the information of the initial nodal positions (Eq.(2.49)) and the displacement vector (Eq.(2.42)), therefore the strain field of the entire domain can be derived.

2.4 Chapter Summary

This chapter has introduced all the algorithms presented in this research. They have been categories into two groups. The first group is global characteristics identification including three methods. The first-two are subspace identification methods including the SSI-COV (Section 2.2.1) and the RSI (Section 2.2.2). Both methods can identify the system natural frequency and damping ratio. The difference between them is as follows: the SSI-COV uses output measurement only to perform the identification where the measured data should satisfy the ambient vibration assumption. On the other hand, the recursive-SI needs both input and output measurement to do the identification. Moreover, it can identify system state on-line during the excitation according to moving window technique. The other method to identify system state is the PCA (Section 2.2.3). Base on the derivation, we can conclude that system normal modes can be approached as signals' PCs follow three restrictions: 1.the damping ratio is small enough in all cases, 2.the structural mass matrix is homogeneous, and 3.the number of measurement should

be larger enough. Following these criteria, the system normal modes can be obtained by the PCA.

After the global system characteristics are identified, we go detail of the local motion properties based on three different analyses. The first one is the SSA (Section 2.3.1). It can decompose local signals into the mutual mono-components following their energy contribution. Moreover, the singular spectrum of the SSA can reflect the decomposition quality and give the preview of the signal information. According to these properties, the SSA is employed to extract the local element's principal motion for further analysis. The other method is CWT (Section 2.3.2). With the help of wavelet kernel, the CWT can transform input signal into a time-scale plane called scalogram that represents the time frequency decomposition. The resulting wavelet coefficient gives the energy distribution of the signal. While the signal is not continuous at certain time instances, the scalogram will come out a high energy concentration at that time instances with a wide range of scale distribution. This property is used to judge the crack movement. The last method is finite element analysis (Section 2.3.3). Because the spatial measurement has obtained the information of full dimensional element motion, the FEM can be easily performed to derive the element's strain field using the displacement measurement. After the elements' motion properties are derived. We can

compare the analysis result between elements to defined damage location. The research

framework is shown in Figure 2-6. Further analysis of real structural system will

mention in next chapter.

Chapter 3. Experimental Survey

3.1 Description of the Experiment

In order to study the application of spatial displacement signals in a real structure system, the data of a series of shake table test in the National Center for Research on Earthquake Engineering (NCREE) in Taiwan is chose for further analysis. The experimental specimen was an one-story two-bay reinforce concrete (RC) frame constructed following the Taiwanese design code, with the story height 2 m, span length 2 m, and the approximate weight 6500 kg. The cross section of three columns was 20 cm×20 cm, and both joints of the side columns were reinforced for repeated loading. The design detail and configurations of RC frame can refer to Figure 3-1 and Figure 3-2. This experiment constructed six specimens following the same design detail. For shake table test, each specimen was subjected to seismic loading along its longitudinal direction. To measure the structure vibration, two measuring systems were employed. First system is most commonly used in NCREE including 12 accelerometers, 4 lateral LVDTs, and 16 small LVDTs. These devices measured the frame acceleration, lateral displacement, and detail deformation of local connection. This system was connected to the control center and measured with sampling frequency 200 Hz. The other measuring

system was optical sensing system, with total 24 optical targets which were marked on the central column to measure the spatial displacement information. This system was independent from control center with its own sampling frequency 100 Hz. To synchronize both measuring systems, optical sensing system was triggered with control center. The configurations of each sensing devices can access from Figure 3-3 to Figure 3-5. The input ground motion of shake table test was selected the Chi-Chi earthquake in Taiwan (Station TCU082) which is shown in Figure 3-6. Two groups of tests were performed. The Group1 compared the response of 4 specimens with different intensity level. And Group2 focused on a single specimen (RCF6) excited by series of excitation with different intensity level applied back to back. The intensity level was selected 600 gal, 800 gal, 1000 gal, 1200 gal, 1000 gal, 800 gal, 600 gal (Numbered from RCF6-1 to RCF6-7). The physical information of these excitations is listed in Table 3-1.

In this research, the analysis will focus on the Group2 test and the spatial displacement data acquired from the optical sensing system. The signal analysis methodologies mentioned in previous chapter are applied to identify the system parameters and produce damage assessment.

3.2 Preview of System Physical Properties

Since this experiment was recorded using two different measuring system and the data from normal measuring system including accelerometers and lateral LVDTs had been well studied by other researchers [12, 14, 16], there are some structural physical properties we can preview (acceleration measurement of RCF6-2 (800 gal) was broken). First is the absolute acceleration response (Figure 3-7). The Fourier spectrum (Figure 3-8) of it shows that the structure dominant frequency response changed during these seismic vibrations. The system natural frequency is also identified by absolute acceleration data using equilibrium linear system analysis (Table 3-1). Another measurement is about the relative displacement from the lateral LVDTs (Figure 3-9). It displays that the structure had permanent deformation in each seismic response. If we transform this displacement data into story drift ratio (Figure 3-10), the most vibration time frame can be roughly estimate. Finally is the hysteresis behavior (Figure 3-11) of each seismic test. From this figure, the stiffness degradation is significant during first two cases. After that, the structural stiffness just changed slightly.

3.3 Optical Data Preprocessing

As mentioned in the Section 3.1, the spatial displacement data is measured using an optical sensing system. This system is called Dynamic Measuring Machine (DMM) designed by NDI Inc. It consists of two major devices. One is the Target-based Photogrammetry that provides the ability to conduct dynamic measurement functions and full three dimensional tracking. The other device is OPTOTRAK[®] Certus which is the optical tracker. It will track the optical laser flashed by the target system that marks on the specific points of the structure. The tracker has the ability to track how these three dimensional measurements change over time for dynamic motion measurement with RMS accuracy up to 0.1 mm. Detail configuration of optical sensing system is shown in Figure 3-12. Since the optical tracker uses its own processing system to measure the three dimensional motion over time, some optical data preprocessing techniques must be performed before utilizing these measured signals. The processing techniques are listed as follows:

3.3.1 Three Dimensional Affine Transformation

The original three dimensional measurements are stored in a regular Cartesian coordinate defined by the optical tracker's location and facing direction. Although the

coordinate can be set up as correct as possible, it still has some difference because of the

personal equation. The scheme of this question is shown in Figure 3-13, where axes

x_1-y_1-z_1 may refer to the coordinate of optical sensing system and axes x_2-y_2-z_2 are

the design system. To correct the difference, the three dimensional affine transformation

that combines of rotation and translation of the coordinate is performed. The processes

are as below:

First is arranging the design position of all optical targets and the measured

position at the initial stage in two ensemble matrices with an adding coordinate w of

value 1, that is

$$\mathbf{P}_{design} = \begin{bmatrix} x \\ y \\ z \\ w \end{bmatrix} = \begin{bmatrix} x_1 & x_2 & \cdots & x_n \\ y_1 & y_2 & \cdots & y_n \\ z_1 & z_2 & \cdots & z_n \\ 1 & 1 & \cdots & 1 \end{bmatrix}, \text{ and } \mathbf{P}_{measure,init} = \begin{bmatrix} x' \\ y' \\ z' \\ w' \end{bmatrix} = \begin{bmatrix} x_1' & x_2' & \cdots & x_n' \\ y_1' & y_2' & \cdots & y_n' \\ z_1' & z_2' & \cdots & z_n' \\ 1 & 1 & \cdots & 1 \end{bmatrix}. \quad (3.1)$$

The suffix $1,\ldots,n$ represents order of optical sensors in the experiment. This kind of

coordinate representation is called the homogenous coordinates. The adding coordinate

of value 1 conducts the application of translation. Therefore, the transform matrix $\mathbf{T}$

between these two ensemble matrices can perform both rotation and translation of the

vector space. To get the transform matrix $\mathbf{T}$ at the second step, the division of two

ensemble matrices is calculated. That is

$$\mathbf{T} = \mathbf{P}_{design}\mathbf{P}_{measure,init}^+. \quad (3.2)$$

37

As soon as the coordinate transform matrix $\mathbf{T}$ between design and optical system is known, the optical measurement over time can be transform into the design coordinate system by left multiplying $\mathbf{T}$, that is

$$\mathbf{P}_{correct}(t) = \mathbf{T}\mathbf{P}_{measure}(t). \tag{3.3}$$

Therefore, the data in $\mathbf{P}_{correct}(t)$ will show in the design coordinate system we define.

3.3.2 Shifting of Target Positions

The target positions originally are determined at the design stage and then marked onto the test specimen, and therefore $\mathbf{P}_{correct,init}$ of the affine transformation result should be the same as design position $\mathbf{P}_{design}$ at the initial stage. But actually there are slightly differences between them according to the mark imperfection, shifting of target position are employed to eliminate the differences. Thus, the resulting measurements can compare to the design.

Shifting process is done by finding the translation matrix $\mathbf{M} = \mathbf{P}_{design} - \mathbf{P}_{correct,init}$ at the initial stage. After the translation matrix $\mathbf{M}$ is determined, the measurement over time can be revised by following the equation,

$$\mathbf{P}_{revise}(t) = \mathbf{P}_{correct}(t) + \mathbf{M}. \tag{3.4}$$

These two methods including the affine transformation and shifting of target

position are the main optical data preprocessing techniques used in this experiment.

Thus, the following analysis will utilize $\mathbf{P}_{revise}(t)$ as the data of optical measurement.

3.4 Global System Characteristics Identification

In this section, the measured three dimensional displacements are used to identify

global system characteristics. The identified system characteristics focus on the natural

frequency, damping ratio, and mode shapes. Methodologies introduced in the Section

2.2 will be employed here to do the analysis.

3.4.1 Global System Identification by SSI-COV

As mention in the Section 2.2.1, the derivation of SSI-COV is based on the

discrete-time state space model transform from motion equation. Therefore the input

data of optical measurement should use the relative displacement. The stochastic

property of input data is another limitation should be confirmed as well. Only the

measurement of white noise vibration satisfies this condition and is employed to

identify the system.

Before using the SSI-COV, two parameters should be defined. One is the C_{svd}

that determines the percentage of SVD result could be preserved. The other is number

of row i which defined for building the data Hankel matrix. These two parameters

sometimes influence the identification of system. For example, the larger C_{svd} value

will involve more signal information so that more identified results whether they are

noise or not may present; the number of row i changes the arrangement of data

Hankel matrix and the identified results may perturbations according to this reason. To

deal with these problems, the stability diagram [15] is introduced. It is achieved by

plotting calculation result (mostly the frequency) versus the number of row i in the

same figure. The real system modes in this diagram should be present in a line

accordingly. As contrast, noise modes will appear in a mess. Therefore, it can be easy to

identify the real system characteristics from this diagram.

For this research, all the white noise vibration cases are used and the employed

sensors are focus on central column (Sensor order 2-12, 18-26). The C_{svd} value is

selected to be 0.7, 0.8, and 0.9, as well as the number of row i vary between 2 and 200.

The stability diagrams of identified result show from Figure 3-14 to Figure 3-16. These

figures were plotted with frequency domain decomposition (FDD) as compared. From

these figures, not only the SSI-COV but also the FDD show a single structure mode

during the series of shake table tests. It may due to the almost SDOF system according

to the one-story two-bay RC frame. And after each excitation, the structure natural

frequency got a little bit smaller of entire round. This situation means the structure state

changed and the stiffness became smaller and smaller. If we compare between different

C_{svd} values, the stability diagram shows that the natural frequency won't vary but the

higher C_{svd} will come out more stable identified result. The identified natural

frequency and damping ratio are listed in Table 3-2. Though the damping ratio is hard to

make a comment, the natural frequency can compare with Mao's research [16] using

equivalent linear system from accelerometers in Table 3-1. They are similar to each

other. Thus, it confirms that spatial displacement data can also be applied to identify the

system natural frequency and get a reliable result.

3.4.2 Global System Identification by RSI

The RSI is performed in this study to identify the system during seismic vibration.

To employ RSI, some procedures need to be followed. First is about the analysis dataset.

The measured structural relative displacement has permanent deformation due to the

nonlinear behavior of seismic excitation. To keep the equilibrium linear assumption of

state space model, the high-pass Butterworth filter with cut-off frequency 1 Hz is

applied to all relative displacement measurement to remove these permanent

components. The other process is to determine the window length and shift length.

These two parameters influence the identification resolution and the quality of detecting the change. For this research, the window length is 5 sec and shift length is 0.1 sec. Finally is to choose the number of row i, C_{svd}, and C_{omac} that related to de-noise techniques. According to the information from the SSI-COV, these parameters are set to be 100, 0.9, and 0.9. The same optical sensors as the SSI-COV are employed as the output measurement, and the mean measurement of optical Sensor1 and Sensor17 is used as the input measurement. The identified system natural frequency and damping ratio are shown in Figure 3-19 and Figure 3-20.

From the natural frequency variation, we found out the structural natural frequency has a significant jump at the first 600 gal excitation during 30 sec, and another jump occurs closed to 40 sec. After that, the natural frequency change during the remaining excitations just has slightly difference. The most distinguished time frame of frequency change is about 30 sec in these remaining excitations. For damping ratio variation in Figure 3-20, we found out the damping identification quality is not very well. But we can know that the system damping ratio is around 0.06, which is within the range of normal RC structural damping, and the damping is a little bit larger during the seismic effect. The identified natural frequency at the initial and end of time is listed at Table 3-3 and all the natural frequency variations are plotted in Figure 3-21.

3.4.3 Effective Mode Shape by PCA

PCA has been proved that it is capable for calculating the system mode shape in Section 2.2.3. Though there are three restrictions should be followed. For our optical sensing system, the weak point is that the marks of optical sensors are not well uniform distribution. Few sensors are placed at central and most sensors are placed at both ends (Figure 3-4). However, the optical sensors are still distributed on the whole central column with a nearly equal spacing at both ends. Therefore we can assume the restrictions are approximately agreed. One more thing needs to be mention in this analysis is that the mode shapes are approached using SVD, that is

$$\mathbf{X} = \mathbf{U}\mathbf{S}\mathbf{V}^{T}, \tag{3.5}$$

where the left singular vector $\mathbf{U}$ is equal to principal components $\mathbf{\Psi}$ which is the normal modes in Eq.(2.28). Since the normal modes are unit vectors, we plot out the mode shapes with the contribution from $\mathbf{S}$ which stand out the analysis results. The resulting first and second mode shape are shown from Figure 3-23 to Figure 3-26.

According to these figures, the contribution of first mode is relative larger than the second mode for every case. Also we know that the series of excitations is performed symmetric. The cases with the same intensity level show different contribution. This makes us detail see through the modal contribution which is

$$\text{Modal Contribution} = \frac{\mathbf{S}}{\text{trace}(\mathbf{S})} \times 100\,(\%).\qquad(3.6)$$

The calculation results of modal contribution are shown in Figure 3-27 and Table 3-3.

The contribution of first mode leads over 99% in all cases according to the almost

SDOF system. But if we further examine the scale between 99% and 100%, the modal

contribution of first mode is getting larger and larger during these cases. This tells us

while this structure suffering damage, the modal contribution will be difference, and the

contribution from first mode is getting larger.

3.4.4 Vector Space Damage Indicator by SSI-COV

From the derivation of SSI-COV in Section 2.2.1, we know that the system

extended observability matrix $\mathbf{O}_i$ is computed from the eigenvectors of SVD, and the

matrix $\mathbf{O}_i$ contains the system information, which can further calculated to $\mathbf{A}_d$, $\mathbf{C}_d$

that represented the state space equation. We expected $\mathbf{O}_i$ must have the information

while the structure varies. To detect this kind of variation, there are researchers

establishing methods to identify the vector space difference [1, 17, 27]. The concept is

that the vector space represents a certain condition of system state. The space will differ

while system changed. The left singular vectors $\mathbf{U}$ of Eq.(2.12) can conduct this kind

of detection [4]. Thus, the damage indicators of null-space and subspace are introduced:

It starts from the SVD of Eq.(2.10). While the system order is determined by $\mathbf{S}_1$ and the noise term or ultra-low level singular values are denoted by $\mathbf{S}_2$ (control by C_{svd}), the SVD can be approximated as

$$\mathbf{T} = \begin{bmatrix} \mathbf{U}_1 & \mathbf{U}_2 \end{bmatrix} \begin{bmatrix} \mathbf{S}_1 & \mathbf{0} \\ \mathbf{0} & \mathbf{S}_2 \end{bmatrix} \begin{bmatrix} \mathbf{V}_1^T \\ \mathbf{V}_2^T \end{bmatrix} \cong \begin{bmatrix} \mathbf{U}_s & \mathbf{U}_n \end{bmatrix} \begin{bmatrix} \mathbf{S}_s & \mathbf{0} \\ \mathbf{0} & \mathbf{S}_n \end{bmatrix} \begin{bmatrix} \mathbf{V}_s^T \\ \mathbf{V}_n^T \end{bmatrix}, \tag{3.7}$$

where the suffix n denotes null-space, s is subspace, and $\mathbf{S}_n \cong \mathbf{0}$. Based on the orthogonormal properties of eigenvectors, the following equations are always satisfied:

$$\mathbf{U}_s^T \mathbf{U}_n = \mathbf{0}, \tag{3.8}$$

$$\mathbf{T}^T \mathbf{T} - \mathbf{T}^T \mathbf{U} \mathbf{U}^T \mathbf{T} = \mathbf{0}. \tag{3.9}$$

Eq.(3.8) is about the orthogonality between subspace and null-space, and the second equation is the projection error on to the space expand by $\mathbf{U}$. If $\mathbf{S}_n$ is close to zero, Eq.(3.9) can be revised as

$$\mathbf{T}^T \mathbf{T} - \mathbf{T}^T \mathbf{U}_s \mathbf{U}_s^T \mathbf{T} = 0 \Leftrightarrow \sum_{i=1}^{K} \left(\mathbf{t}_i^T \mathbf{t}_i - \mathbf{t}_i^T \mathbf{U}_s \mathbf{U}_s^T \mathbf{t}_i \right) = 0, \tag{3.10}$$

where $\mathbf{t}_i$ is the i-th column vector in the Toeplitz matrix $\mathbf{T}$. Both Eq.(3.8) and Eq.(3.10) are used to detect the damage. The scheme of damage detection can refer to Figure 3-17. The vector space $\mathbf{U}$ at undamaged state (a) is set to be reference space. If the space is difference (b), the vector space $\mathbf{U}'$ is no longer equal. Compare these two vector spaces (c), they have space angle and projection value between them. To employ

this concept, assume the Toeplitz matrix $\mathbf{T}$ of reference and current state are $\mathbf{T}_0$ and

$\mathbf{T}$. Thus, the SVD of them are

$$\mathbf{T}_0 = \begin{bmatrix} \mathbf{U}_{s0} & \mathbf{U}_{n0} \end{bmatrix} \begin{bmatrix} \mathbf{S}_{s0} & \mathbf{0} \\ \mathbf{0} & \mathbf{S}_{n0} \end{bmatrix} \begin{bmatrix} \mathbf{V}_{s0}^T \\ \mathbf{V}_{n0}^T \end{bmatrix},$$
$$\mathbf{T} = \begin{bmatrix} \mathbf{U}_{s} & \mathbf{U}_{n} \end{bmatrix} \begin{bmatrix} \mathbf{S}_{s} & \mathbf{0} \\ \mathbf{0} & \mathbf{S}_{n} \end{bmatrix} \begin{bmatrix} \mathbf{V}_{s}^T \\ \mathbf{V}_{n}^T \end{bmatrix}.$$

(3.11)

The damage indicator DI_n based on the null-space of $\mathbf{T}_0$ can be defined as the

absolute mean value of the matrix evaluated from subspace and null-space that

$$\mathrm{DI}_n = \mathrm{mean}\left(\left| \mathbf{U}_s^T \mathbf{U}_{n0} \right| \right),$$

(3.12)

where $\mathrm{mean}(\cdot)$ evaluates the mean value of all elements in the bracket and $|\cdot|$ is

taking the absolute value. The other damage indicator DI_s based on the subspace of

$\mathbf{T}_0$ is also defined as

$$\mathrm{DI}_s = \frac{\sum_{i=1}^{K} \left(\mathbf{t}_i^T \mathbf{t}_i - \mathbf{t}_i^T \mathbf{U}_s \mathbf{U}_s^T \mathbf{t}_i \right)}{\sum_{i=1}^{K} \mathbf{t}_i^T \mathbf{t}_i}.$$

(3.13)

The denominator is used to normalize the DI_s. In this research, the vector space of

WN1 is set as reference state and the other cases at each time instance are treated as

current states. Base on Eq.(3.12) and Eq.(3.13), the damage indicators are shown in

Figure 3-18 and Table 3-2. As the structure suffering from seismic loading between each

white noise case, the damage indicator of DI_n and DI_s got larger and larger. The

reason why the indicator between WN1 and WN2 is more significant change than other

cases may refer to the natural frequency result of the SSI-COV. The system state had the

largest difference during the excitation of RCF6-1 (600 gal). After that, the system state

just changed slightly. The other information from Figure 3-18 is that DI_n is not

sensitive for this analysis. But it also tells the change of system state.

3.5 Local Element Motion Analysis

After global system characteristics have been identified, this section would like to

analysis the local element motion properties from the mesh of these sensor locations.

The configuration of meshes can refer to Figure 3-28. There are ten elements marked on

the central column with a rectangular shape and numbered from bottom to top. By

applying methodologies introduced in Section 2.3, these elements' principal motion,

displacement non-continuity, and strain variation during the series of excitations are

examined. These analyses are based on the geometric properties. The extracted features

will compare between elements, therefore damage location may be determined.

3.5.1 Local element principal motion by SSA

According to previous introduction, the SSA has the ability to decompose

multivariate signal into mutual trend, harmonic wave, and noise term. Following the

property, this research applies the SSA on the optical signals acquired from seismic

excitations of each mesh element (neglect central elements B5 and B6) defined in Figure 3-28. The SSA parameter L is selected as 400. By examining the singular spectrum of decomposed result, the reconstruction focuses on the dominant eigentriple defined in Eq.(2.35). Then the reconstruct signals are treated as the element principal motion. One assumption is made that the principal motion along longitudinal axis x is different from vertical axis y according to the orthogonality of axes. Therefore, they are separated into two categories and need to be analysis apart.

In this research concept, the principal motion of each concrete element should move like a rigid body motion. But while crack occurs, the element principal motion will act with a significant difference. By detecting the difference between two axes, the crack location and direction may be discoverable. This idea assumes the influence of rigid body rotation is small enough that can be neglected. The scheme of this concept can refer to Figure 3-30(a) and (b). The analysis procedures are as follows:

1. Apply SSA on displacement data of each element nodes according to the axes, and reconstruct the dominant eigentriple as element principal motion.

2. Examine the motion difference along edges based on Figure 3-30(a) and (b). The difference of edge P1-P3 and P2-P4 are for y direction, and edge P1-P2 and P3-P4 are for x direction. Definition of nodal order is in Figure 3-29.

48

3. Calculate the square-sum of the signals of difference, and observe the result. The square-sum is defined as $S_{y,i}(t) = s_{y1,i}^2(t) + s_{y2,i}^2(t)$ for i-th element y direction, where the $s_{y1}(t)$ and $s_{y2}(t)$ are the motion difference along two edges. The same process is set for x direction.

The analysis results show from Figure 3-39 to Figure 3-52 for total 7 seismic excitation cases. We select two cases for detail discussing the analysis procedure (Figure 3-31 to Figure 3-38), and the same concepts are also capable for other cases. The selected cases are RCF6-1 (600 gal) for first excitation and RCF6-4 (1200 gal) as largest excitation.

For the element principal motion along x and y axis at analysis Step1, the results of RCF6-1 are shown in Figure 3-31 and Figure 3-32 and RCF6-4 are in Figure 3-35 and Figure 3-36. These subfigures are arranged according to their position along the column. By examining the singular spectrum and the 4 nodes principal motions, we can easily found out that the principal motion of each element is reflected a trend. This tells us the principal motion is the element's permanent deformation. One will doubt that the motion of RCF6-1 x direction top side elements didn't reflect this situation. This is related to the element dominant motion properties and the SSA techniques. For this series of analyses, the elements, which reflected this condition, are listed in Table 3-4, and we will neglect these data for further analyses. Detail examine the trend

49

components, we can discover that the 4 nodes principal motions of an element are behaved in two groups. For x direction, the two groups are P1-P2 and P3-P4. And for y direction, they are P1-P4 and P2-P4. The different behavior of these group may induced by element rotation or shear deformation. But in some cases, for example RCF6-1 y direction element B2 and RCF6-4 x direction element B1 to B3, the grouping behavior is not consist. This inconsistent situation may refer to a crack presents (Figure 3-30(a) and (b)). We perform Step2 to examine the difference. The results of RCF6-1 are in Figure 3-33 and Figure 3-34; for RCF6-4 are in Figure 3-37 and Figure 3-38. The healthy elements should come out a line along zero in these figures and the damaged elements are not. Finally, compute the square-sum in Step3. Therefore, we can determine the time instant and severity between elements from Figure 3-39 to Figure 3-52.

In this three steps analysis, it eliminates the directions of difference (elongation or shortening) because of the square-sum. If considering these directions of difference and computing bending effect as Figure 3-30(c), the element motion can be estimate more detail. This research selects the element B2 y direction difference for the analysis. The analysis result is shown in Figure 3-53 with the rotation angle and left side difference plotting together. It reflects that element B2 was bending in positive z axis

and elongating along the y axis in first four cases. After that, it recovered back some

bending angle with shortening along y axis in remaining excitations.

3.5.2 Displacement non-continuity by CWT

The CWT in this research is used to detect the signals' non-continuity. For each

control element, we can calculate the displacement difference follows the geometric

detection concept in Figure 3-30(a) and (b). If the crack acted, the signals of difference

may present a non-continuous behavior. Therefore, the application of CWT can detect

this non-continuity, that the scalogram shows a high energy concentration in some time

instances. This information will tell element nonlinear motion occurrence time and may

consist with the crack occurrence.

In this research, we selected the element B2 y direction for the analysis result.

The reason is that the element B2 has the most severity damage and the cracks are lies

on x axis. The results of left and right edge differences are shown from Figure 3-54 to

Figure 3-67 with time-scale plane and the analysis signals plotting together. These

figures give the energy concentration time instance which is also the time where the

non-continuous signals acted. The identified time instances are mostly lies on 30 sec, 38

sec, 40 sec, and 47 sec. These time instances will be confirmed, that they match with the element nonlinear behavior, with other methods in Section 3.5.4.

3.5.3 Local element strain by FEM

Because the discrete elements defined in Figure 3-28 are like a finite element mesh grid and the elements orientation can be directly measured using optical sensors, the concept of two dimensional finite element analysis may applied on this kind of data. First we consider a case that the dimension of each element is already known at the initial stage (design dimension), therefore the Jacobian matrix $\mathbf{J}^e$ in Eq.(2.49) is obtained based on this information. At every time instant, the displacement vector $\mathbf{d}^e$ in Eq.(2.42) is acquired from the optical measurement. Thus, the strain field $\mathbf{\varepsilon}$ of each element can be derived. The analysis results are shown from Figure 3-68 to Figure 3-70 with all cases (RCF6-1 to RCF6-7) plotting together. The three figures represent ε_{xx}, ε_{yy}, and γ_{xy}. The dash line in each figure indicates the strain value at $\pm 3 \times 10^{-3}$, and the time interval within two ticks represents a seismic excitation. Follow the same concept as Figure 3-30, we found out that the element with most notable variation, which are B1-B3 of ε_{xx}, B1-B3, B7, B9 of ε_{yy}, and B1-B3, B7 of γ_{xy}, will match to the crack location. The different between these three groups may due to the crack

direction. In these figures, the ε_{yy} variation is much larger than ε_{xx} and γ_{xy} since most of the cracks are located along x axis.

The other case considers that the analysis is without pre-knowledge about the structure design. Therefore the element orientation can only be extracted from the optical measurement. This case is to simulate installing the optical measuring system to a structure already under service. The seismic excitation RCF6-4 with highest intensity level (1200 gal) is selected to perform this research, and the resulting strain fields are shown from Figure 3-71 to Figure 3-73. The result is different from the previous at time 270-360 sec (interval of RCF6-4), since the strain values are initialized at zero according to the case conditions. Even though the initial condition is different, the identified crack location can also be obtained from the variation of stain value. The signal of elements with crack always has an unrecoverable trend component. And if we detail examine these element strain about ε_{yy}, there are spikes occur at some particular time instant (30 sec, 38 sec, etc.). These spikes may indicate the damage action. As contract, the elements without trend have no spike presents. It also has the same condition as first case that ε_{xx} variation is not so significant than ε_{yy}, but the crack at B1 and B2 are still detectable. This approximate element strain result will be compared with other signal analysis methods in next section.

3.5.4 Connection between Local Analysis Methodologies

The previous three sections have introduced three kinds of approaches to obtain the element properties. In this section, the connections between these analysis results are discussed. First is the strain field trajectory.

The approximate strain field has been derived from the FEM, and the result with non-zero trajectory has discovered that it may consist with crack location. But the FEM strain only obtains an approximate result. This analysis would like to use the SSA principal motion to acquire the strain trajectory following more simply concept. The concept is treating the mesh element as a tiny control volume. Therefore the strain definition can be obtained (Figure 2-5) with the principal motion as

$$\varepsilon_{xx} = \left(\frac{(P_{2x} - P_{1x}) + (P_{4x} - P_{3x})}{2 \times dx} \right) \tag{3.14}$$

$$\varepsilon_{yy} = \left(\frac{(P_{3y} - P_{1y}) + (P_{4y} - P_{3y})}{2 \times dy} \right) \tag{3.15}$$

$$\gamma_{xy} = \frac{((P_{4x} - P_{3x}) - (P_{2x} - P_{1x})) dx + (-(P_{4y} - P_{2y}) + (P_{3y} - P_{1y})) dy}{2 \times dxdy} \tag{3.16}$$

This analysis selects the element B2 to perform this analysis. The resulting figures are shown from Figure 3-74 to Figure 3-76. The dash line indicates the strain trajectory obtained from FEM and solid line is result from the SSA principal motion. It can be

seen that they have the same tendency during the time interval, though tiny inconsistence is present within the strong motion duration.

The other is the crack movement time instance identification. The CWT and FEM both can detect the crack movement time instance; the CWT examines the energy concentration of scalogram, and the FEM detects the spike occurrence. This section will check the consistence of detected time instance. It is achieved by plotting the two results together and examining the identified time. The element B2 is also selected to perform this analysis, and the result is shown from Figure 3-77 to Figure 3-80. From the figures, the spike of strain ε_{yy} is match to the time instance of energy concentration of CWT. It means the detection may be reliable.

3.6 Chapter Summary

In this chapter, an experiment about a one-story two-bay RC frame is examined. This experiment consists of a series of seismic excitation with different intensity level apply back to back. Two measurement systems are installed on this specimen. One is the normal measuring system and the other is the optical measuring system. This research focuses on the data acquired from the optical measuring system. Signal analysis methodologies introduced in Chapter 2 are applied to identify the global system

characteristics and perform damage assessment. The results show well behavior to reflect system condition and local damage occurrence. It can also be compared with the identified characteristics from normal measuring system analyzed by other researchers. The summary of this analysis is as follows:

1. The seismic ground motion started at about 30 second for ensemble rounds, and these excitation levels are selected as 600 gal, 800 gal, 1000 gal, 1200 gal, 1000 gal, 800 gal, and 600 gal applied back to back..

2. The structure had already got into nonlinear behavior in first excitation, though no significant crack occurs in the central column. Due to the nonlinear behavior, permanent deformation is presented in all cases.

3. This research performs analysis based on the optical sensing system which can measure the three dimensional displacement. Before using it, coordinate correction is needed. Moreover, the mean value of Sensor1 and Sensor17 at the bottom of column is defined as the ground motion since most of the analyses are performed using relative displacement.

4. The system natural frequency and damping ratio between seismic excitations can be identified using SSI-COV. Optical sensors located in central column are used for analysis. The stability diagram just shows single mode due to an

almost SDOF system in global point of view, and the natural frequency got smaller following the cases. For a more stable identification, the number of row i should select around 100.

5. The variation of natural frequency and damping ratio during seismic can be detected by RSI. The output data of RSI is selected the same as the SSI-COV and input is the ground displacement. The parameters of RSI are window length 5 sec, shift length 0.1 sec, $C_{svd} = 0.9$, $C_{omac} = 0.9$, and $i = 100$. Analysis results reflect that the most significant frequency reduction occurs at 30 sec, and then another reduction at about 38 sec. If we compare between cases, the reduction at first case (RCF6-1) is more significant than others. The identified natural frequency can compared with SSI-COV using white noise. Though there is slightly difference between them, the trend of frequency decrease is the same.

6. The system mode shape can be briefly obtained by PCA. Relative displacement of seismic data in central column is also used in this analysis. To stand out normal mode, modal contribution computed by SVD is combined with it as effective modal shape. The modal contribution of the first mode became larger and larger along the series of excitation.

7. Damage assessment can detect by the SSI-COV vector space variation. Two damage indicators are employed in this analysis. For the analysis result, the damage indicator variation at first case (RCF6-1) is significant. After that, the indicators just enlarge a little during the remaining seismic cases.

8. Optical targets can be meshed into a group of elements. The identified element characteristics should consist with system local information.

9. The SSA applies on the element displacement data and reconstruct the dominant eigentriple will obtain the element permanent deformation. This deformation will consist while element remain rigid. If the motion get a different tendency, there might crack occurs at this element.

10. The element crack action time instance can be detected by CWT. This is achieved by examining the signal non-continuity from the time-scale scalogram. The non-continuous time instance will come out a high energy concentration with a wide scale band.

11. The local element strain variation can be derived by FEM. For the health elements, the strain value vibrates along zero. For damage elements, there are an unrecoverable component include in the strain history. There are spikes occurrences in the ε_{yy} time history which may indicate the crack motion.

12. The strain trajectory obtained from SSA principal motion has the same tendency as the finite element approach, though during the strong motion region, the approximate strain will have some inconsistence.

13. The CWT energy concentration time instance can be compared with the FEM spikes occurrence time. This condition may tell that the detection of crack movement is reliable.

Both the SSA and FEM can detect system damage location. This is not only because of the application of these methodologies but also the large amount of sensors provides by the optical measuring system

.
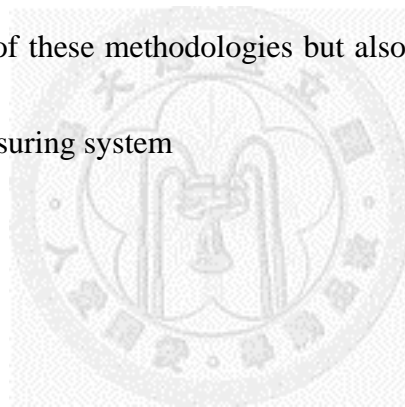
Chapter 4. Conclusions

4.1 Research Conclusions

This research studies the application of signal processing techniques on the spatial displacement data acquired by optical measuring system. The system has the ability to obtain a large amount of target points' three dimensional motion over time. Therefore it can acquire detail structural motion for structural health monitoring (SHM). An experiment of one-story two-bay RC frame is selected to perform the analysis. The central column of this frame was installed the optical measuring system for the 3D motion. The methodologies including system identification and local motion detection are applied on this spatial displacement data to see the capability for SHM. The analysis results have been discussed in Section 3.6. For this section, some conclusions of this research are made.

1. The coordinate system of measured data is important. Especially for spatial displacement signal, the motion direction should be correct; otherwise the dynamic calculation result may get wrong answer. The affine transformation is a widely used technique for coordinate transform. It can perform transformation and rotation in one time.

2. The SSI-COV is a powerful system identification technology. It performs system identification using output only signals. In most researches, the SSI-COV is applied on the acceleration data. In this research, we employed it on two dimensional displacement measurement. Based on the state space derivation, it should be also capable. The identified result just shows tiny different compare to frequency detect by equilibrium linear model. It proves the method is capable.

3. While according to the different system condition between seismic excitations, the damage should be judged. Two indicators of vector space projection theory are introduced. There are null-space damage index and subspace damage index. Both indicators are well behavior in this research that can detect the system change, and the value of subspace index is much smaller than null-space index. This highly value difference may because of the projection complexity. The null-space is more complexity than subspace.

4. For structural dynamic system identification, the RSI is used. Since the derivation is based on the state space model. The spatial displacement data should be removed the trend component before applying the analysis.

5. A brief system normal mode can be approached by sensor distributed. So, the spatial displacement data of dynamic motion analyzed by PCA is considered. The result shows that while system changed, the modal contribution will be also differs. In this case, the contribution of first mode has a tendency that's get larger and larger.

6. The mesh method of optical sensors can be judged following the element shape. For a more widely used and easily meshed element, quadratic four element is better for mesh grids

7. The SSA has the ability to extract element principal motion. While the system got into nonlinear behavior. The element principal motion is the permanent deformation. For an idea element, the element principal motion should move as rigid body. The rack may present in specific element since its 4 nodes motion have significant inconsistence that different from rigid body.

8. The signal inconsistence of the element edge may refer to the crack present. If calculating the signal difference, the non-continuity of it may consist with the crack occurrence time instance. The CWT has the ability to extract the non-continuity time instance form the signal.

9. FEM is an outstanding method for mesh-type element. Since the dynamic motion is measured from optical signals, the approximate strain field can be directly calculated without solving boundary value problem. The strain value also shows great behavior for damage localization, and can be compared with SSA approach.

10. The element strain trajectory can be approached by SSA principal motion. The calculated result is consisted with FEM trend. This means the approaches are reliable and the optical sensor arrangement is feasible for detail analysis.

This research has proved the capability of system identification using the spatial displacement data and performs damage assessment and localization. These identified results also show that they can be compared with the results obtained from normal measuring system. This means the sensing technique is a good system to measure data for SHM. But some issue also needs to be mention. First is the capability of SSA. It has been proved that the element principal motion should be a permanent deformation while structure got into nonlinear behavior. But in some cases, we are hard to extract the element permanent deformation. This is because the SSA decomposition is based on the decomposed signals energy. If the energy of permanent deformation is not significant than oscillation wave, the permanent deformation will be hard to extract. The other is

the damage quantify. The judgment of damage detects by the vector space damage indicator and other local analysis methods need to be established.

4.2 Recommendations for Future Work

The spatial displacement measurement has been proved the capability for the system identification and damage assessment. However, the optical measuring system used in this analysis is a total integrated system provides for experiment, which is not suitable for normal condition. To establish a sensing system with more widely capability for SHM, we can go detail about how to extract the three dimensional displacement data from the image. And apply this technique to the monitors installed in the structure. Another idea is to long term measuring the structural motion through monitors, and performing system identification over time. It may become a good measuring system for SHM. For the local damage assessment applied in this research. The local element crack can all be detected. But the damage condition of elements without crack is hard to be quantified. The better indices should be established to quantify the damage condition and perform early warning. These are all hard issues. Further study is needed for these problems.

References

1. Basseville, M., M. Abdelghani, and A. Benveniste, *Subspace-based fault detection algorithms for vibration monitoring.* Automatica, 2000. **36**(1): p. 101-109.

2. Chang, C.-C., et al., *Multi-component signal decomposition techniques for structural health monitoring.* Proc. SPIE, 2005. **5765**: p. 873.

3. Chang, C.-C., K.W. Sze, and Z. Sun, *Structural damage assessment using principal component analysis.* Proc. SPIE, 2004. **5394**: p. 438-445.

4. Chao, S.-H. and C.-H. Loh, *Application of SVD Techniques to Structural Damage Detection.* Structural Health Monitoring, 2012.

5. De Boe, P. and J.-C. Golinval, *Principal Component Analysis of a Piezosensor Array for Damage Localization.* Structural Health Monitoring, 2003. **2**(2): p. 137-144.

6. Elsner, J.B. and A.A. Tsonis, *Singular Spectrum Analysis: A New Tool in Time Series Analysis* 1996: Plenum Press.

7. Feeny, B.F., *ON PROPER ORTHOGONAL CO-ORDINATES AS INDICATORS OF MODAL ACTIVITY.* Journal of Sound and Vibration, 2002. **255**(5): p. 805-817.

8.   Fish, J. and T. Belytschko, *A First Course in Finite Elements* 2007: Wiley.

9.   Golyandina, N., V.V. Nekrutkin, and A.A. Zhigljavsky, *Analysis of Time Series Structure: SSA and Related Techniques* 2001: Chapman and Hall/CRC.

10.   Han, S. and B.F. Feeny, *Enhanced Proper Orthogonal Decomposition for the Modal Analysis of Homogeneous Structures.* Journal of Vibration and Control, 2002. **8**(1): p. 19-40.

11.   Hattori, K., et al., *Singular spectral analysis and principal component analysis for signal discrimination of ULF geomagnetic data associated with 2000 Izu Island Earthquake Swarm.* Physics and Chemistry of the Earth, Parts A/B/C, 2006. **31**(4–9): p. 281-291.

12.   Huang, J.-R., *System Identification of Degrading Hysteretic Restoring Forces of Reinforced Concrete Frames*, in *Department of Civil Engineering,*2009, National Taiwan University.

13.   Jolliffe, I.T., *Principal Component Analysis.* Vol. 2nd. 2002: Springer.

14.   Li, J.-H., *Enhancing Structural Seismic Response Insight of RC Frame by Time-Frequency Decomposition*, in *Department of Civil Engineering,*2011, National Taiwan University.

15. Liu, Y.-C., *Application of Covariance Driven Stochastic Subspace Identification Method*, in *Department of Civil Engineering,*2011, National Taiwan University.

16. Mao, C.-H., *Nonlinear System Identification Method for Structural Health Monitoring: Techniques for the Detection of Nonlinear Indicators*, in *Department of Civil Engineering,*2009, National Taiwan University.

17. Moskvina, V. and A. Zhigljavsky, *An Algorithm Based on Singular Spectrum Analysis for Change-Point Detection.* Communications in Statistics - Simulation and Computation, 2003. **32**(2): p. 319-352.

18. Pearson, K., *LIII. On lines and planes of closest fit to systems of points in space.* Philosophical Magazine Series 6, 1901. **2**(11): p. 559-572.

19. Pelosi, G., *The finite-element method, Part I: R. L. Courant [Historical Corner].* Antennas and Propagation Magazine, IEEE, 2007. **49**(2): p. 180-182.

20. Takens, F., *Dynamical systems and turbulence Warwick 1980.* 1981. **898**: p. 366-381.

21. Tselentis, G.A. and P. Paraskevopoulos, *Site response analysis of Vartholomio W-Greece from singular spectrum analysis of microtremor and weak motion data.* Soil Dynamics and Earthquake Engineering, 2010. **30**(5): p. 378-394.

22. Van Overschee, P. and B.L.R. De Moor, *Subspace Identification for Linear Systems: Theory - Implementation - Applications*1996, Boston / London / Dordrecht: Kluwer Academic Publishers.

23. Vanlanduit, S., et al., *A robust singular value decomposition for damage detection under changing operating conditions and structural uncertainties.* Journal of Sound and Vibration, 2005. **284**(3–5): p. 1033-1050.

24. Vautard, R., P. Yiou, and M. Ghil, *Singular-spectrum analysis: A toolkit for short, noisy chaotic signals.* Physica D: Nonlinear Phenomena, 1992. **58**(1–4): p. 95-126.

25. Verhaegen, M., *Identification of the deterministic part of MIMO state space models given in innovations form from input-output data.* Automatica, 1994. **30**(1): p. 61-74.

26. Weng, J.-H., *Application of Subspace Identification in System Identification and Structural Damage Detection*, in *Department of Civil Engineering,*2010, National Taiwan University.

27. Weng, J.-H. and C.-H. Loh, *Recursive subspace identification for on-line tracking of structural modal parameter.* Mechanical Systems and Signal Processing, 2011. **25**(8): p. 2923-2937.

28.   Zhang, Y., et al., *Modal parameter identification using response data only.*

Journal of Sound and Vibration, 2005. **282**(1–2): p. 367-380

.

Table 3-1 Physical parameters of shake table test (Freq. refer to Mao)

Case ID.	Excitation Type	PGA (gal)	Max Absolute Accel. (gal)	Max. Story Drift Ratio	Equivalent Linear System Freq.	
					Start Freq. (Hz)	End Freq. (Hz)
WN1	White Noise	29	24	0.06	5.82	
RCF6-1	TCU082	622	1225	1.35	5.87	2.87
WN2	White Noise	30	18	0.04	3.12	
RCF6-2	TCU082	800 (expected)	-	-	-	-
WN3	White Noise	32	13	0.05	2.47	
RCF6-3	TCU082	1041	1368	2.69	2.6	2.45
WN4	White Noise	30	15	0.06	2.67	
RCF6-4	TCU082	1103	1271	2.94	2.35	2.35
WN5	White Noise	32	14	0.05	2.57	
RCF6-5	TCU082	1004	1261	2.87	2.35	2.36
WN6	White Noise	27	15	0.07	2.57	
RCF6-6	TCU082	803	1059	2.45	2.36	2.39
WN7	White Noise	30	13	0.06	2.52	
RCF6-7	TCU082	582	806	2.01	2.42	2.43
WN8	White Noise	32	13	0.06	2.49	

Table 3-2 White noise analysis result by SSI-COV ($C_{svd} = 0.9$)

WN Case ID.	Natural Freq. (Hz)	Damping ratio	Subspace Damage Indicator	Null-space Damage Indicator
WN1	5.76	0.04	0	0
WN2	3.07	0.08	0.79	3.317×10^{-3}
WN3	2.88	0.09	0.85	3.354×10^{-3}
WN4	2.62	0.08	0.91	3.357×10^{-3}
WN5	2.52	0.07	0.93	3.383×10^{-3}
WN6	2.46	0.07	0.94	3.373×10^{-3}
WN7	2.44	0.07	0.95	3.366×10^{-3}
WN8	2.44	0.07	0.95	3.411×10^{-3}

Table 3-3 Seismic analysis result by RSI and PCA

Seismic Case ID	RSI Frequency		PCA Modal Contribution	
	Start Freq. (Hz)	End Freq. (Hz)	First Mode (%)	Second Mode (%)
RCF6-1	5.78	3.08	99.22	0.74
RCF6-2	3.10	2.65	99.64	0.34
RCF6-3	3.16	2.5	99.52	0.47
RCF6-4	2.58	2.36	99.82	0.16
RCF6-5	2.58	2.28	99.95	0.02
RCF6-6	2.36	2.22	99.96	0.02
RCF6-7	2.43	2.35	99.95	0.03

Table 3-4 Element with oscillation principal motion by SSA

Seismic Case ID	x Direction Element	y Direction Element
RCF6-1	B_7, B_8, B_9, B_{10}	-
RCF6-2	B_1	-
RCF6-3	-	-
RCF6-4	-	-
RCF6-5	-	B_{10}
RCF6-6	-	-
RCF6-7	-	-
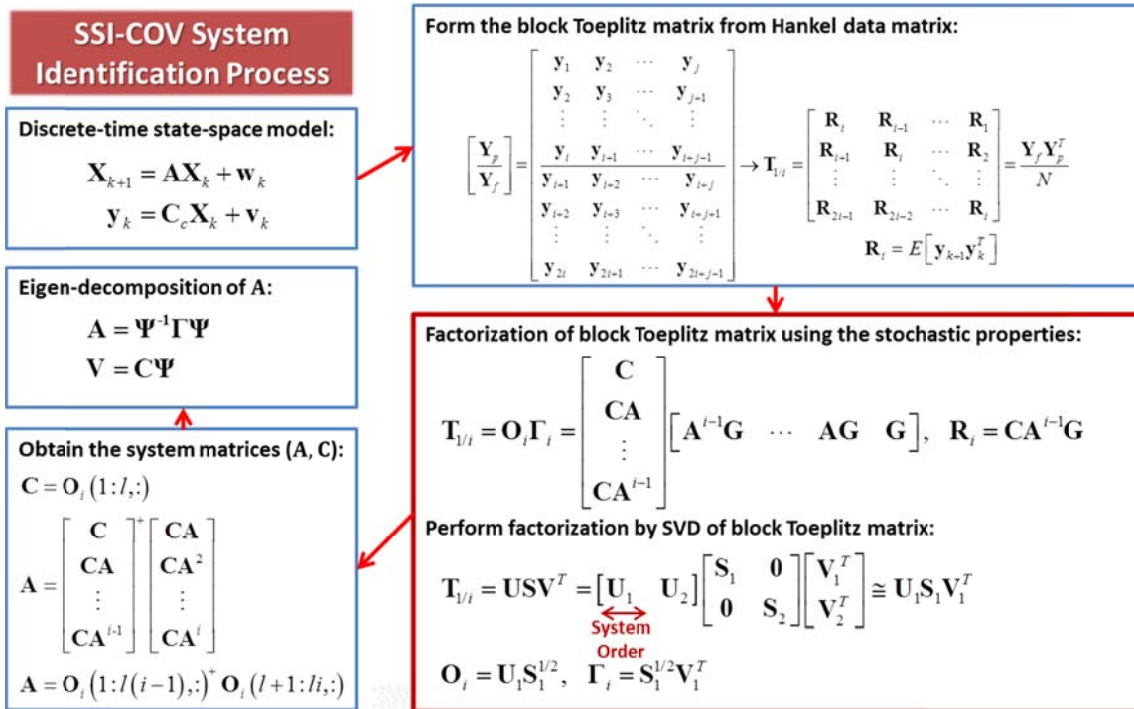
Figure 2-1 Flowchart of SSI-COV algorithm
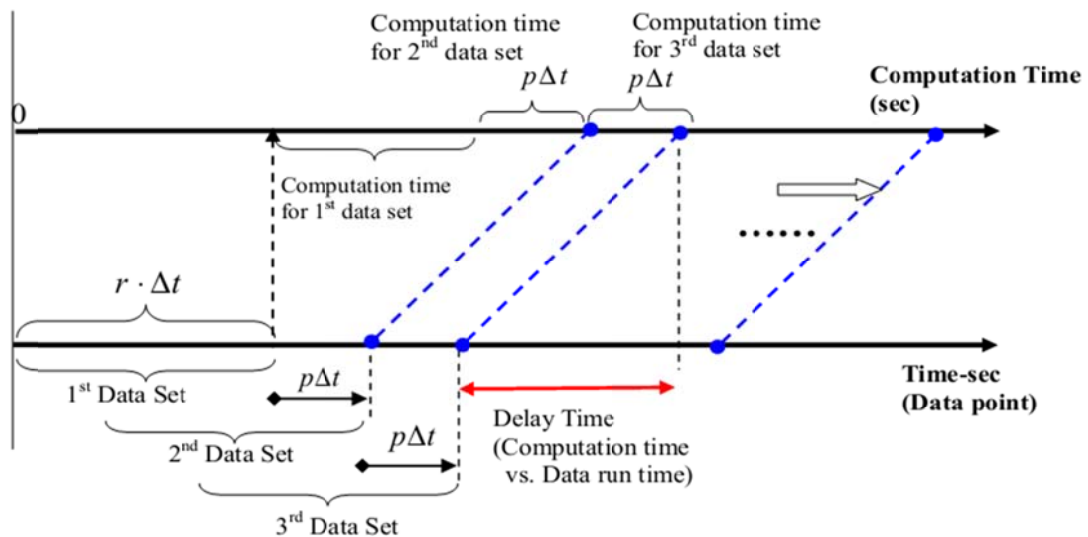
Figure 2-2 Scheme of on-line recursive identification
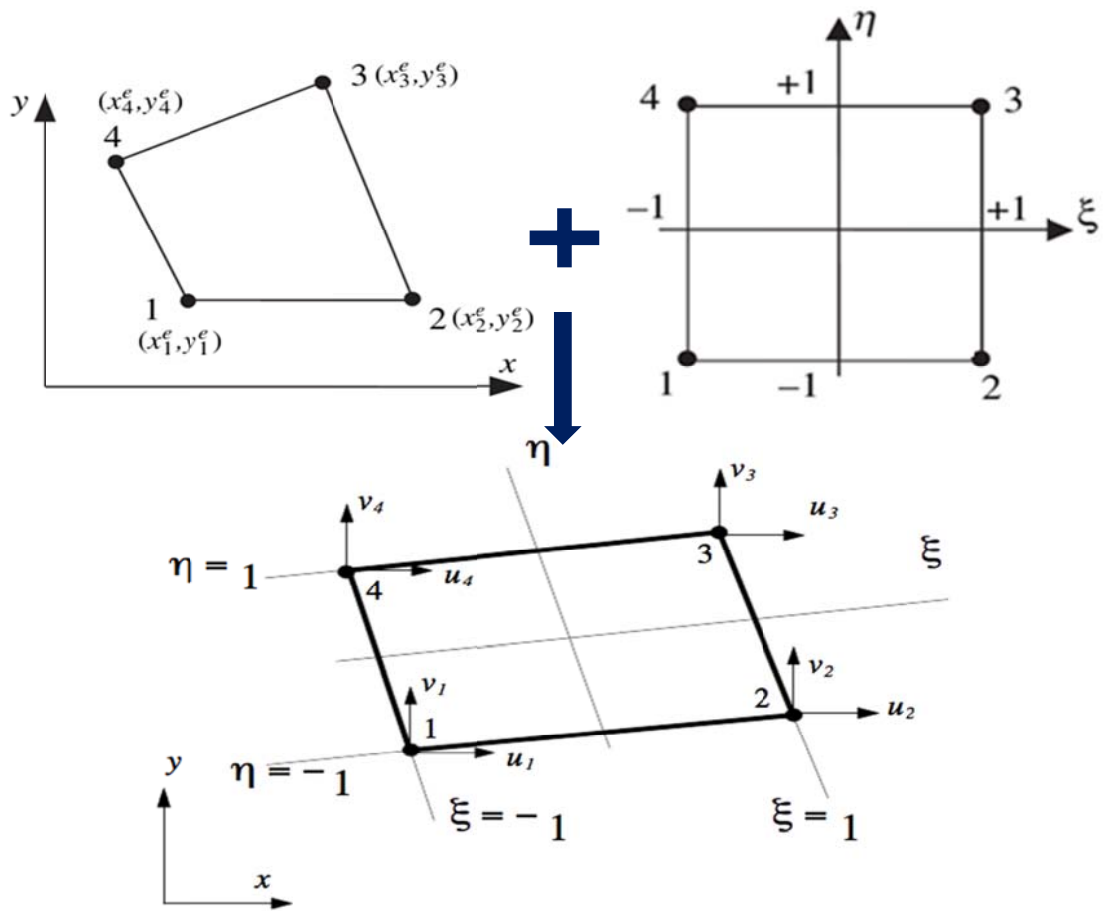
Figure 2-3 Finite element coordinate system, combines physic and natural system
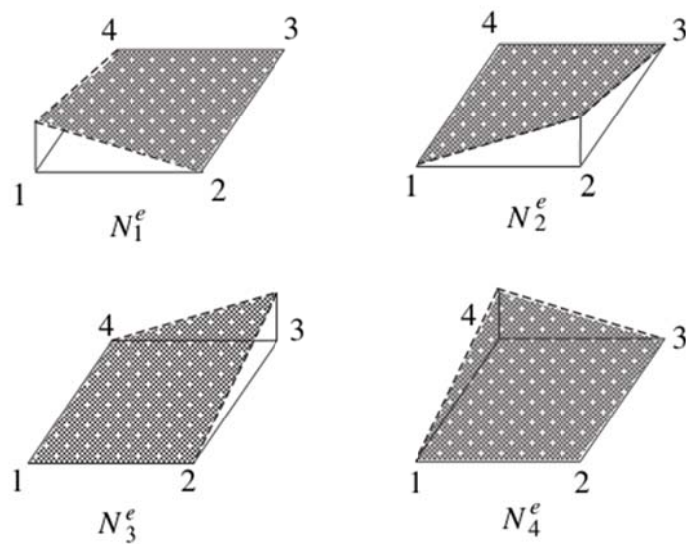
Figure 2-4 Scheme of Q4 element shape function

74
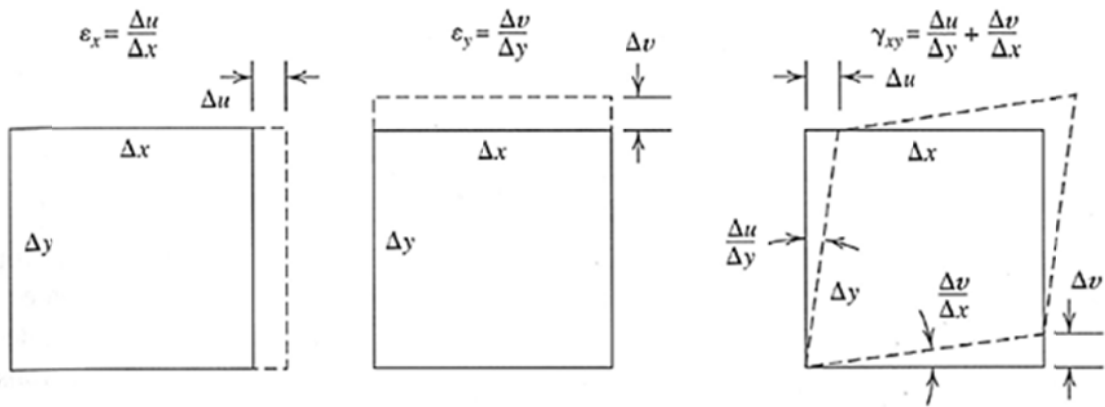
Figure 2-5 Strain definition of unit element
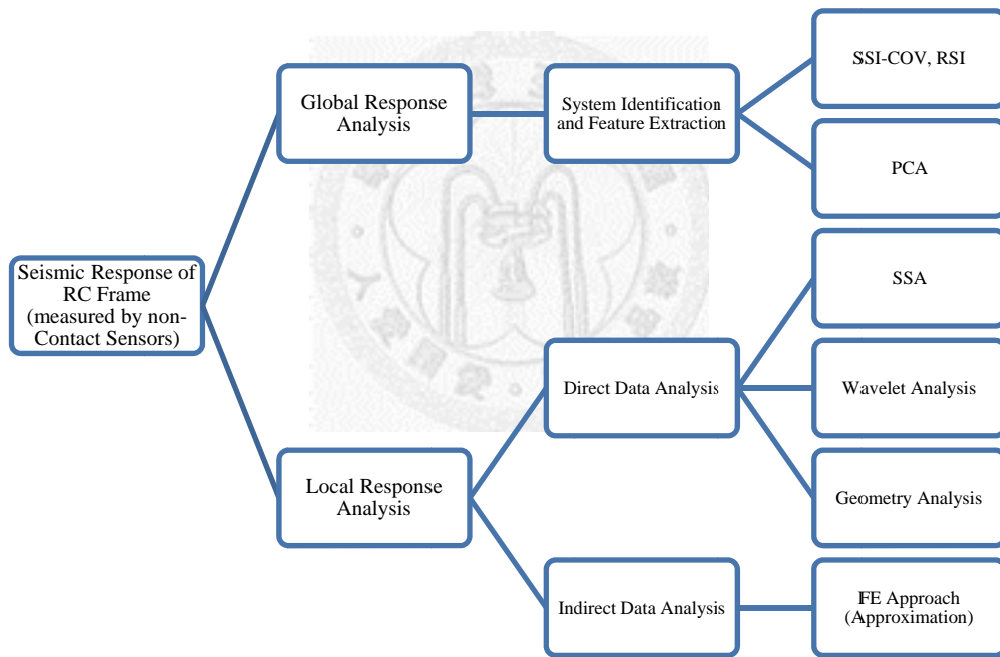
Figure 2-6 Research framework

Figure 3-1 Specimen of one-story two-bay RC frame

Design 28 days concrete compressive strength

$f_c' = 280 kgw/cm^2$

Design steel strength

$f_y = 4200 kgw/cm^2$

Lateral View

Unit: cm

Side Columns

4#4 steel bars are used as longitudinal reinforcement

Center Column

8#4 steel bars are used as longitudinal reinforcement

Beam

Top: 3#3 steel bars

Bottom: 2#3 steel bars

#3 steel bars with 10cm spacing are used as the transverse reinforcement
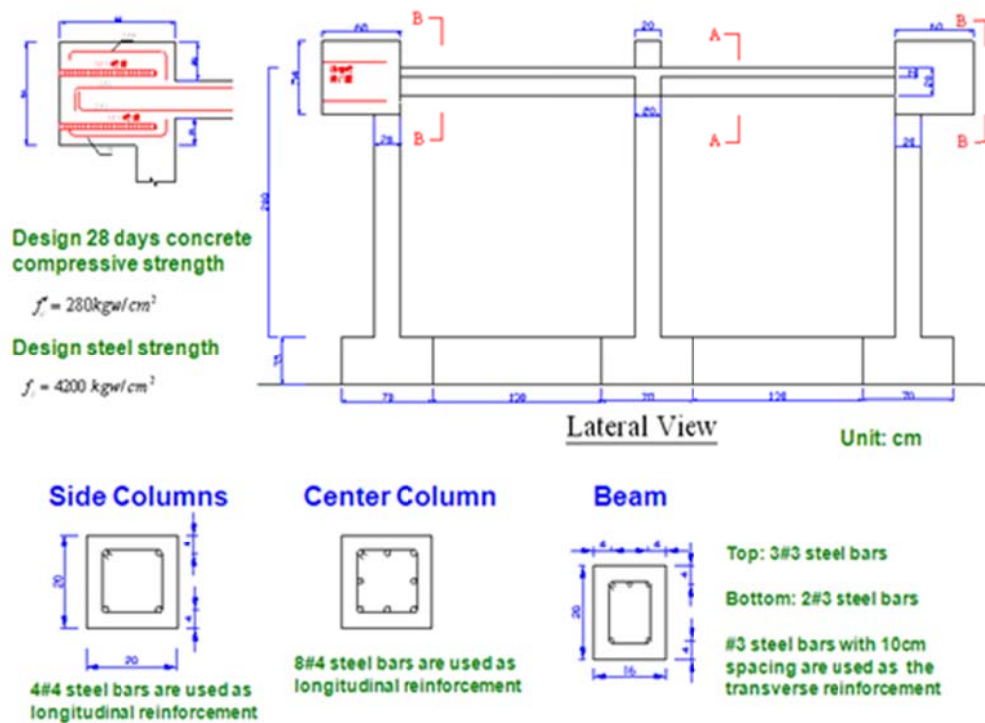
Figure 3-2 Design detail of elements and specimen diemnsion
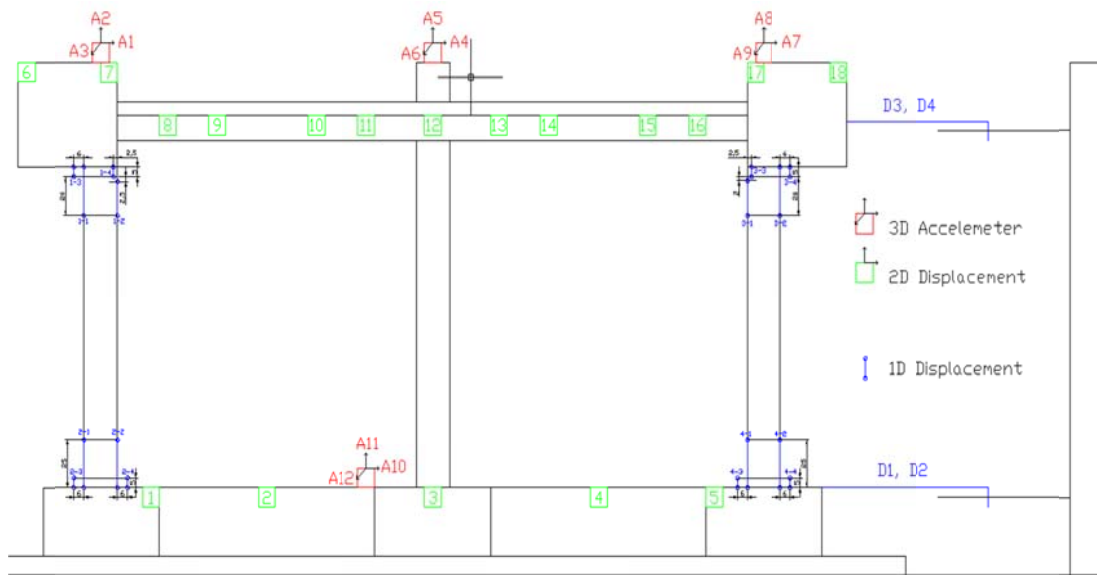
Figure 3-3 Configuration of general measuring system
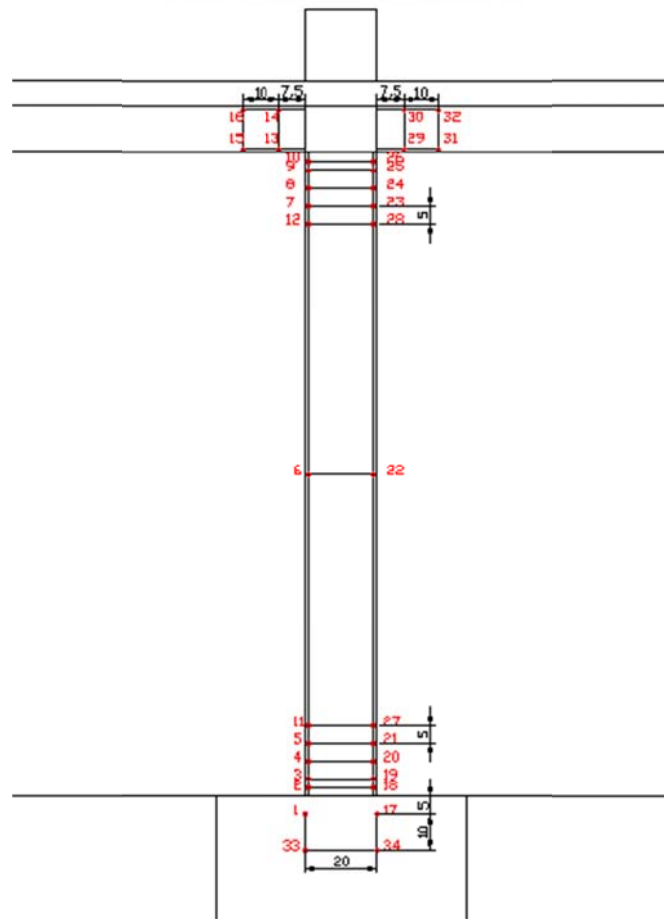
Figure 3-4 Configuration of optical measuring system

77

Figure 3-5 Optical sensing system in the shake table test
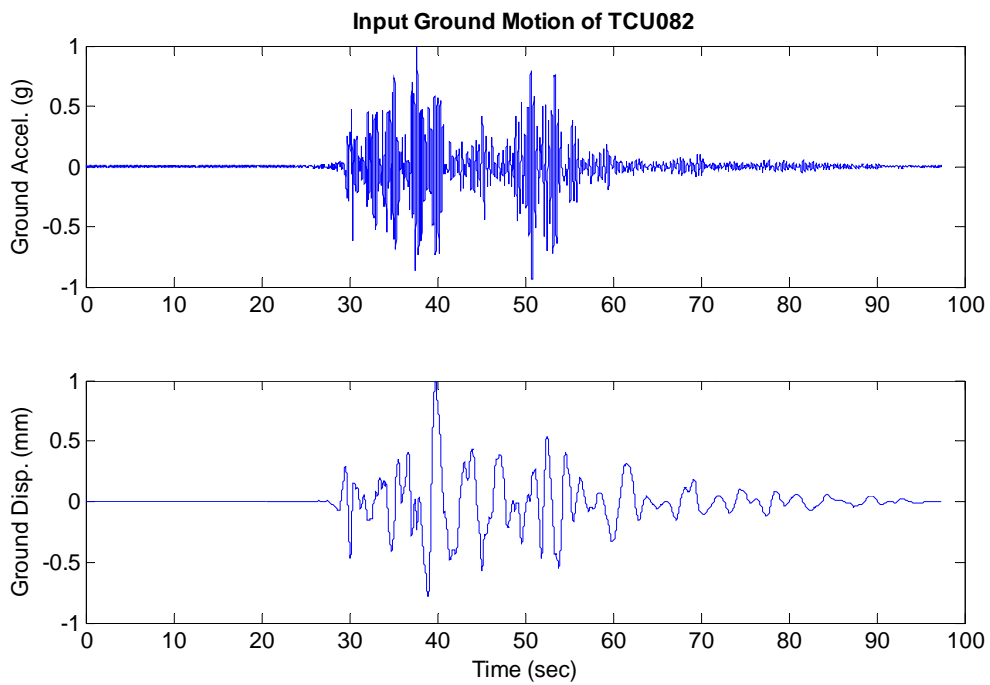
Figure 3-6 Normalized input ground motion of TCU082
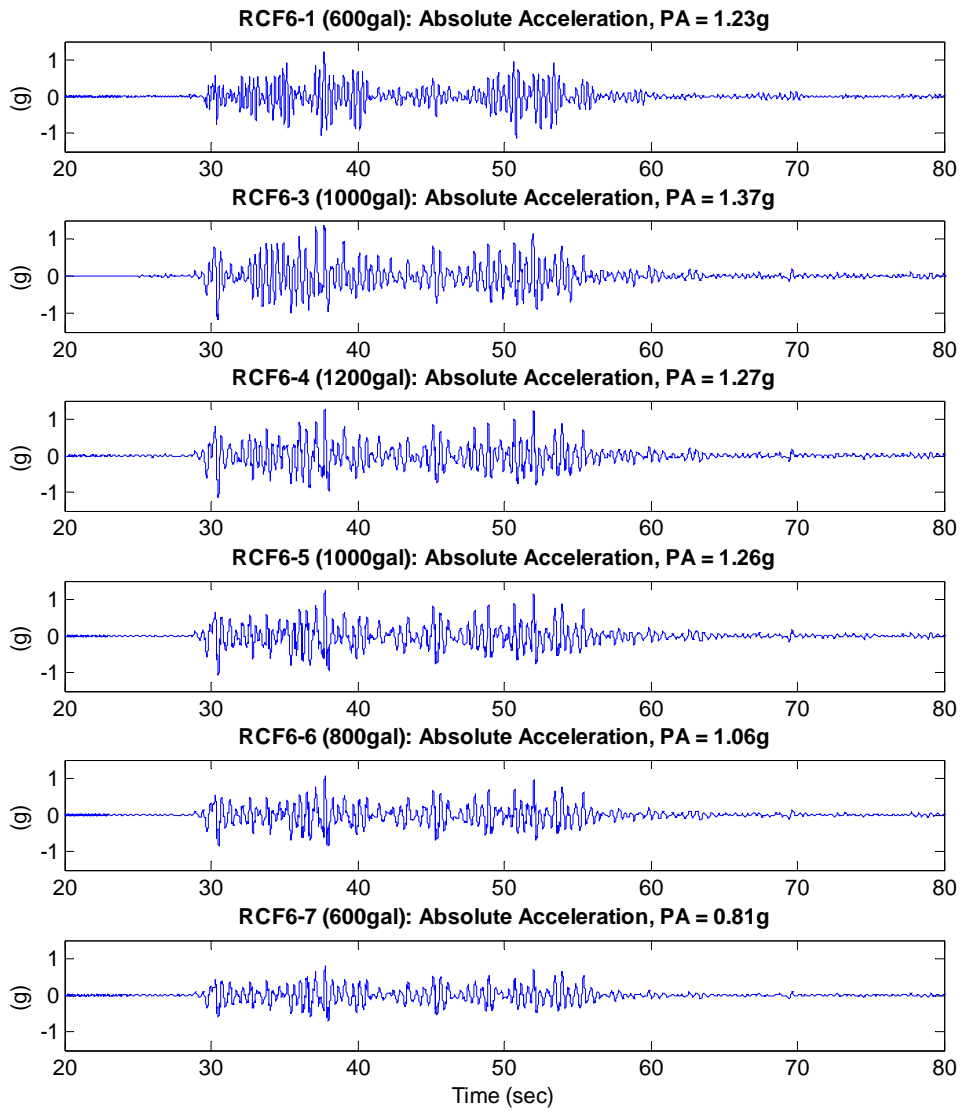
Figure 3-7 Absolute acceleration response of the series of excitations
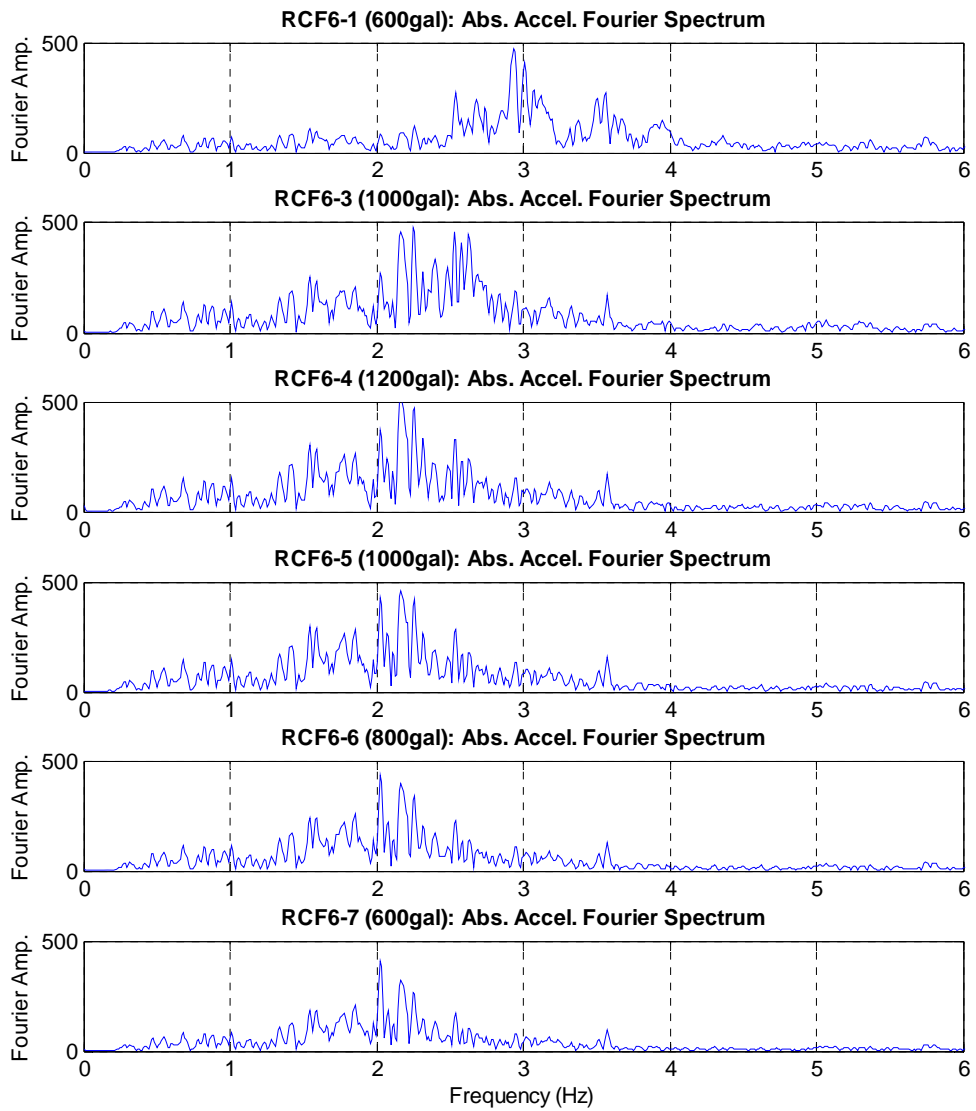
Figure 3-8 Absolute acceleration Fourier spectrum of the series of excitations
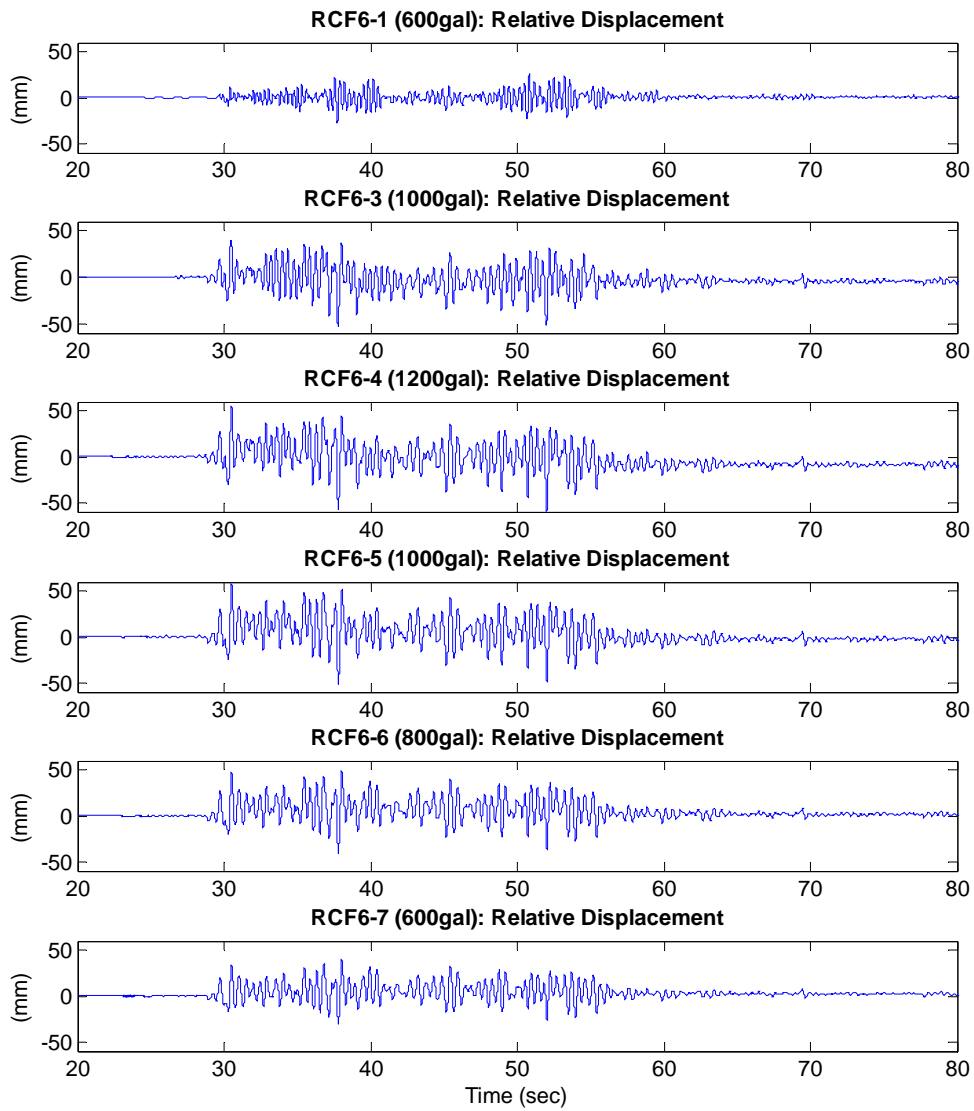
Figure 3-9 Relative displacement of the series of exciations

81
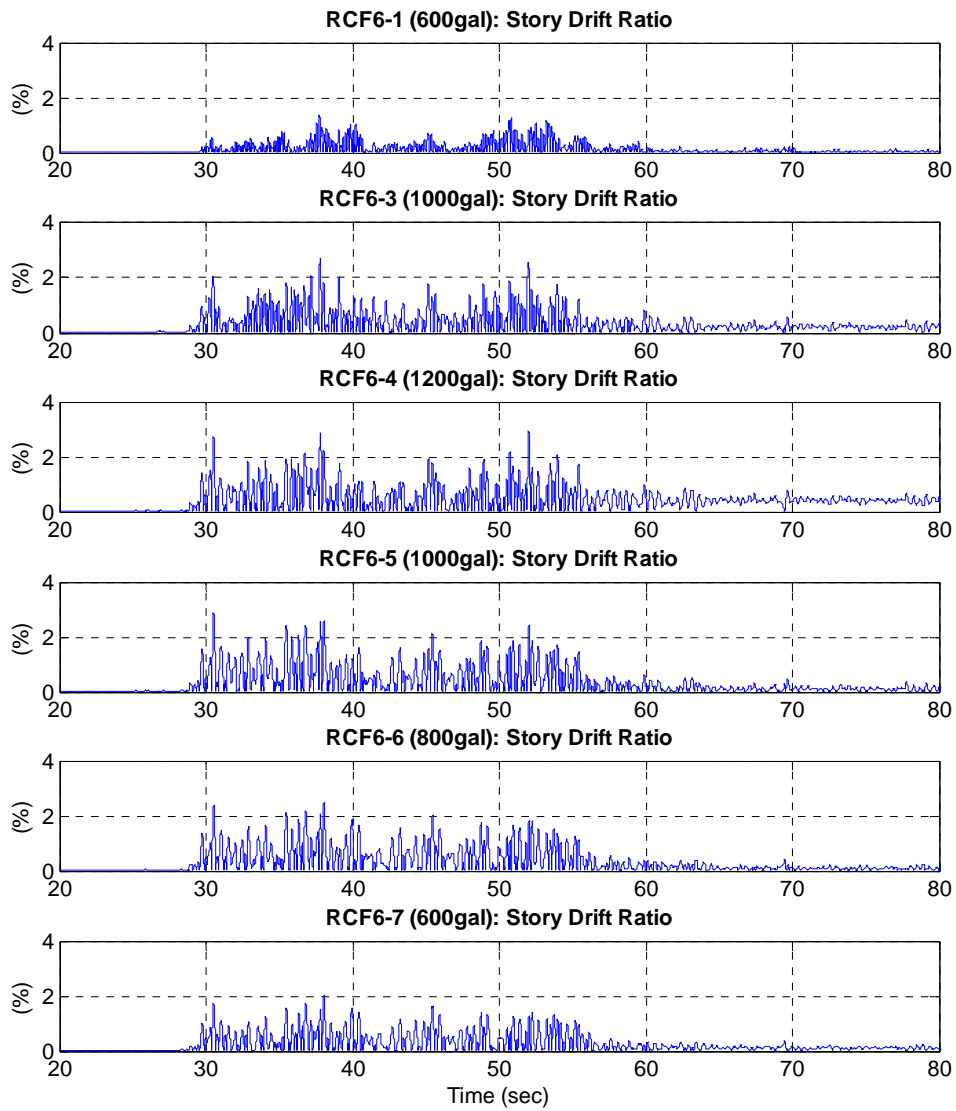
Figure 3-10 Inter story drift ratio of the series of excitations
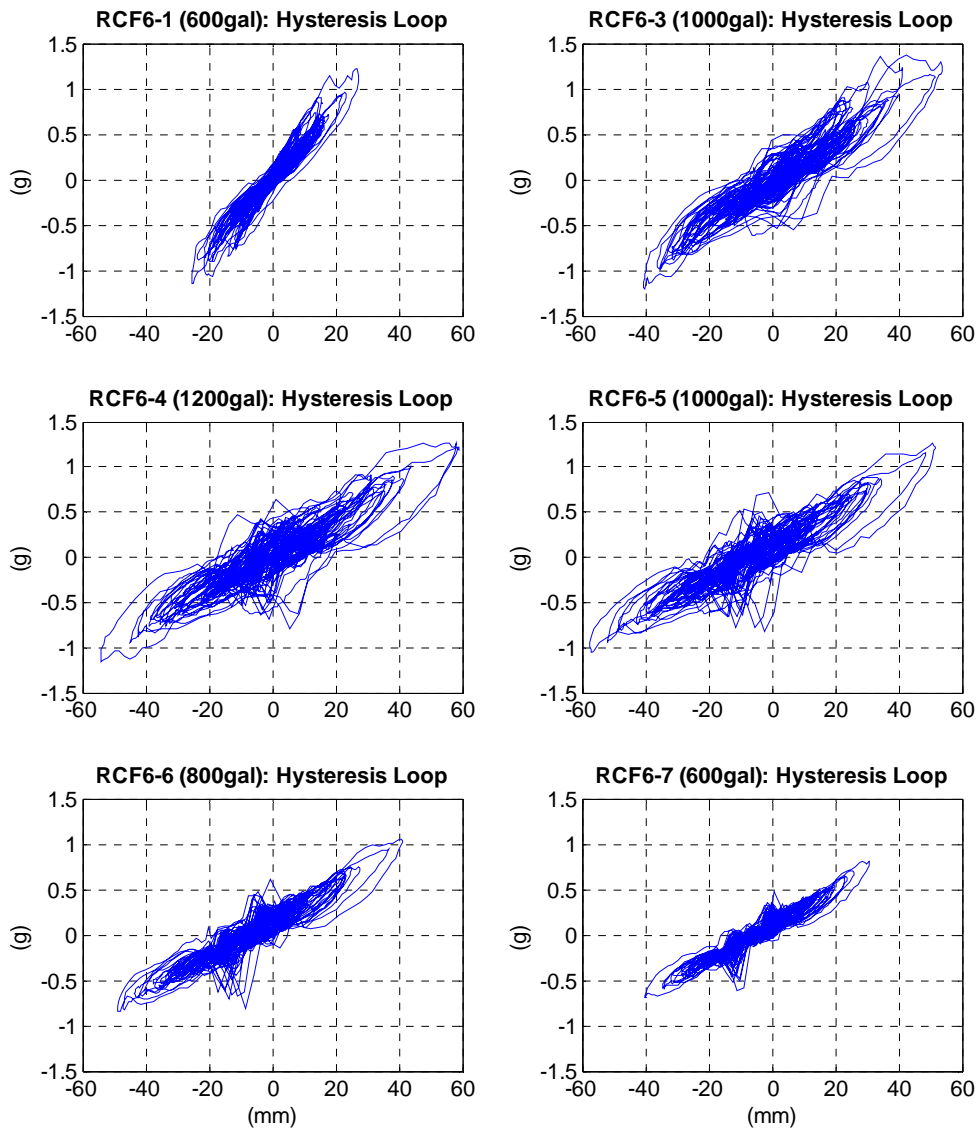
Figure 3-11 Hysteresis behavior of the series of excitations
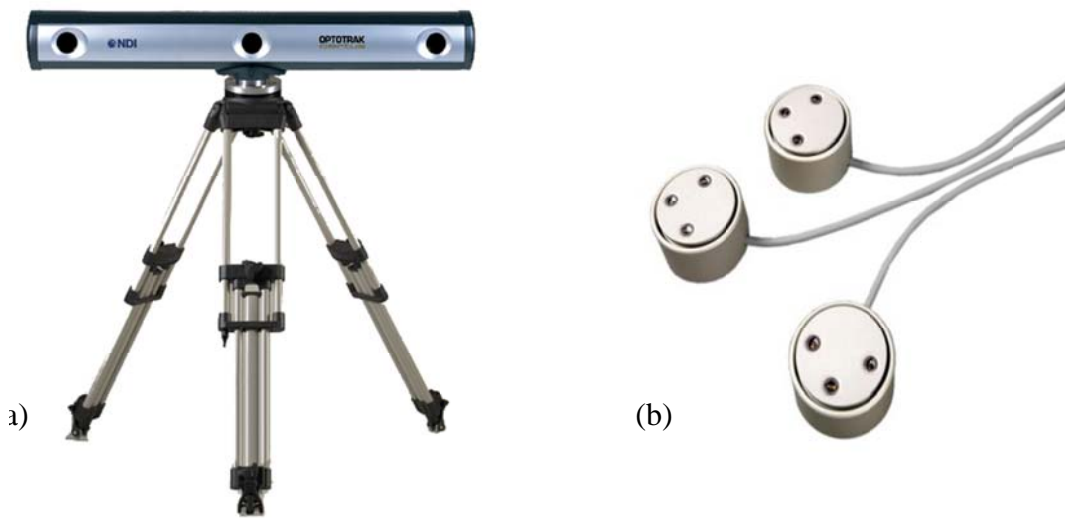
Figure 3-12 DMM of NDI Inc.: (a) Optical tracker and (b) targets.
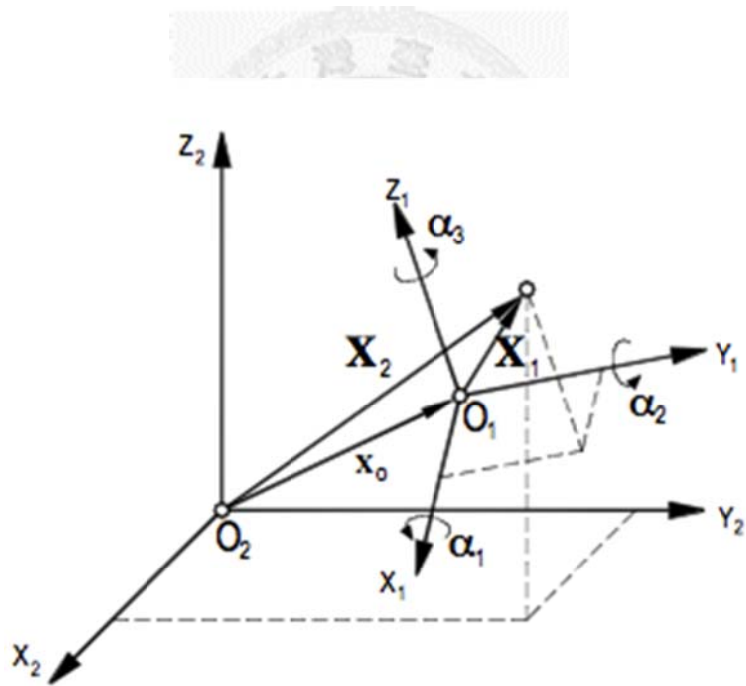
Figure 3-13 Scheme of two different coordinate systems
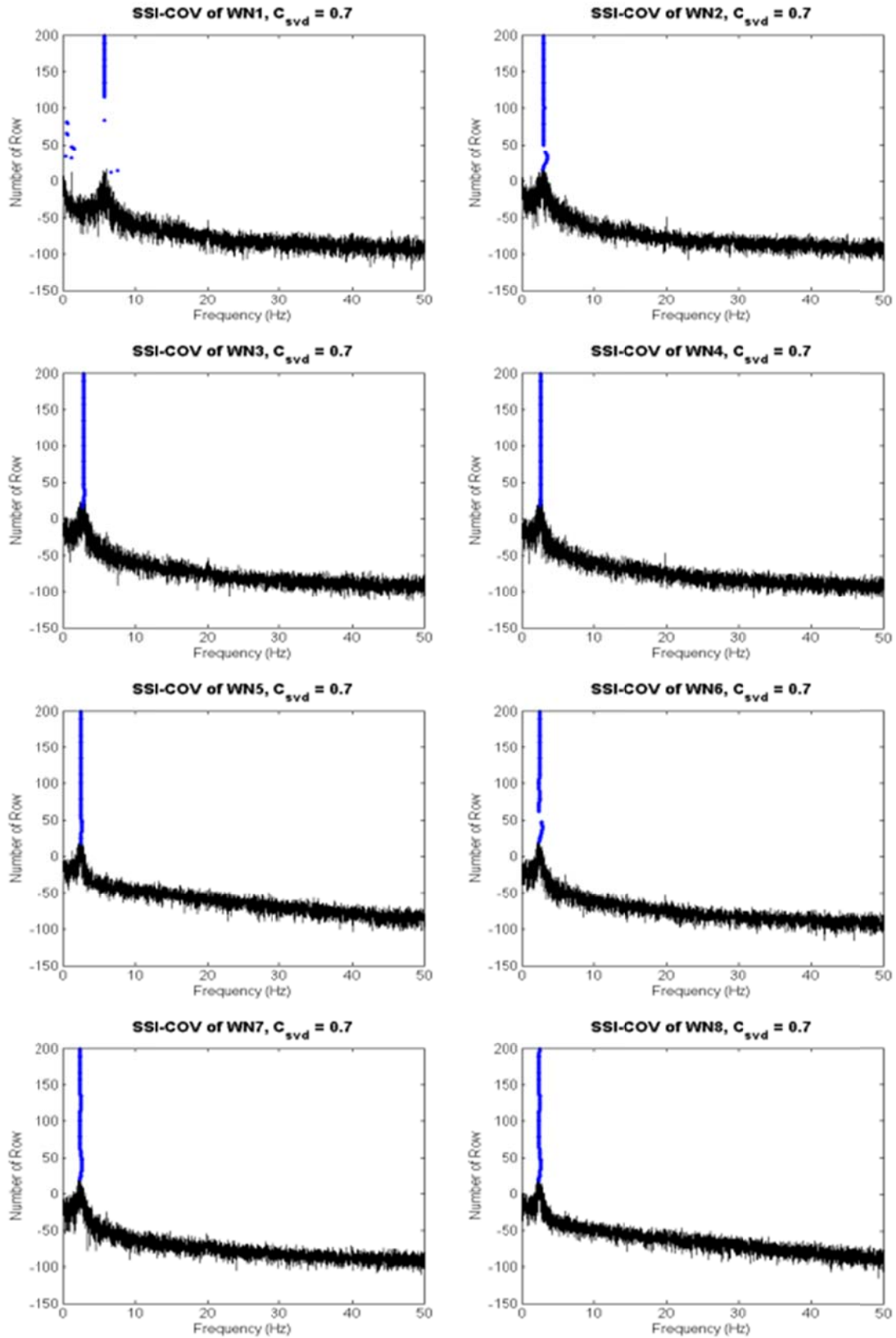
Figure 3-14 System natural frequency stability diagram, $C_{svd} = 0.7$
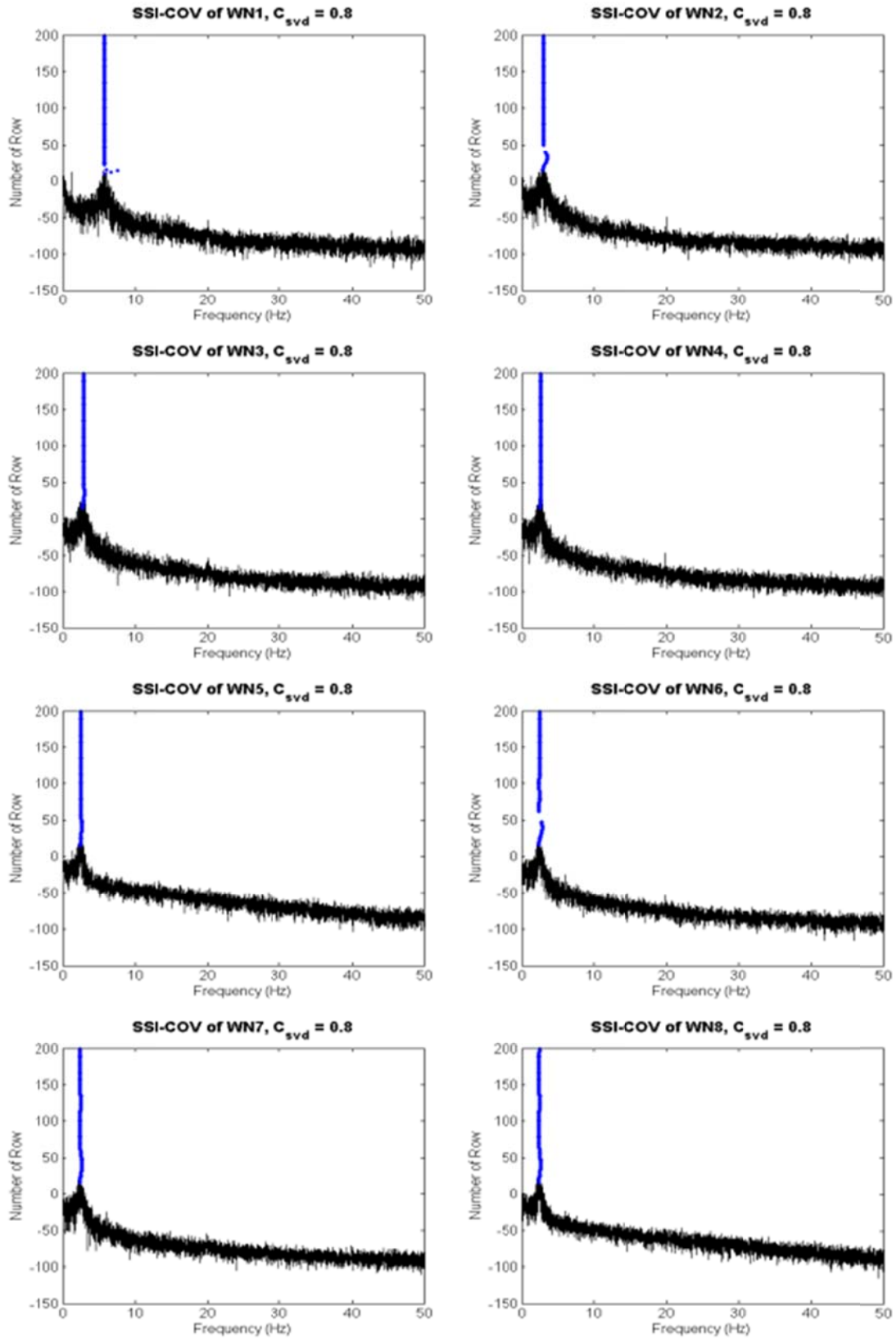
Figure 3-15 System natural frequency stability diagram, $C_{svd} = 0.8$
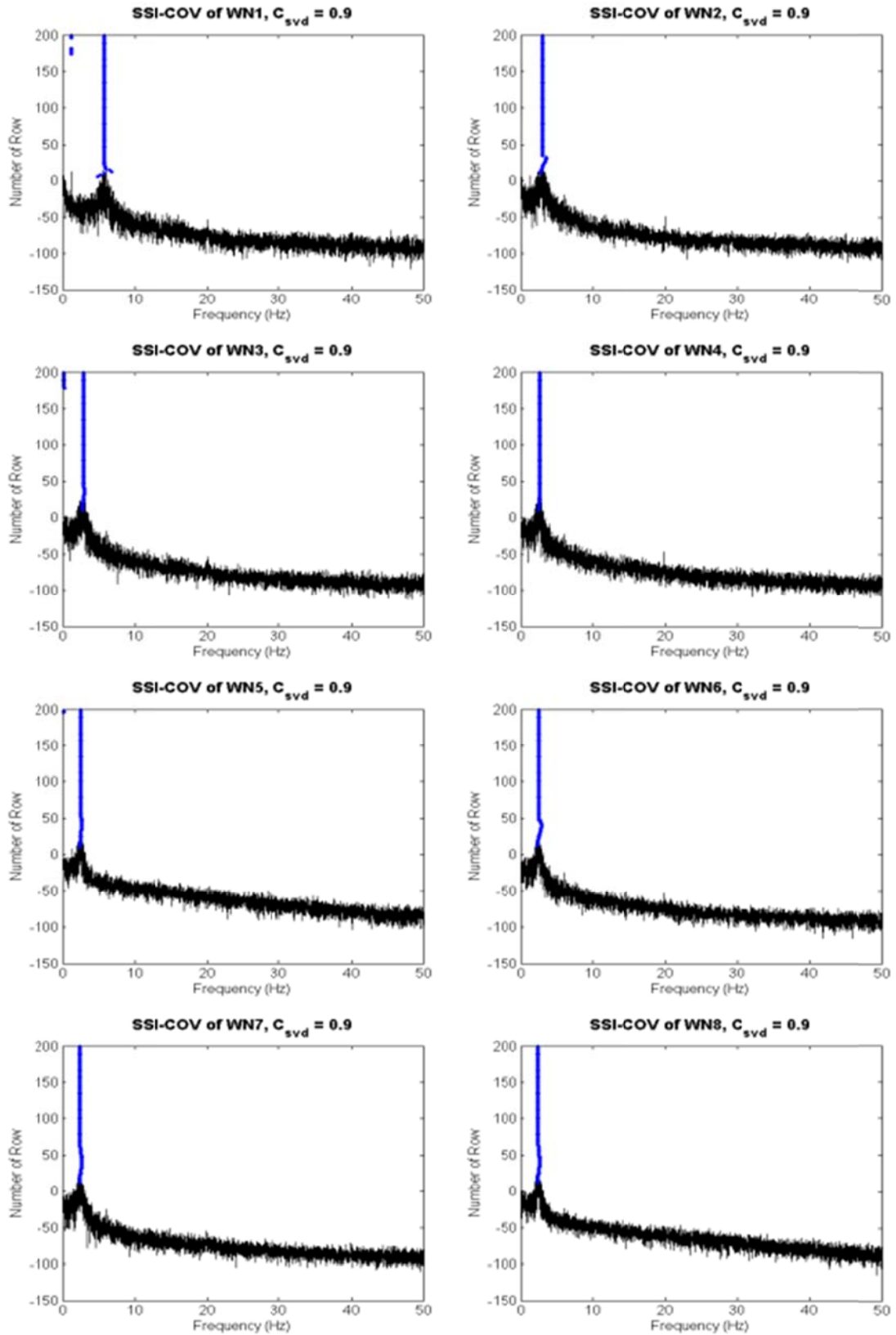
Figure 3-16 System natrual frequency stability diagram, $C_{svd} = 0.9$
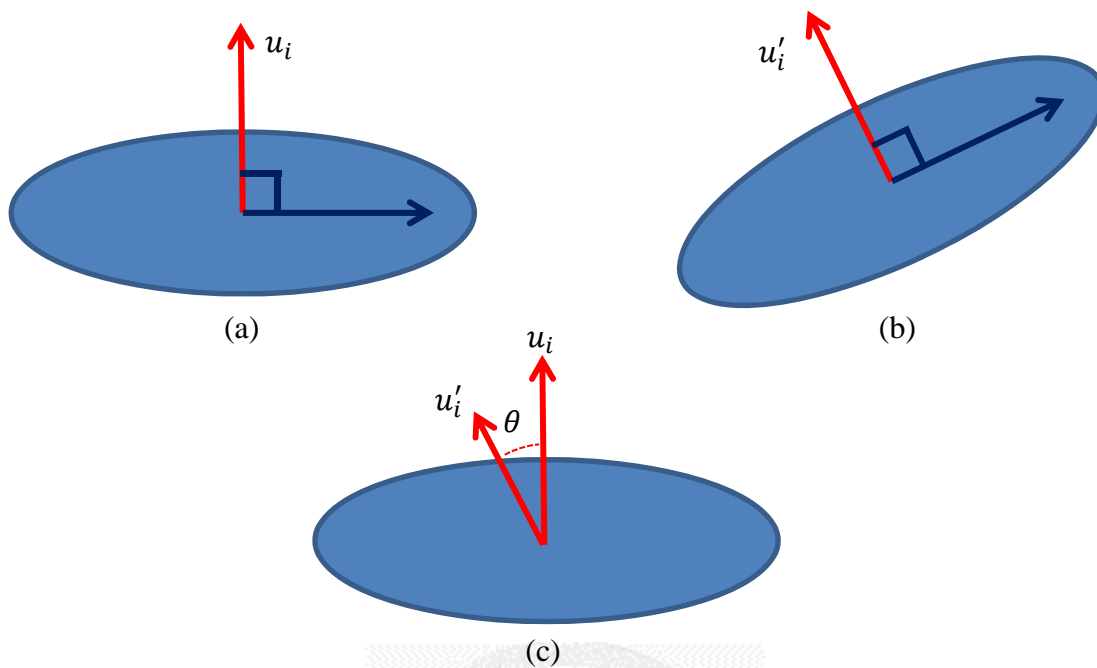
Figure 3-17 Scheme of space difference (a) reference, (b) current, and (c) compare
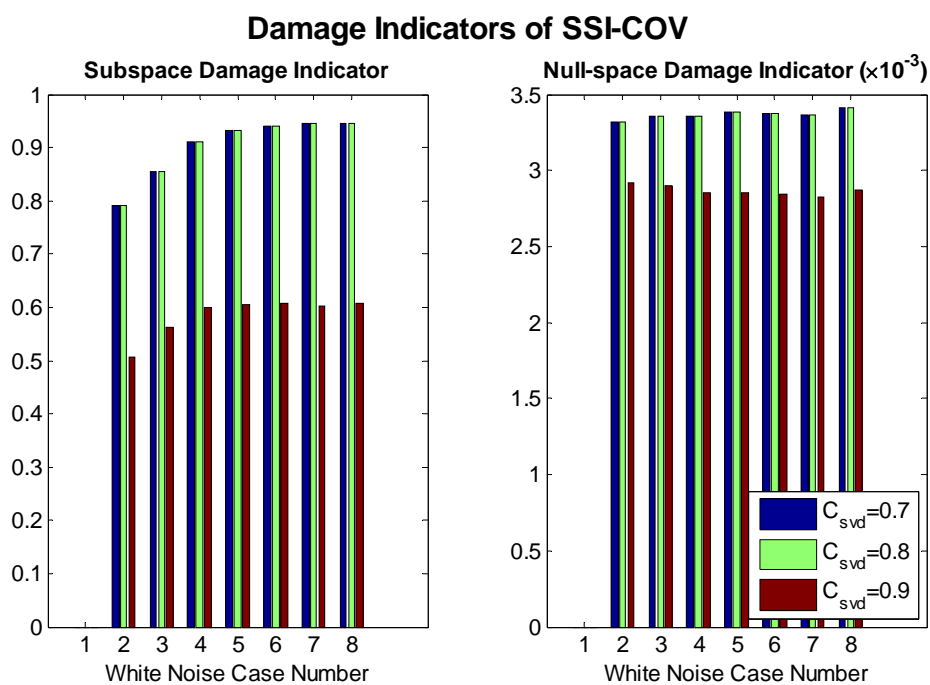
Figure 3-18 Damage indicators of space projection
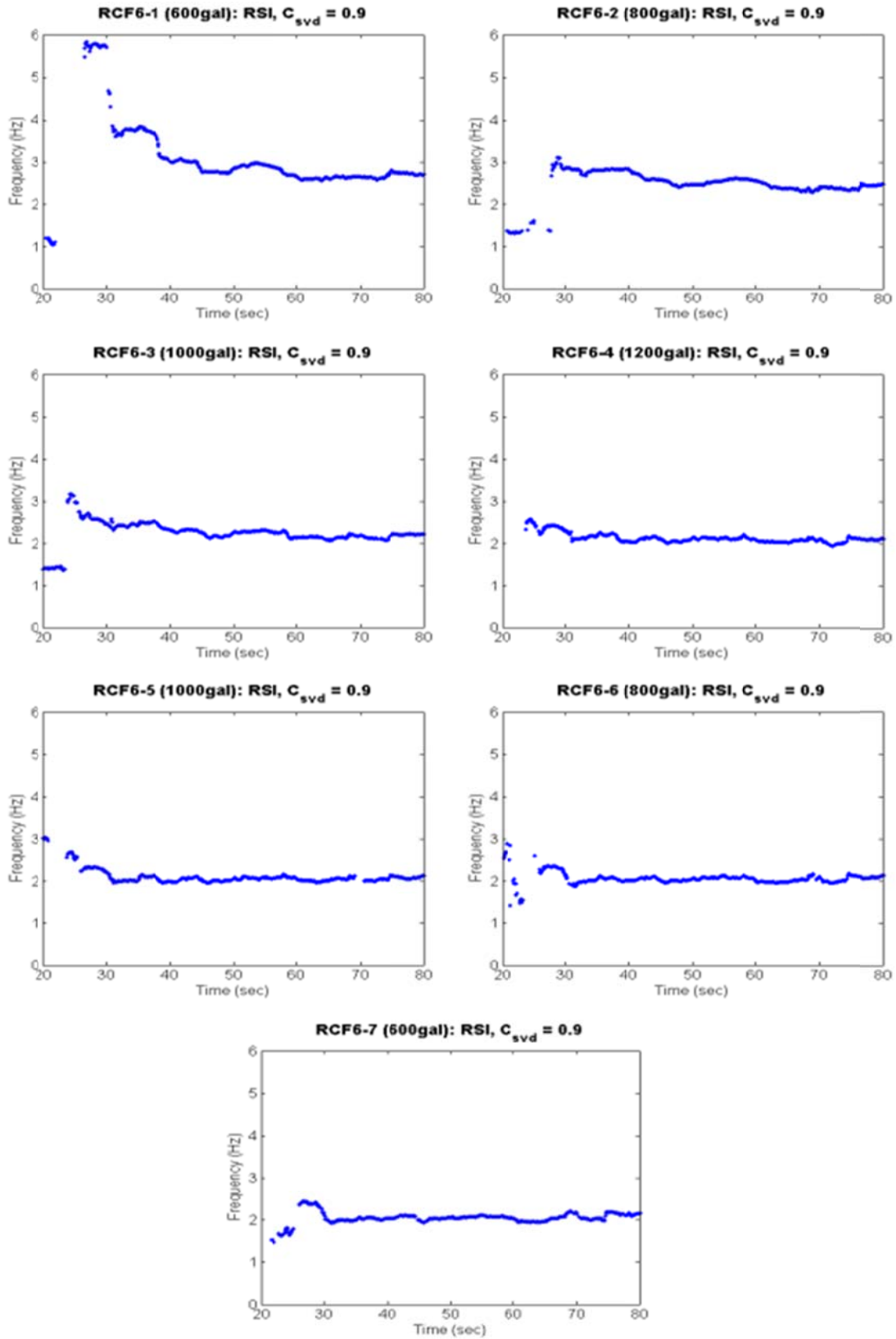
Figure 3-19 System natural frequency during seismic loading, $C_{svd} = 0.9$
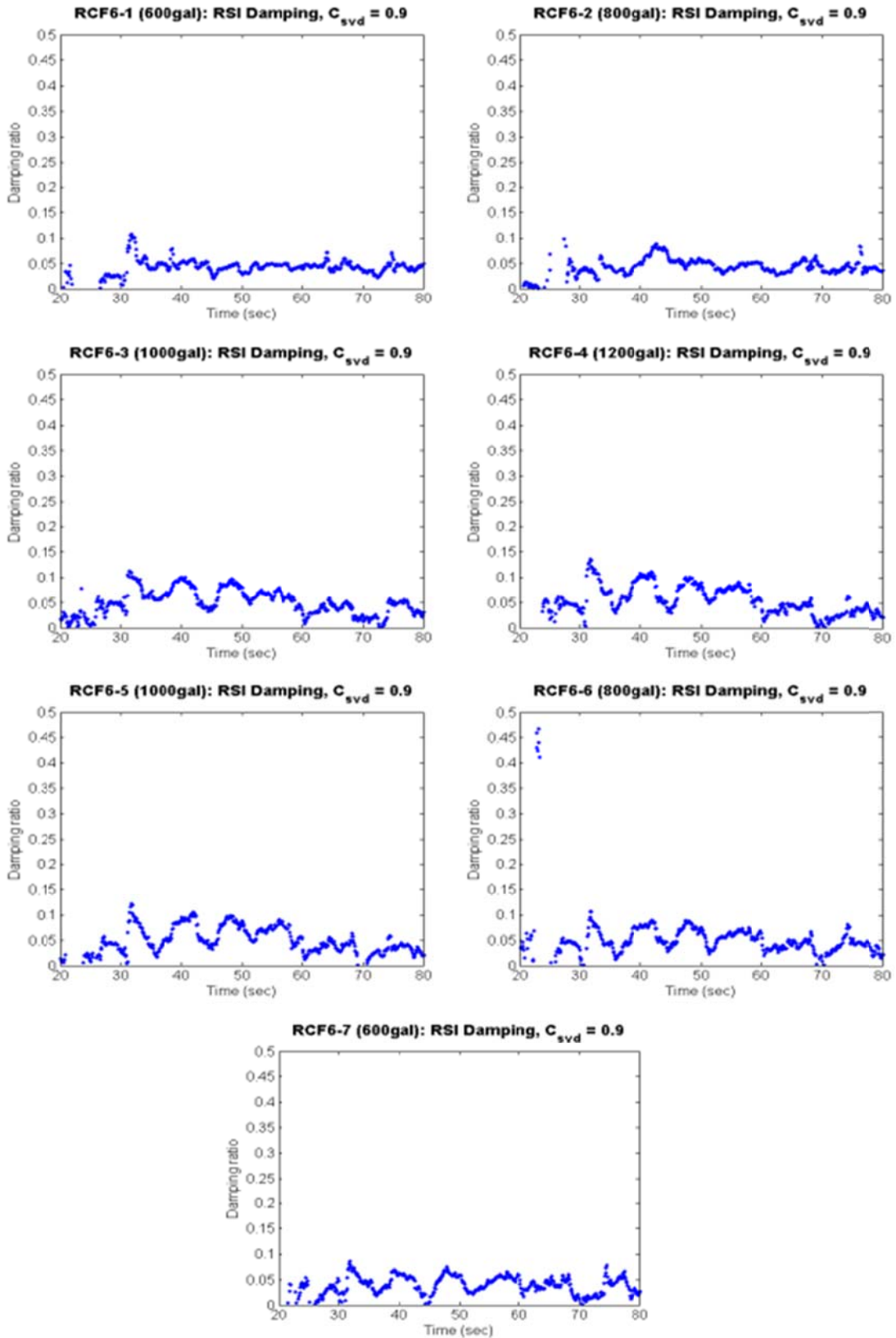
Figure 3-20 System damping ratio during seismic loading, $C_{svd} = 0.9$
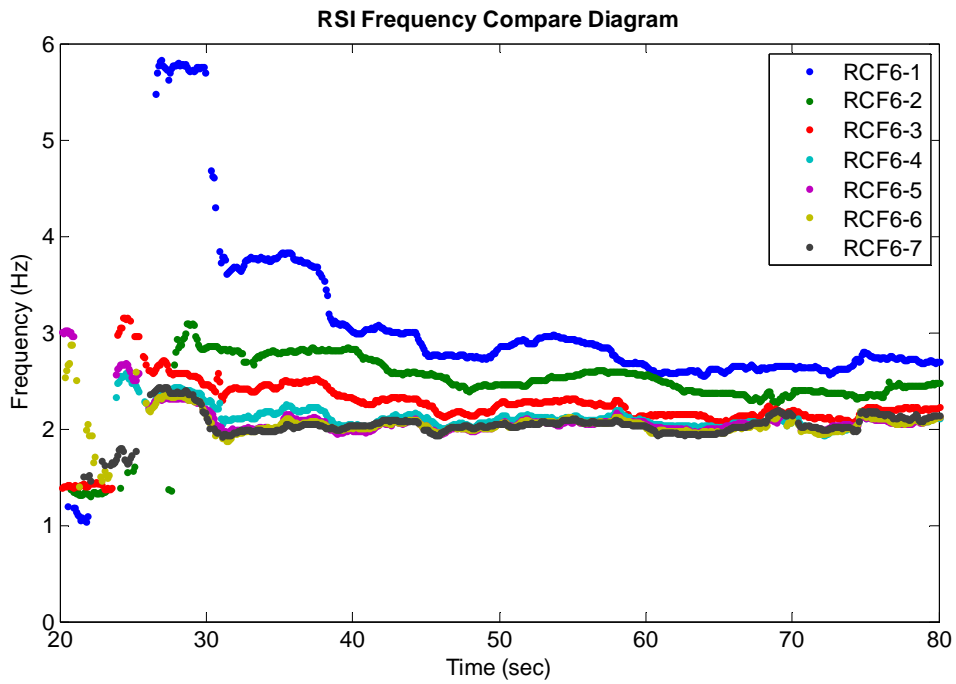
Figure 3-21 System natural frequency compare diagram

Instantaneous Phase Analysis
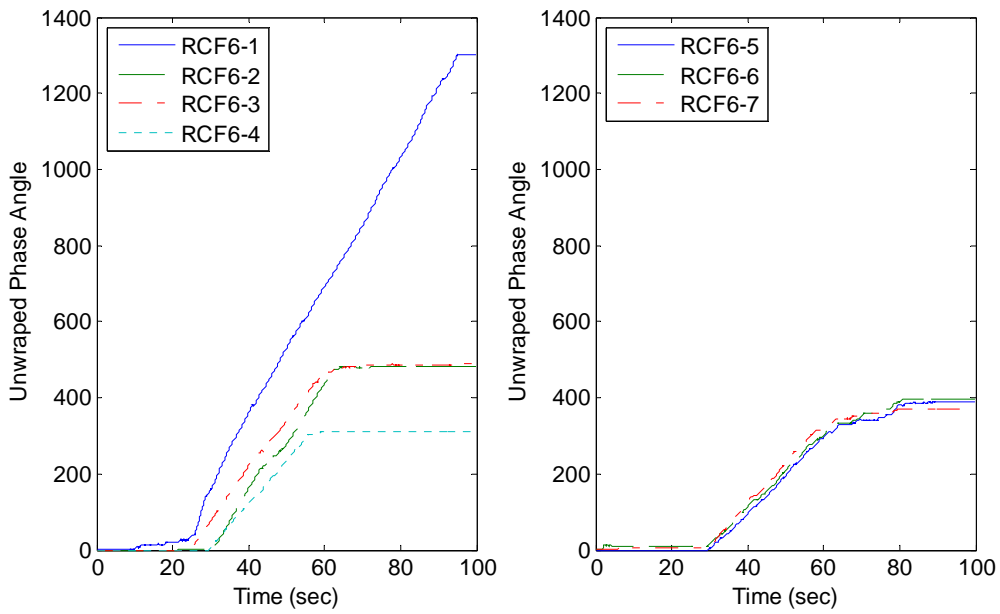
Figure 3-22 Instantaneous phase analysis
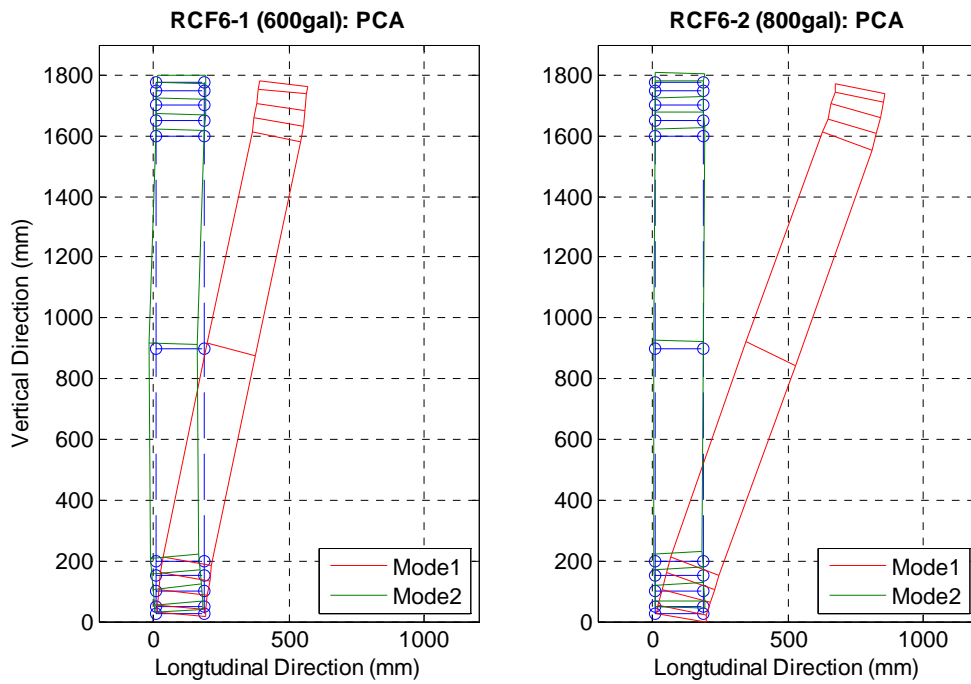
Figure 3-23 Effective mode shape (a)
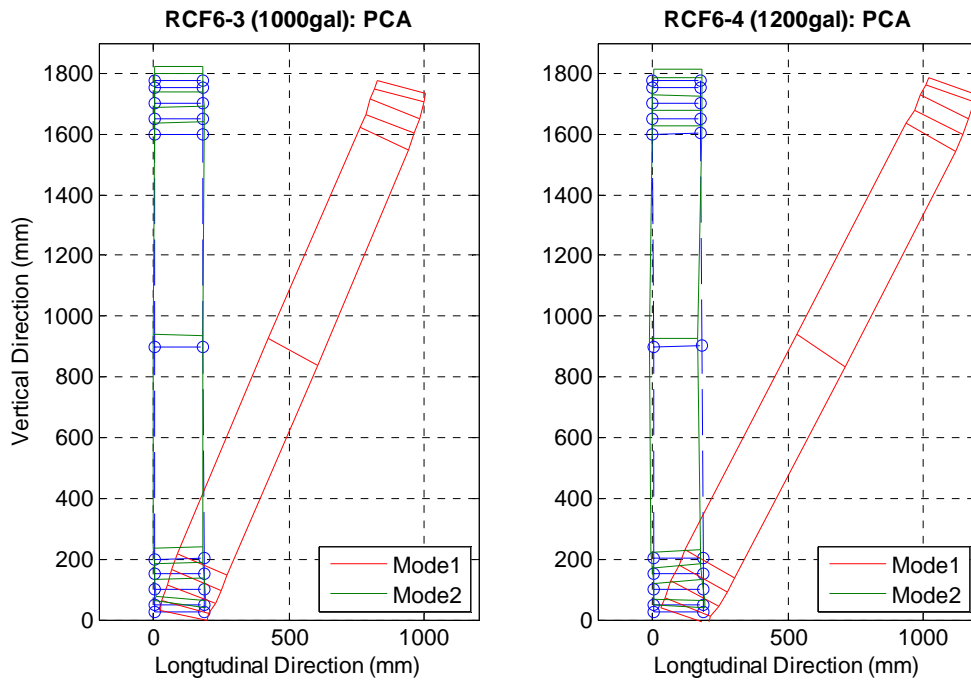
Figure 3-24 Effective mode shape (b)
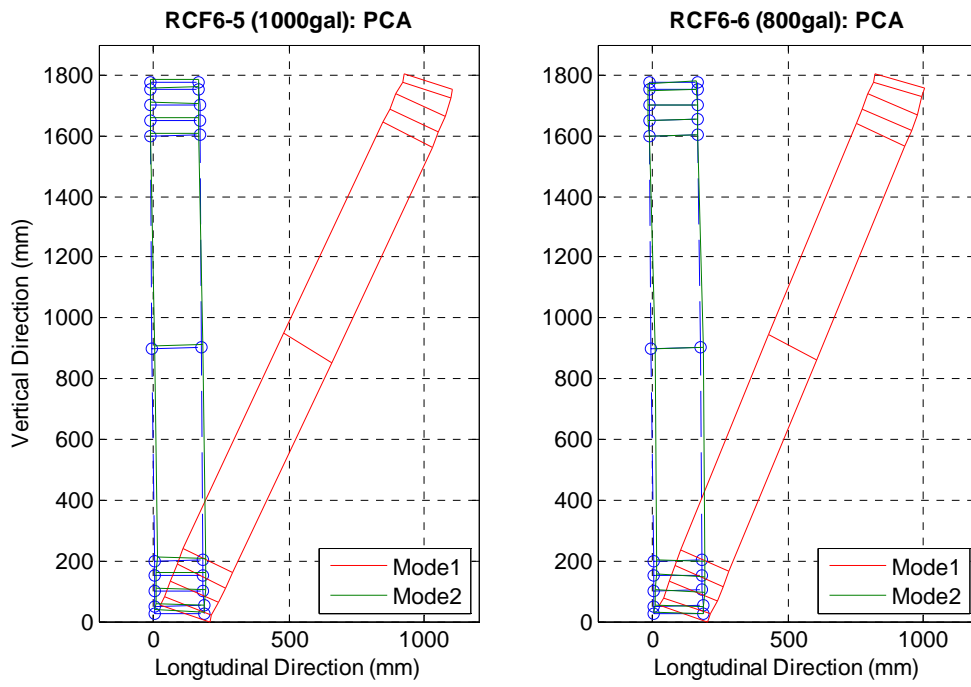
Figure 3-25 Effective mode shape (c)
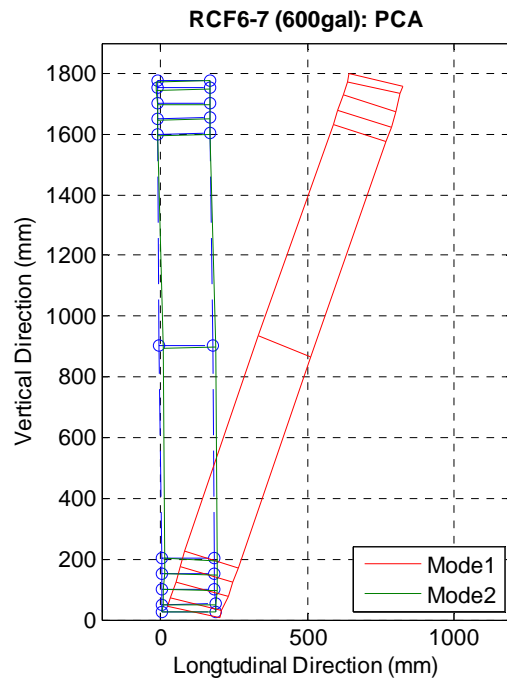
Figure 3-26 Effective mode shape (d)

93
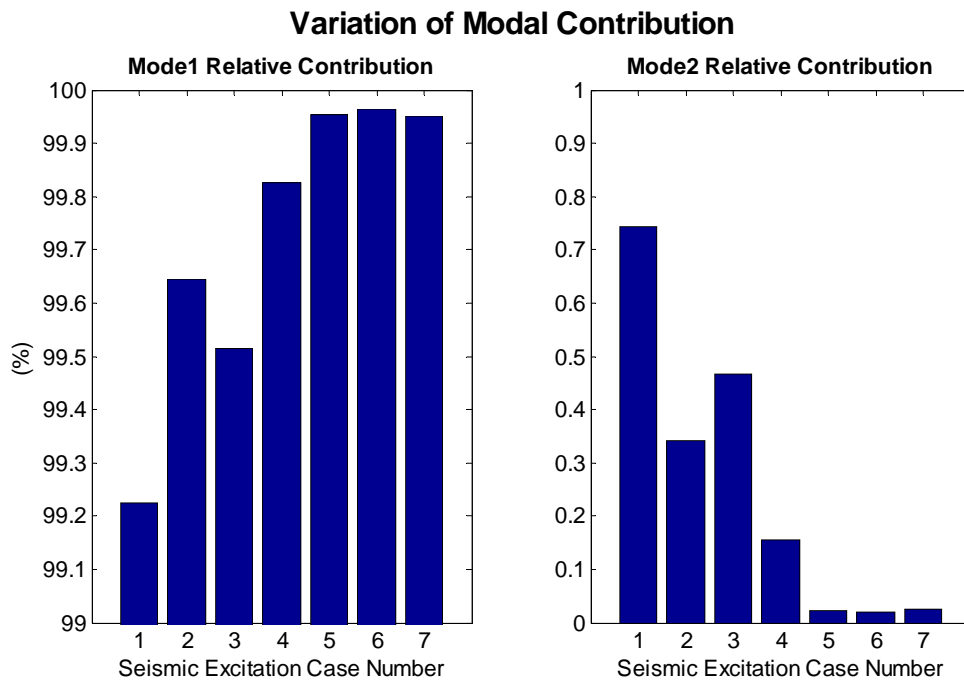
Figure 3-27 Variation of modal contribution
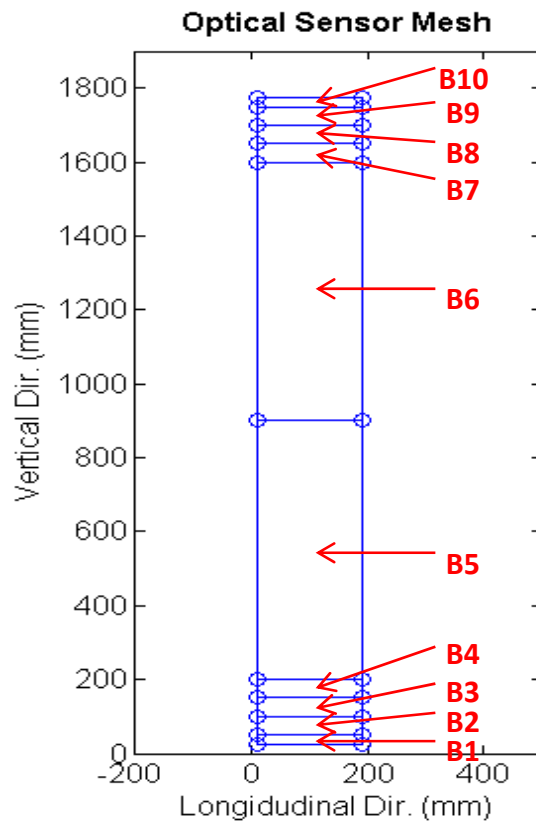
Figure 3-28 Mesh grids of optical sensors on central column
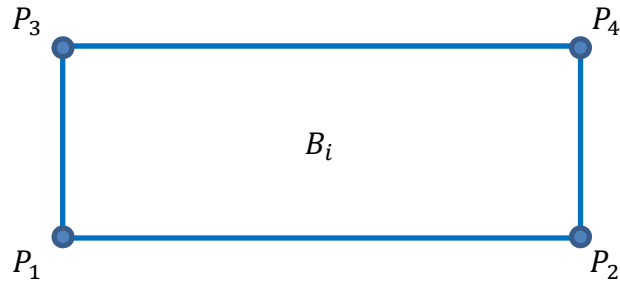
Figure 3-29 Nodal order for a particular element
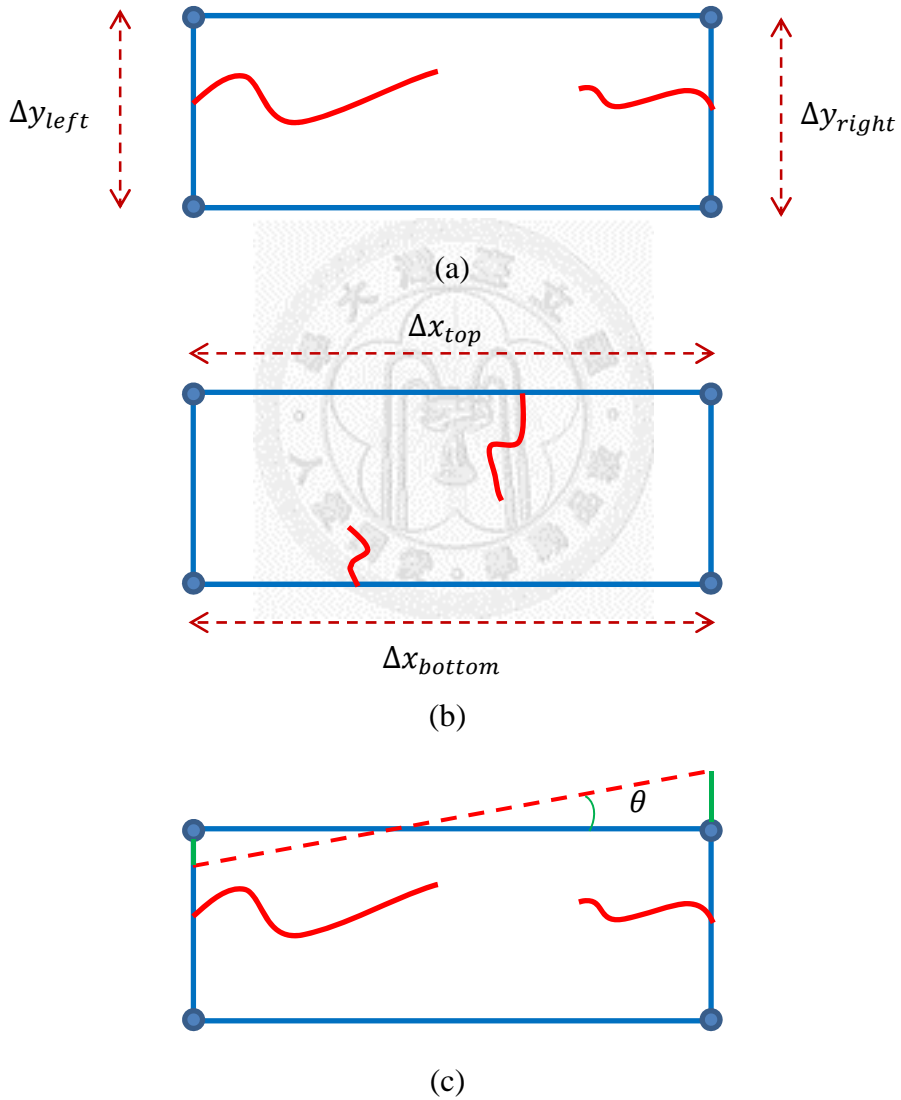
Figure 3-30 Scheme of damage detection: (a) vertical, (b) laterial difference, and (c) y

direction bending analysis
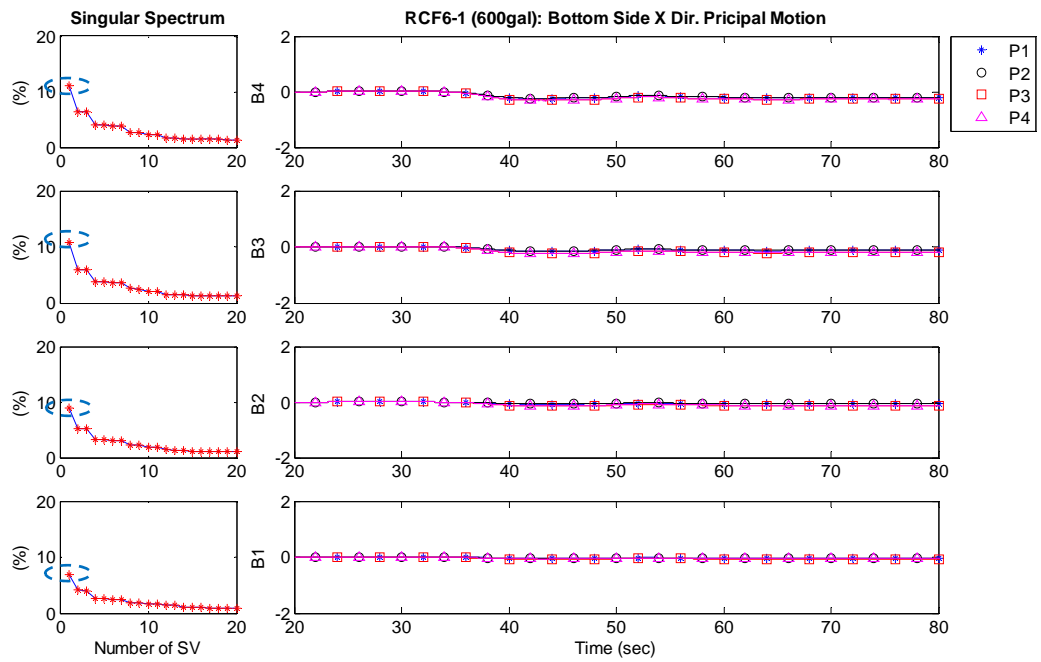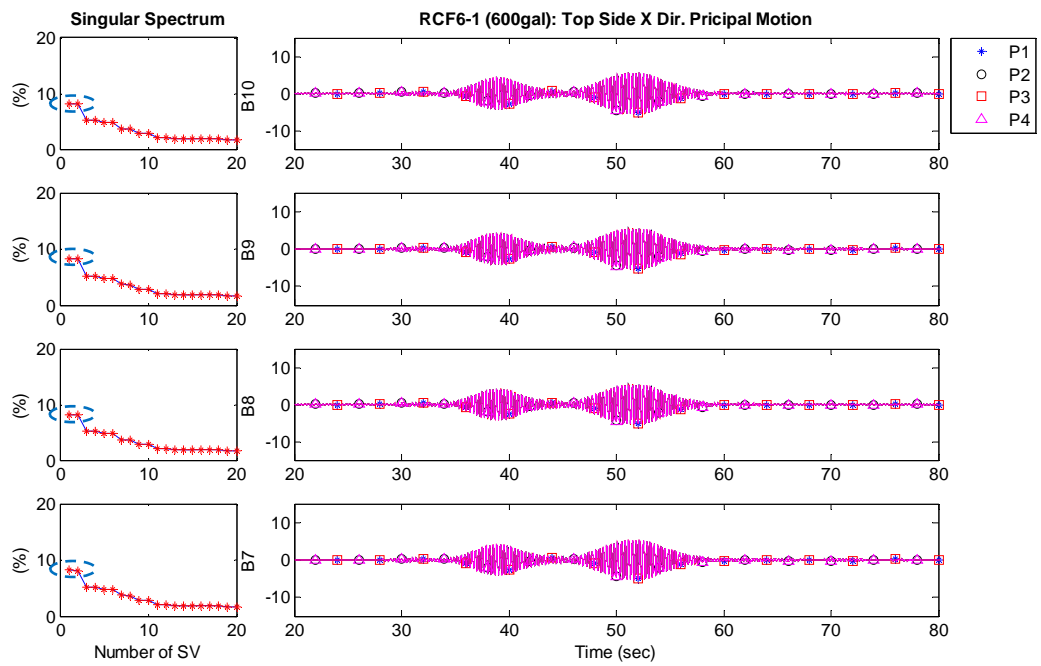
Figure 3-31 RCF6-1 X Dir. element four nodes principal motion
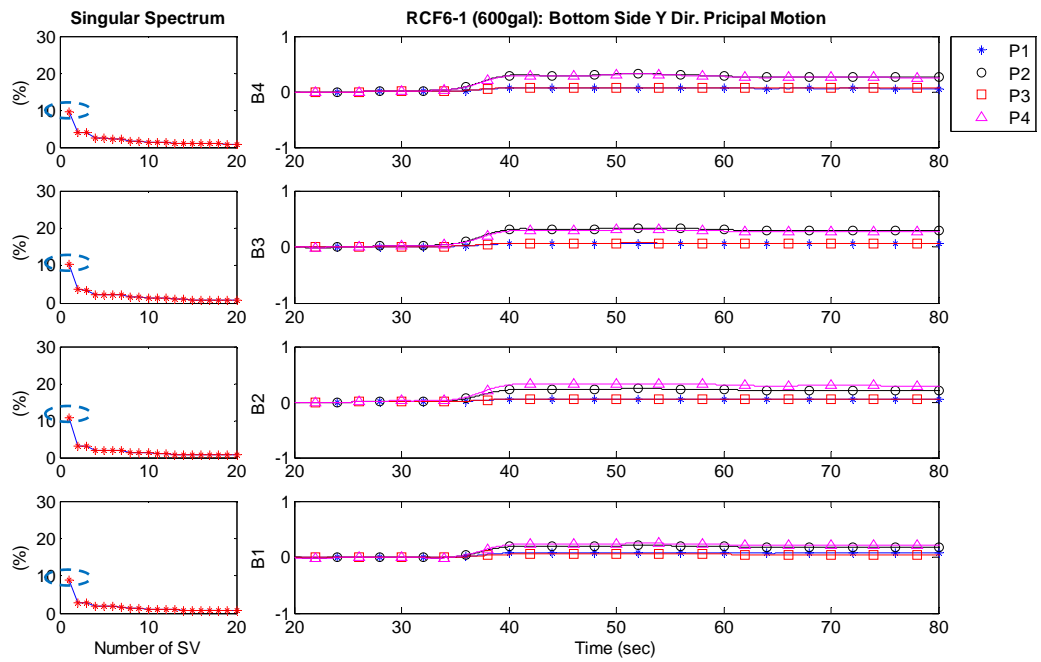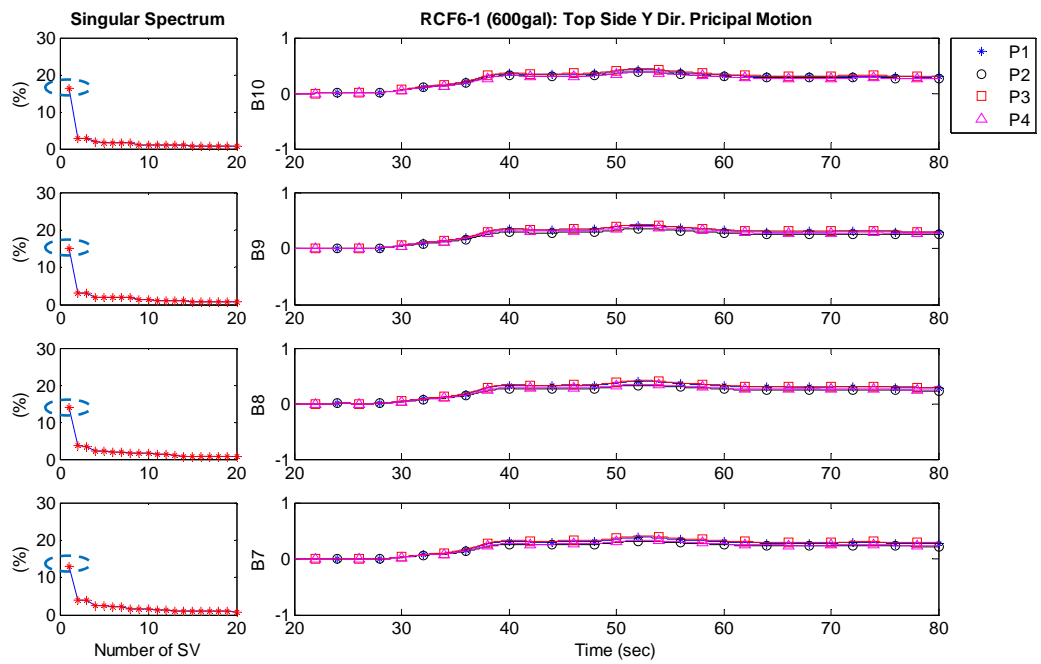
Figure 3-32 RCF6-1 Y Dir. element four nodes principal motion
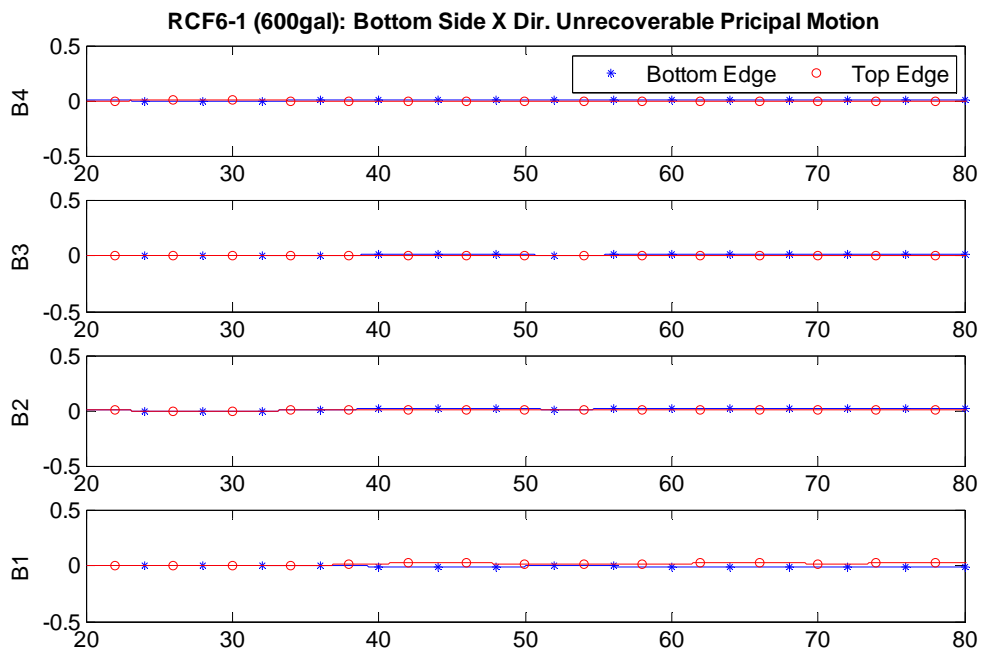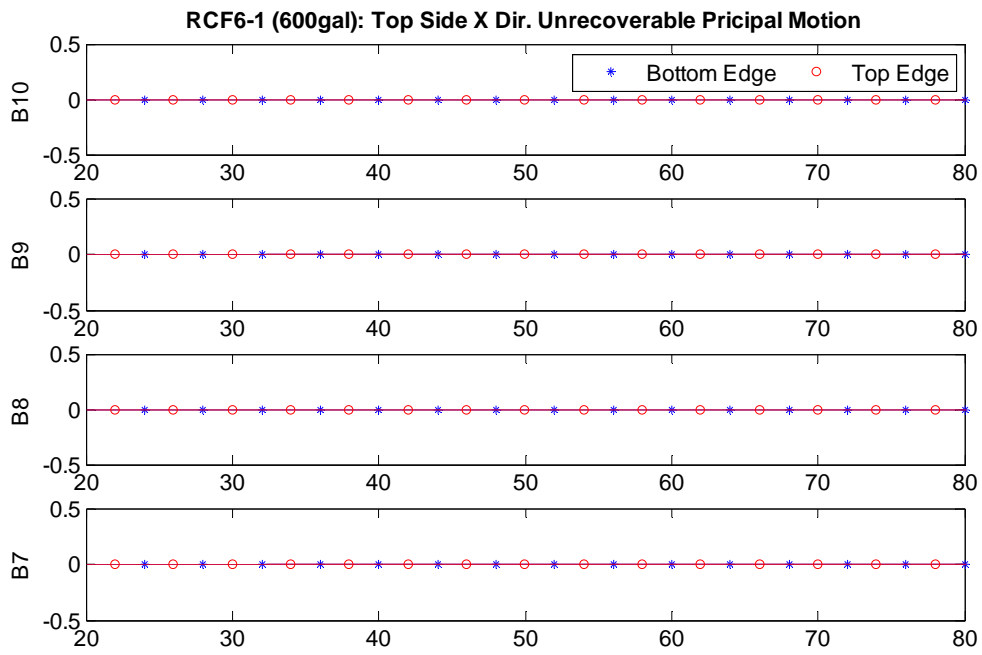
Figure 3-33 RCF6-1 X Dir. unrecoverable element principal motion

98
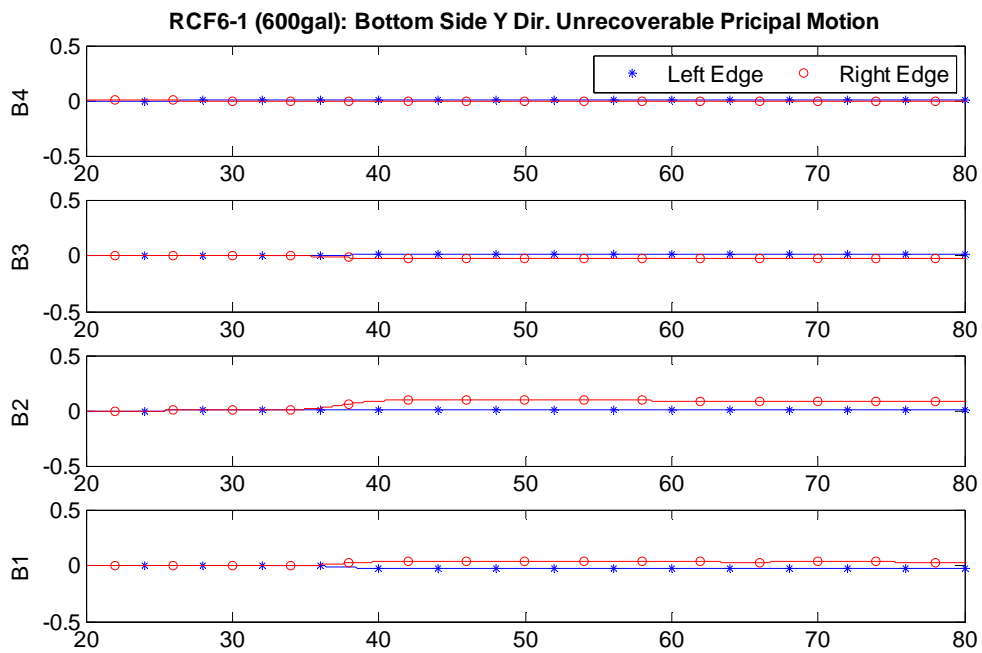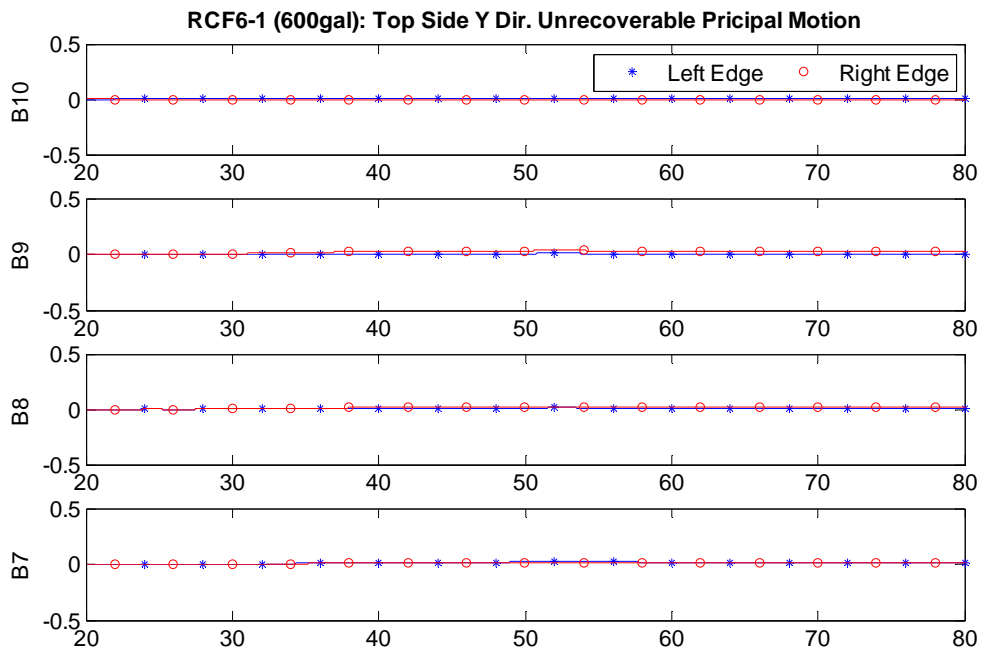
Figure 3-34 RCF6-1 Y Dir. unrecoverable element principal motion
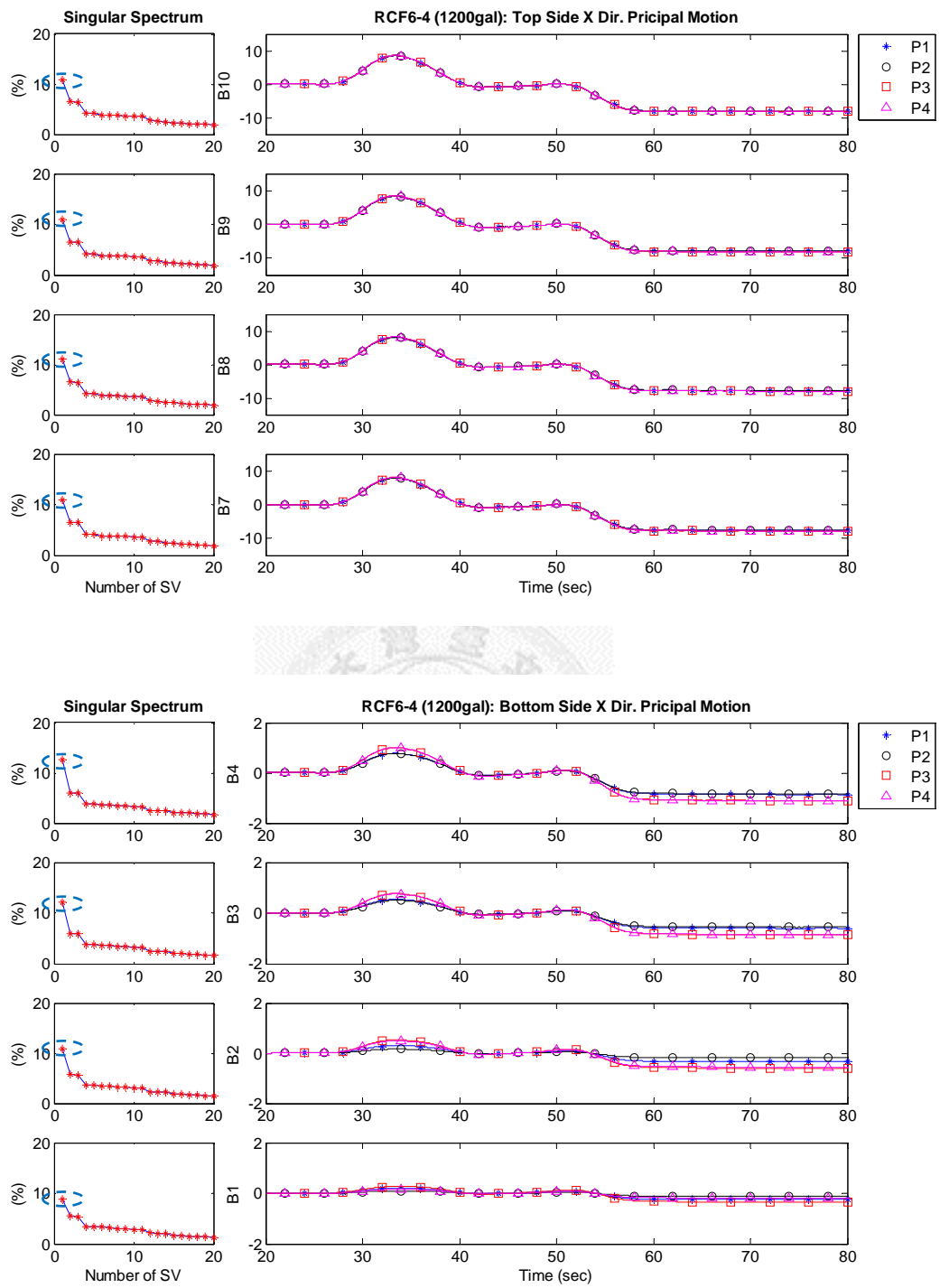
Figure 3-35 RCF6-4 X Dir. element four nodes principal motion
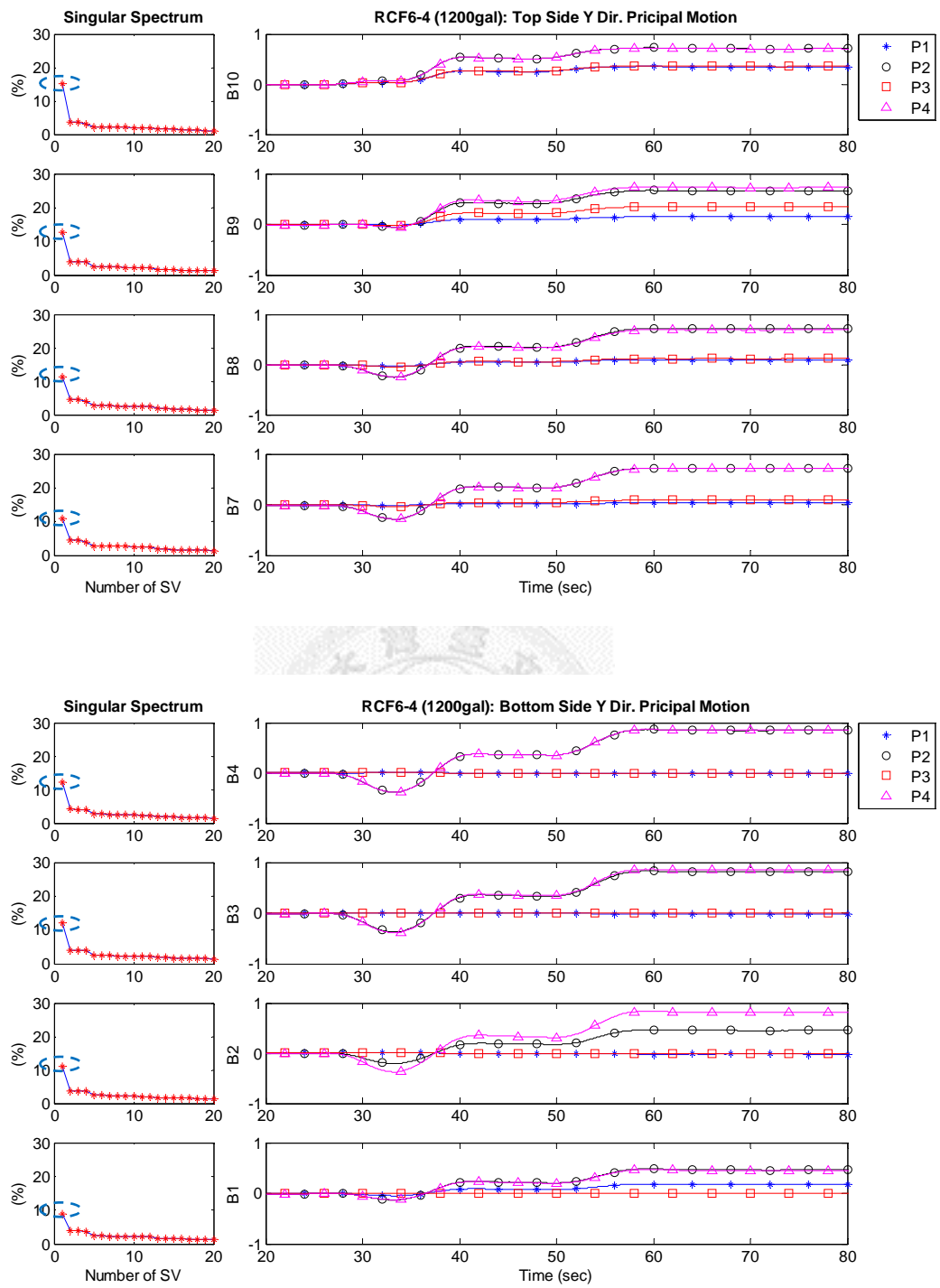
Figure 3-36 RCF6-4 Y Dir. element four nodes principal motion
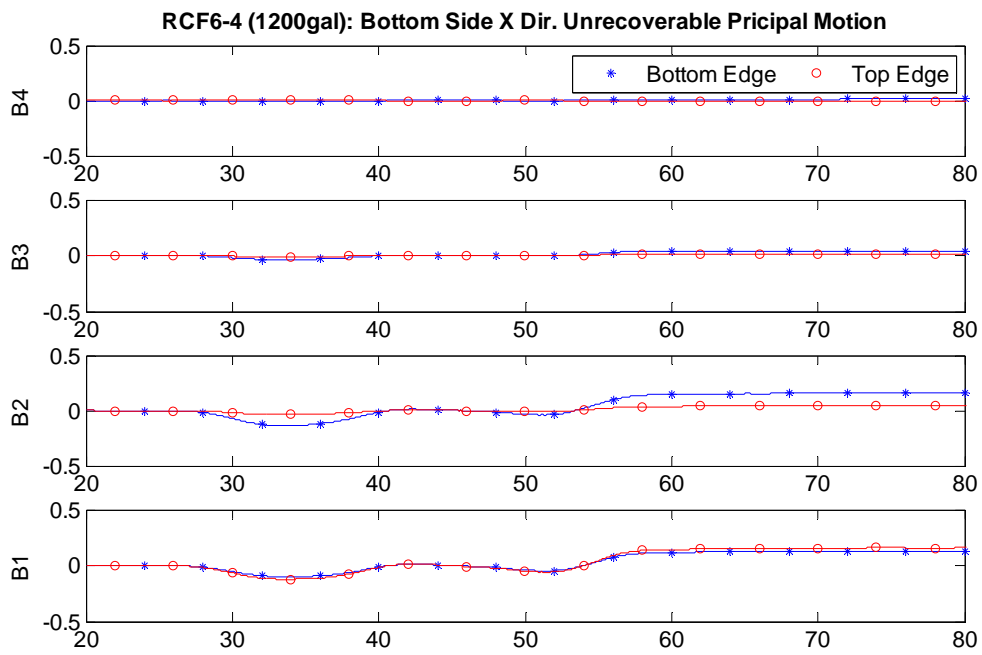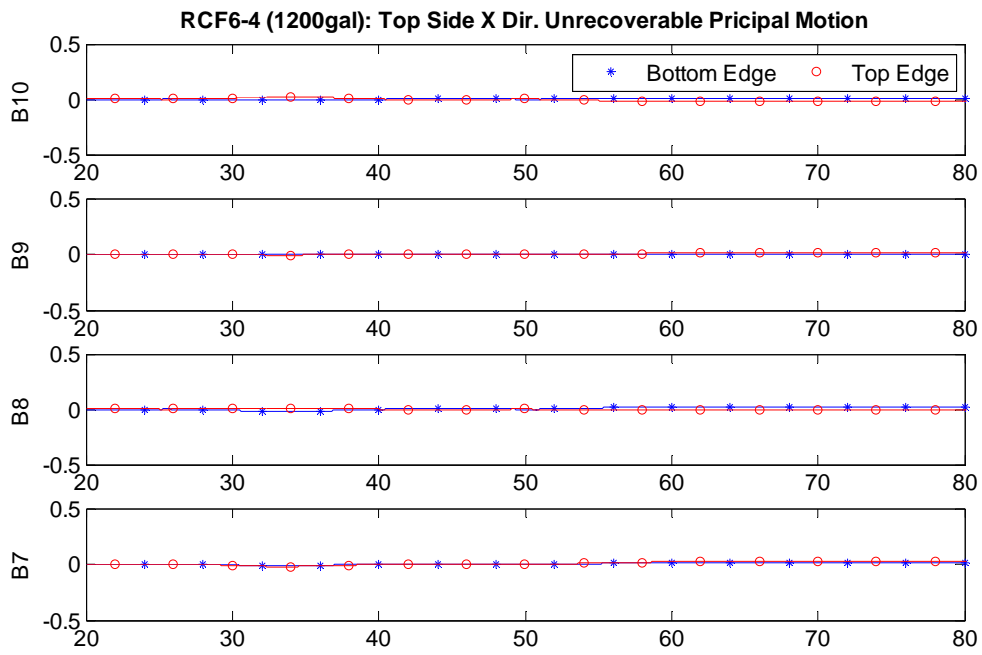
Figure 3-37 RCF6-4 X Dir. unrecoverable element principal motion

102
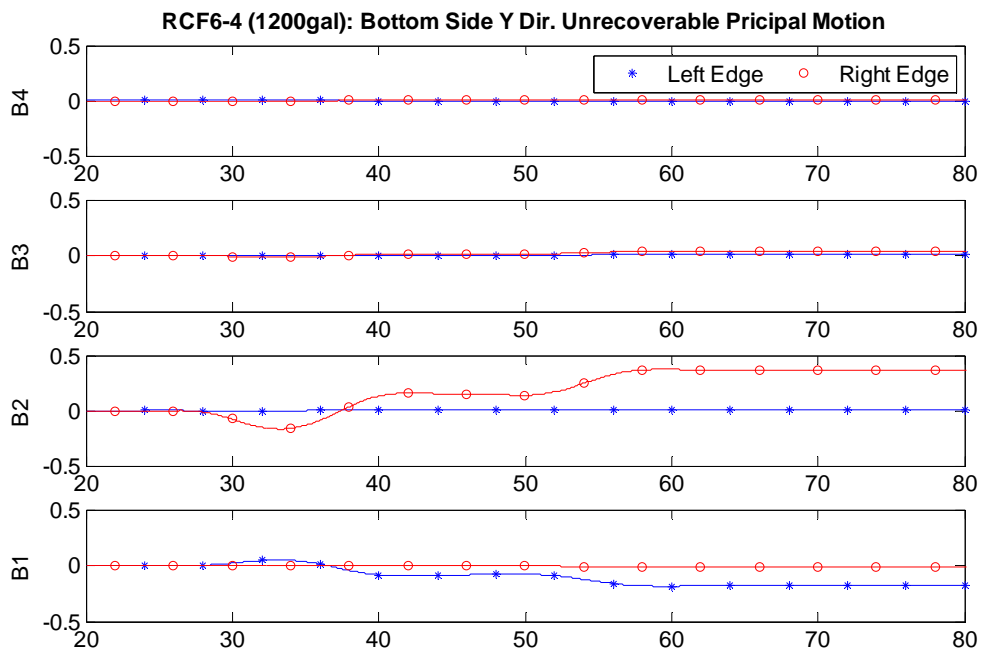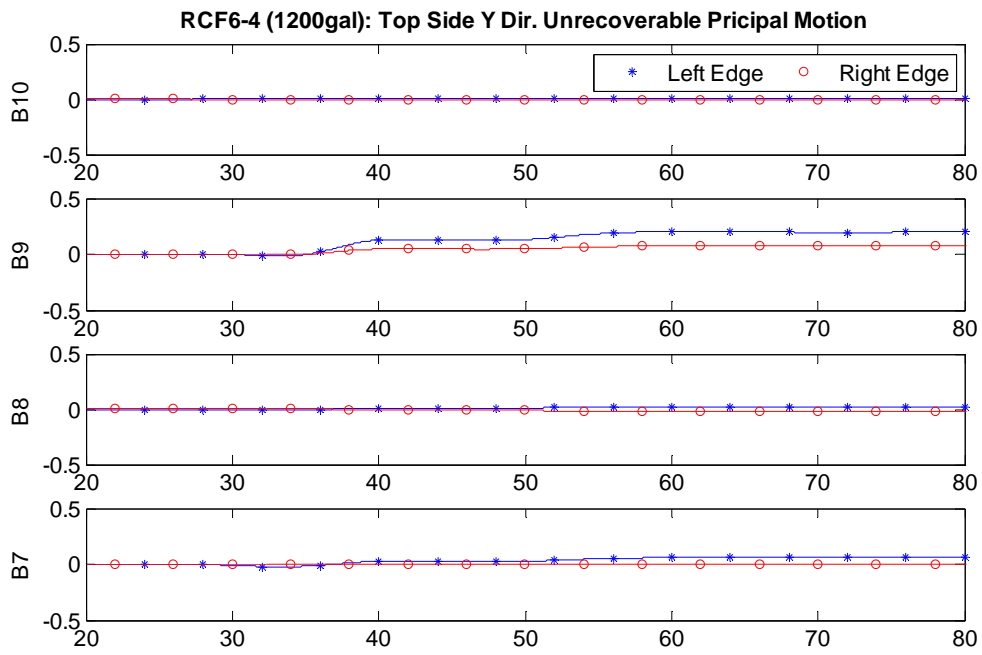
Figure 3-38 RCF6-4 Y Dir. unrecoverable element principal motion

RCF6-1 (600gal): Bottom Side X Dir. Square-sum of Unrecoverable Signals
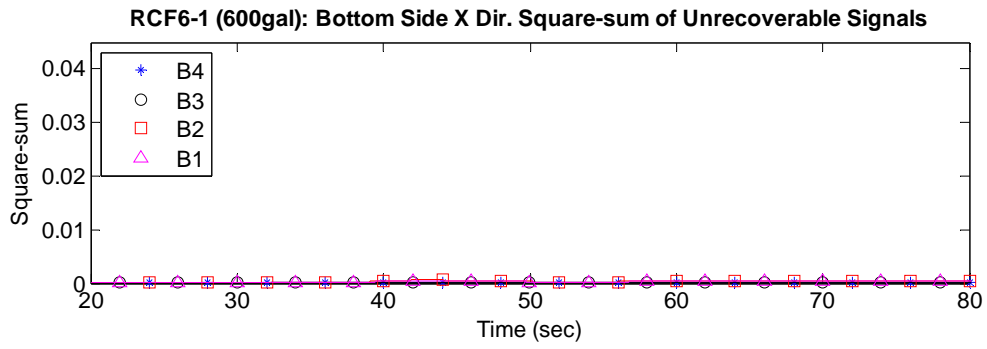
Figure 3-39 RCF6-1 X Dir. square -sum of unrecoverable signals

RCF6-1 (600gal): Top Side Y Dir. Square-sum of Unrecoverable Signals

RCF6-1 (600gal): Bottom Side Y Dir. Square-sum of Unrecoverable Signals
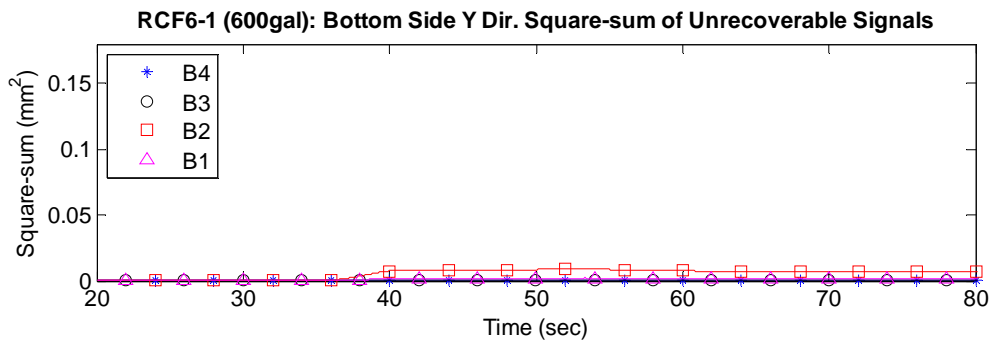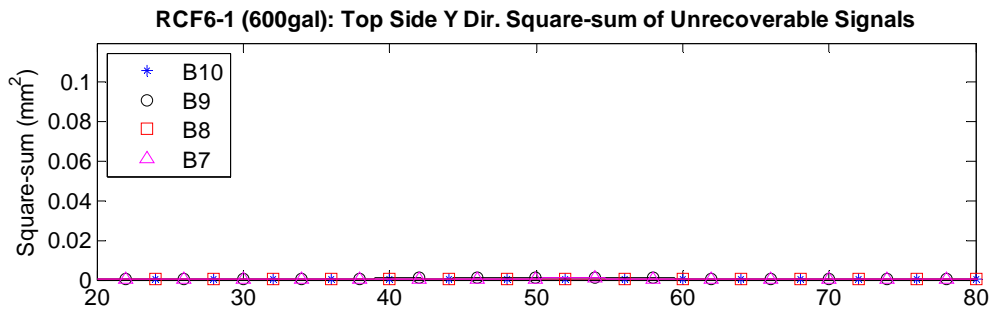
Figure 3-40 RCF6-1 Y Dir. square-sum of unrecoverable signals
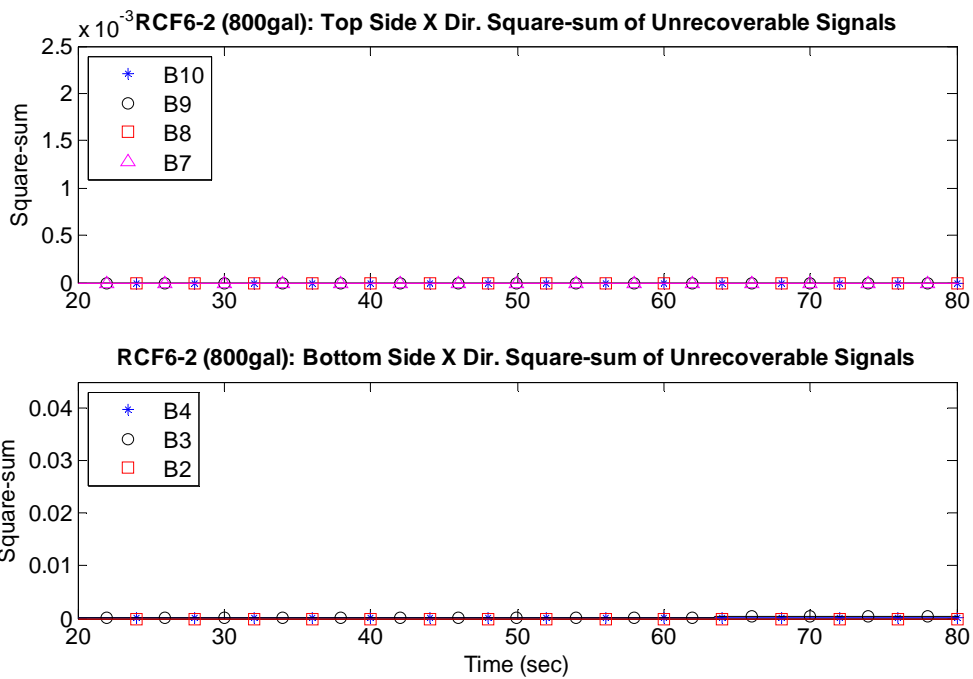
Figure 3-41 RCF6-2 X Dir. square-sum of unrecoverable signals
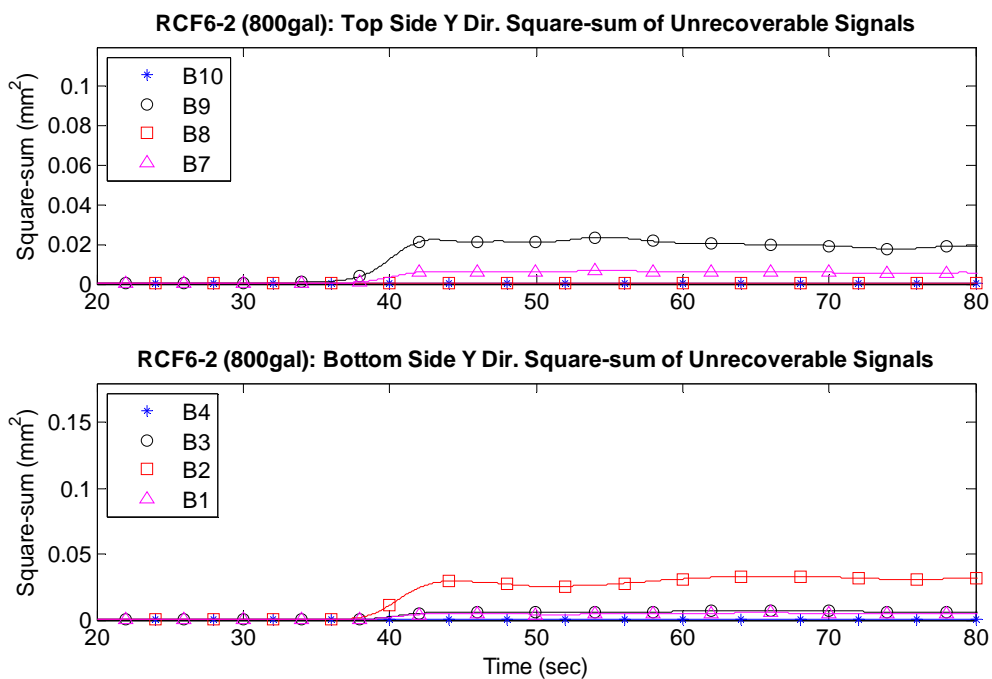
Figure 3-42 RCF6-2 Y Dir. square-sum of unrecoverable signals

105
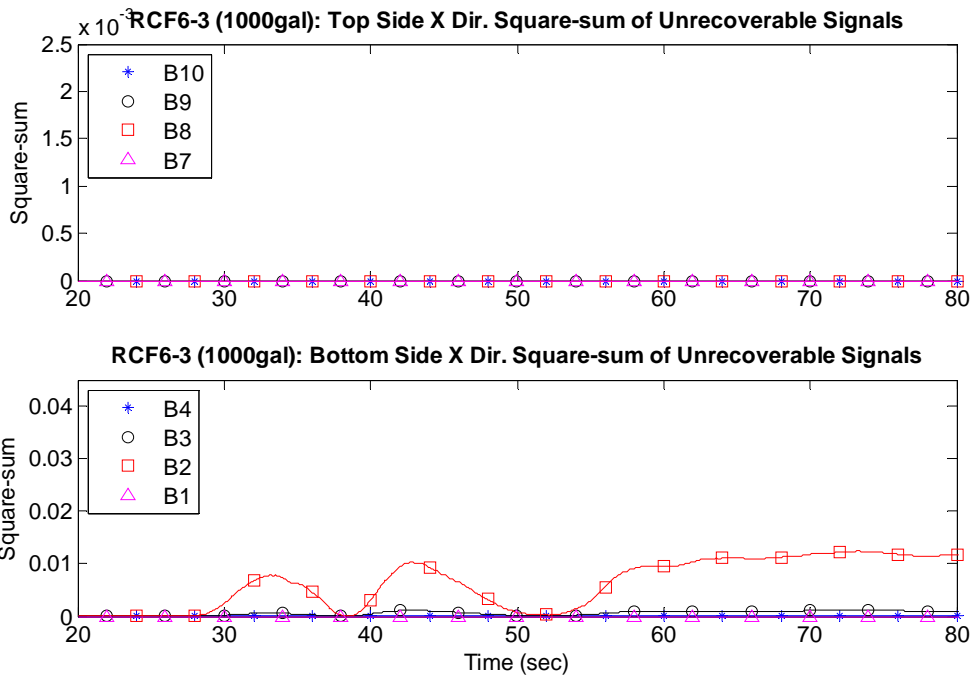
Figure 3-43 RCF6-3 X Dir. square-sum of unrecoverable signals
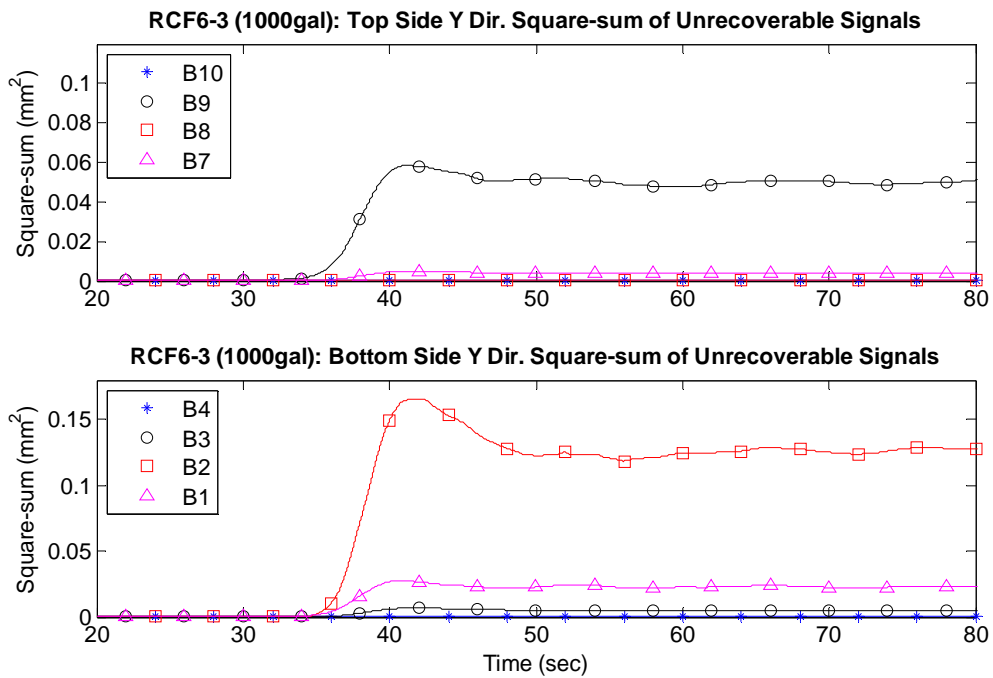
Figure 3-44 RCF6-3 Y Dir. square-sum of unrecoverable signals
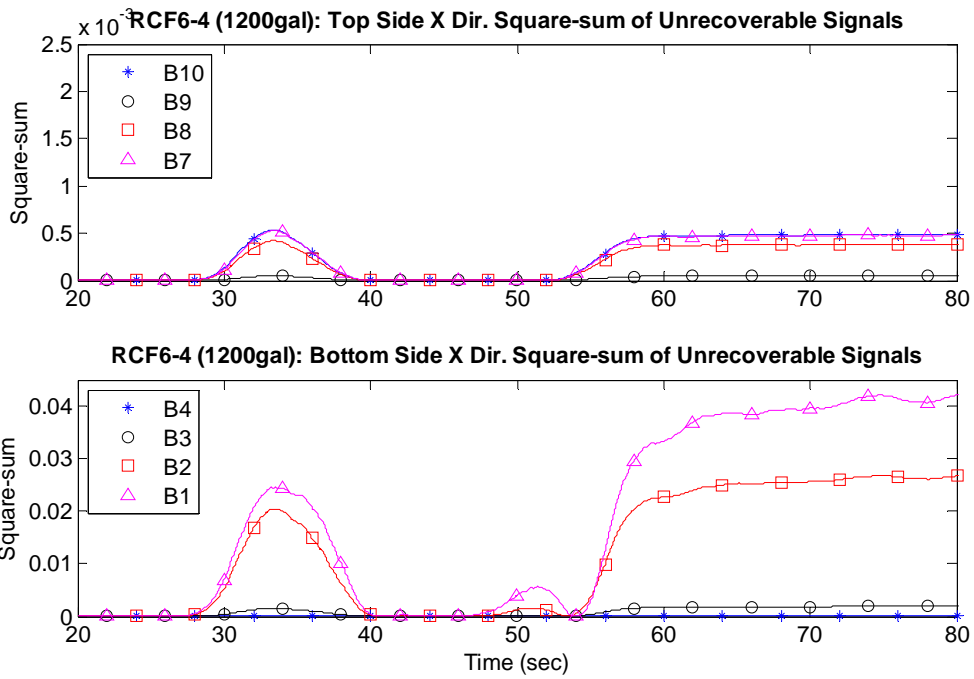
Figure 3-45 RCF6-4 X Dir. square-sum of unrecoverable signals
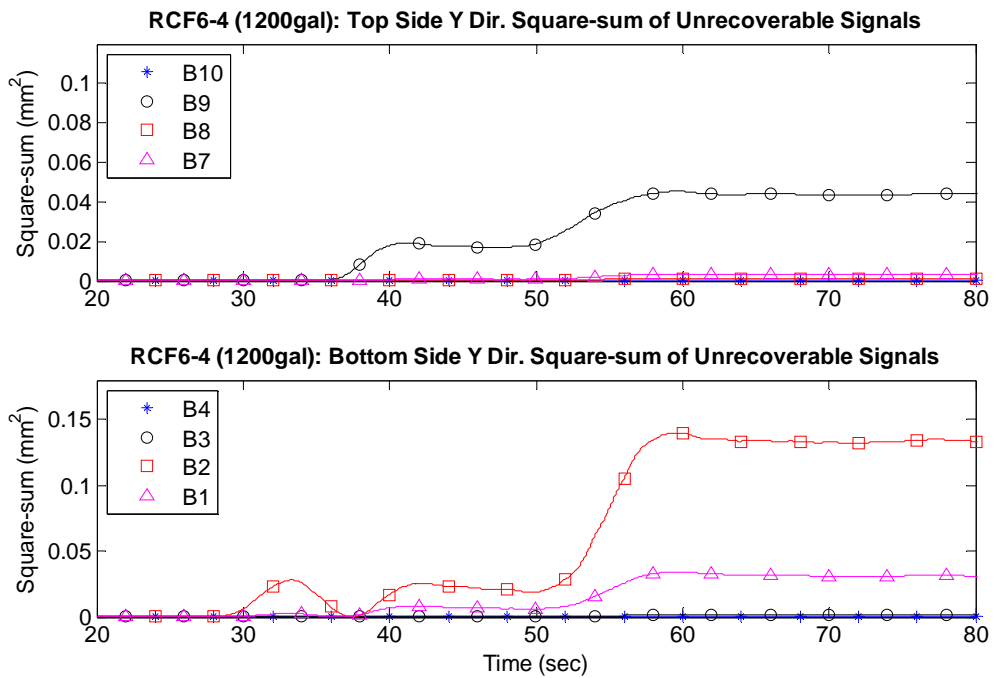
Figure 3-46 RCF6-4 Y Dir. square-sum of unrecoverable signals
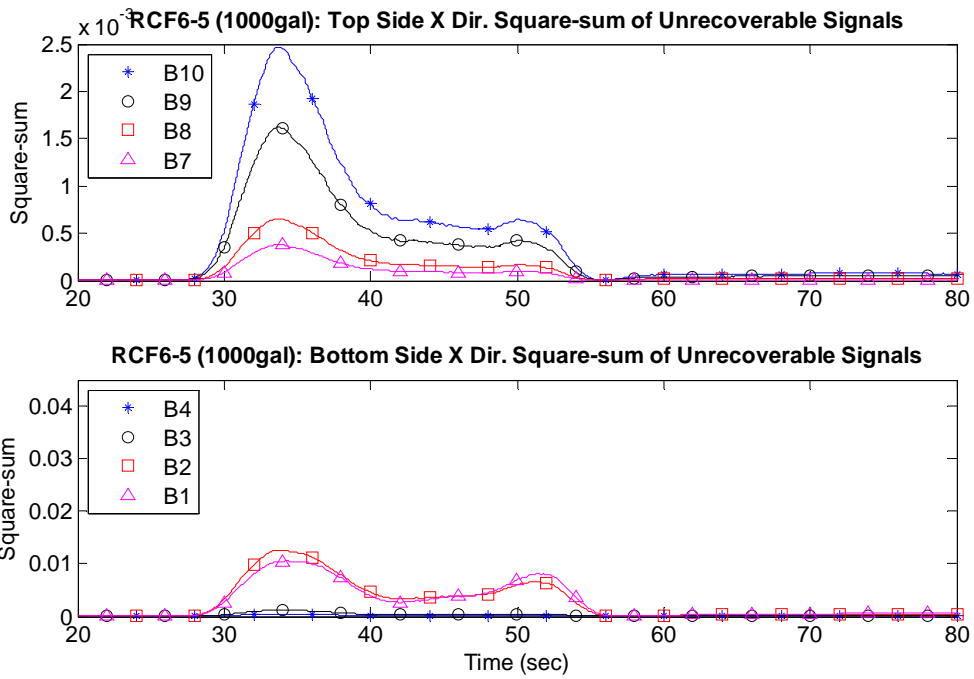
Figure 3-47 RCF6-5 X Dir. square-sum of unrecoverable signals
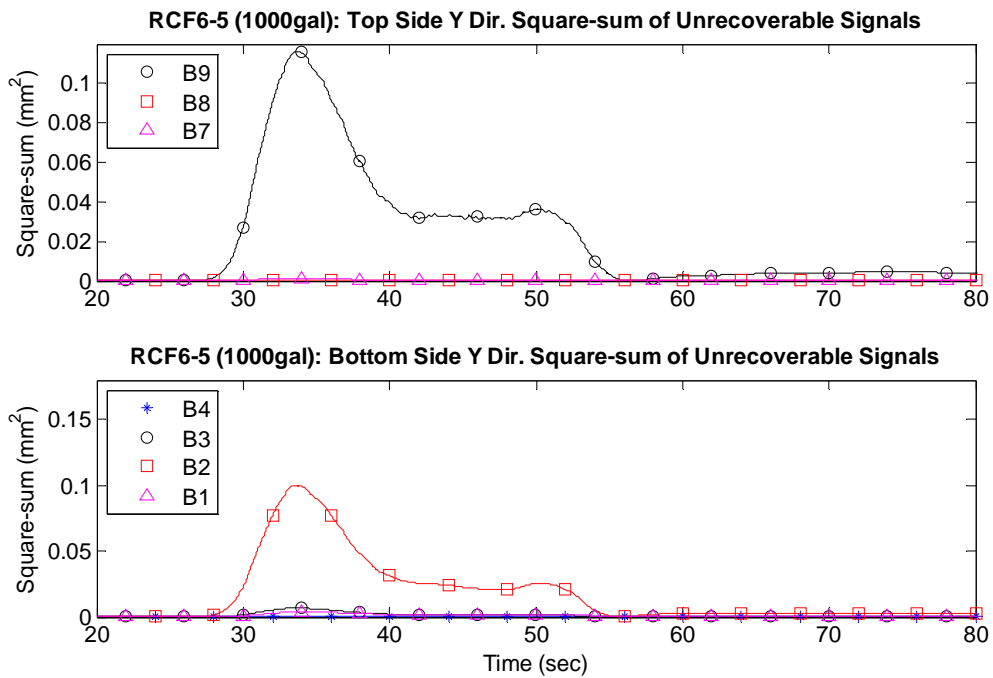
Figure 3-48 RCF6-5 Y Dir. square-sum of unrecoverable signals
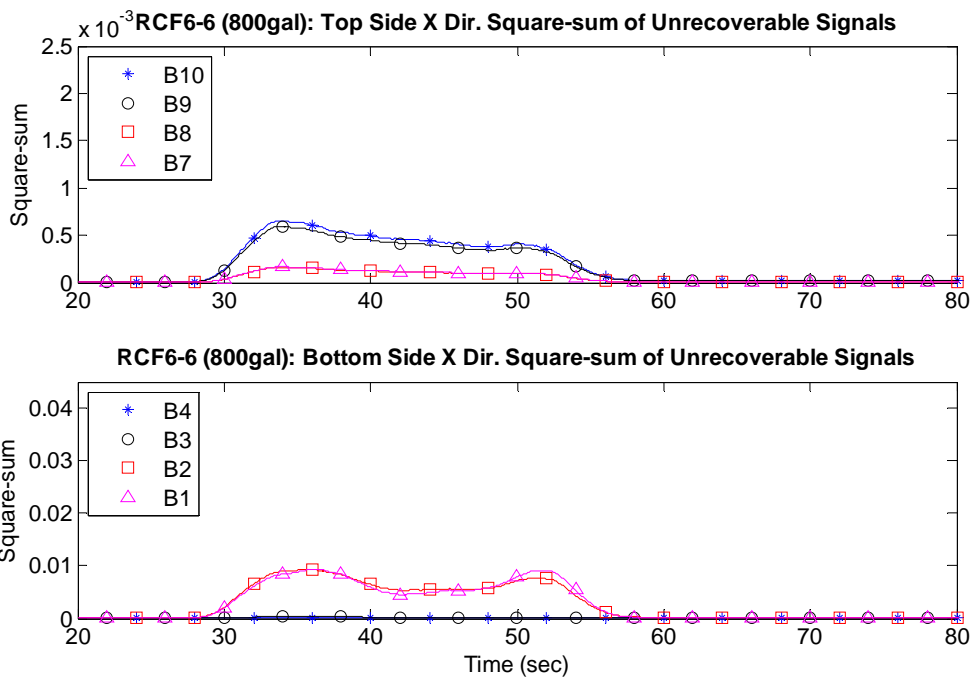
Figure 3-49 RCF6-6 X Dir. square-sum of unrecoverable signals
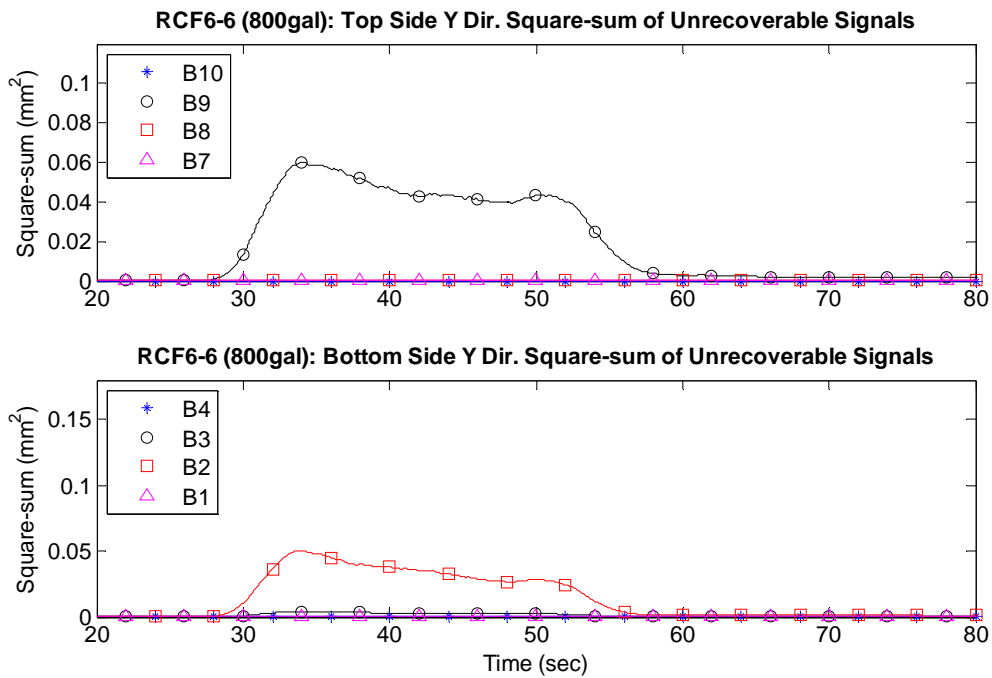
Figure 3-50 RCF6-6 Y Dir. square-sum of unrecoverable signals
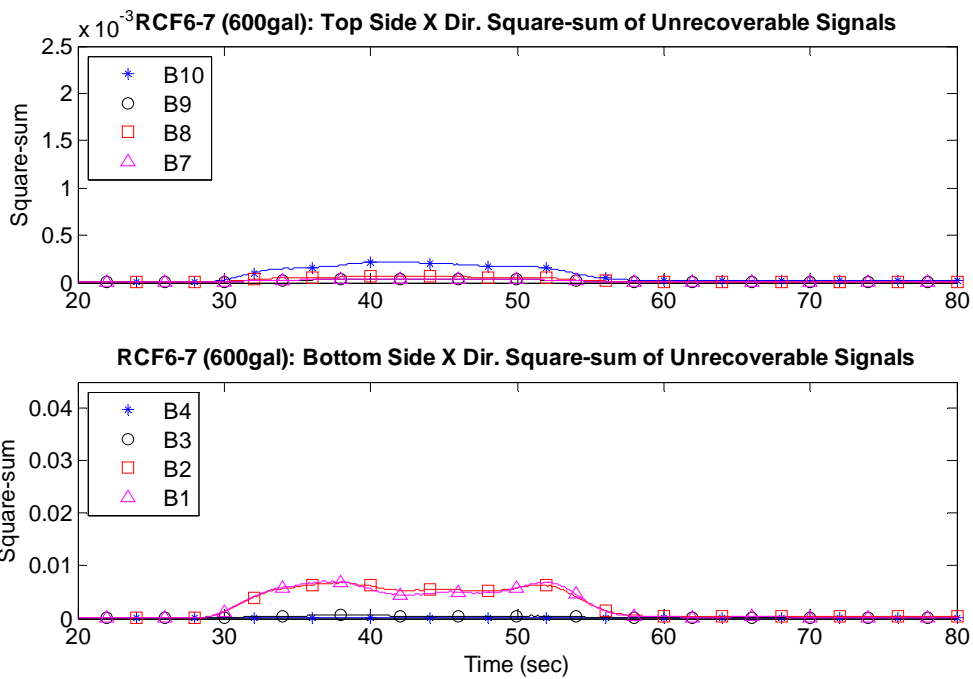
Figure 3-51 RCF6-7 X Dir. square-sum of unrecoverable signals
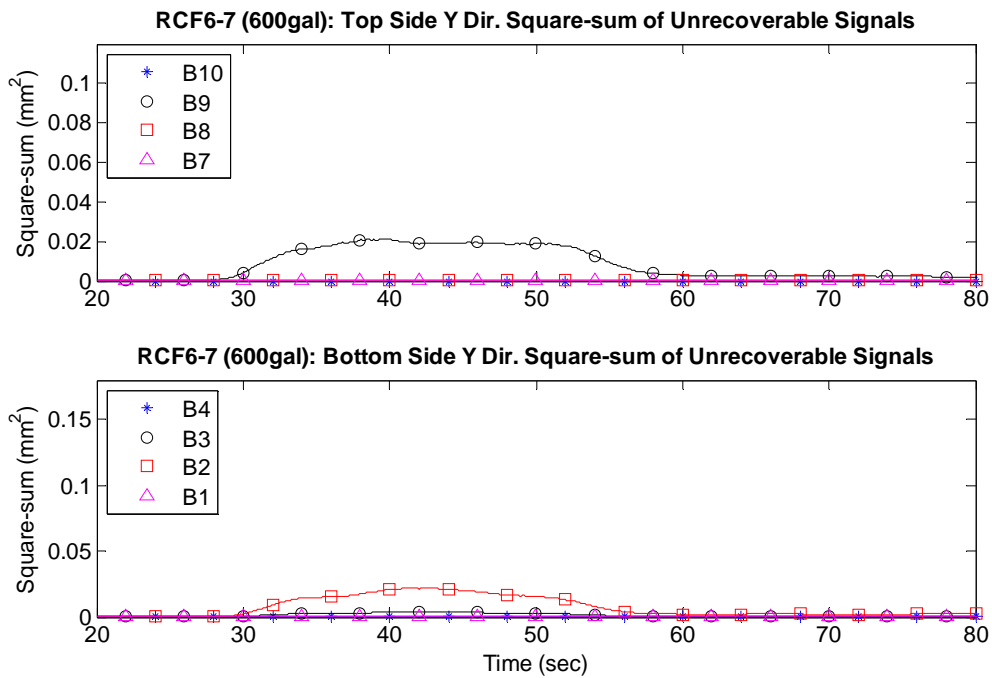
Figure 3-52 RCF6-7 Y Dir. square-sum of unrecoverable signals
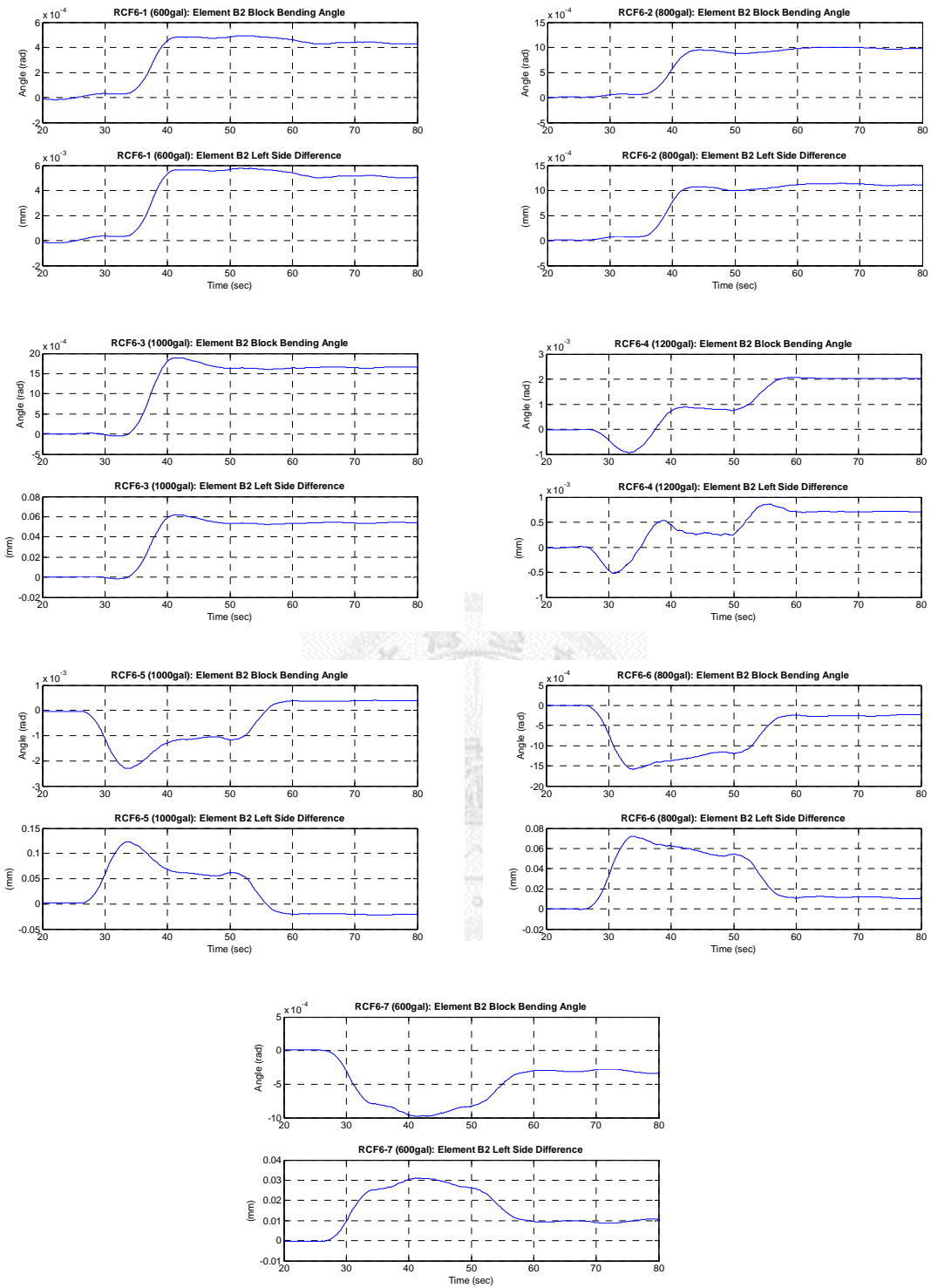
Figure 3-53 Element B2 Y Direction bending angle analysis
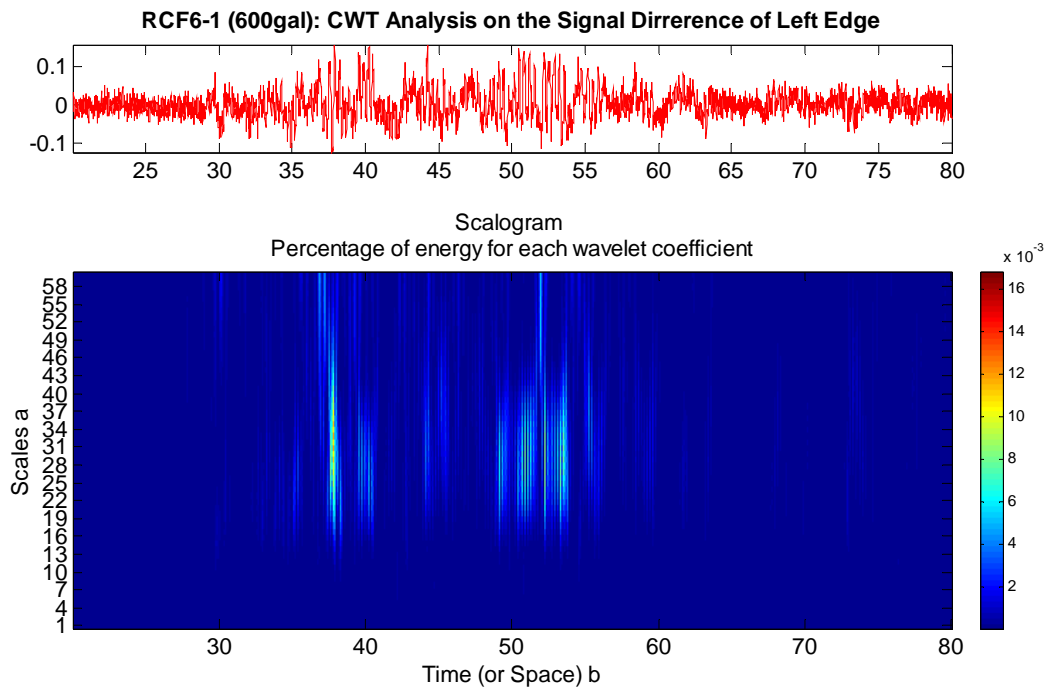
Figure 3-54 RCF6-1 CWT analysis of element B2 lef edge difference
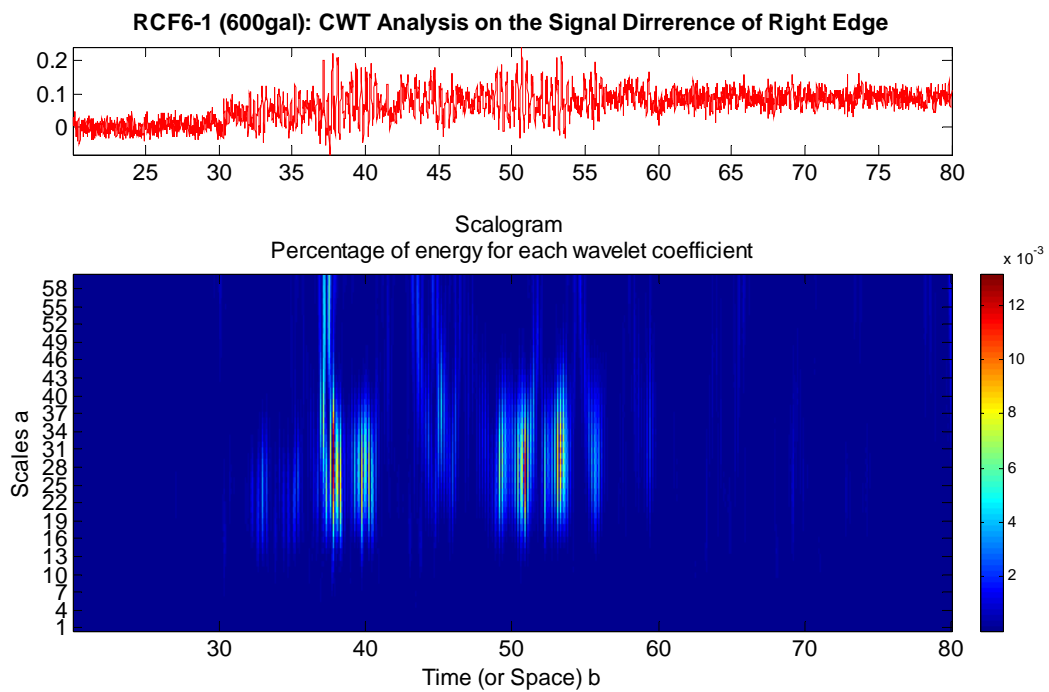
Figure 3-55 RCF6-1 CWT analysis of element B2 right edge difference
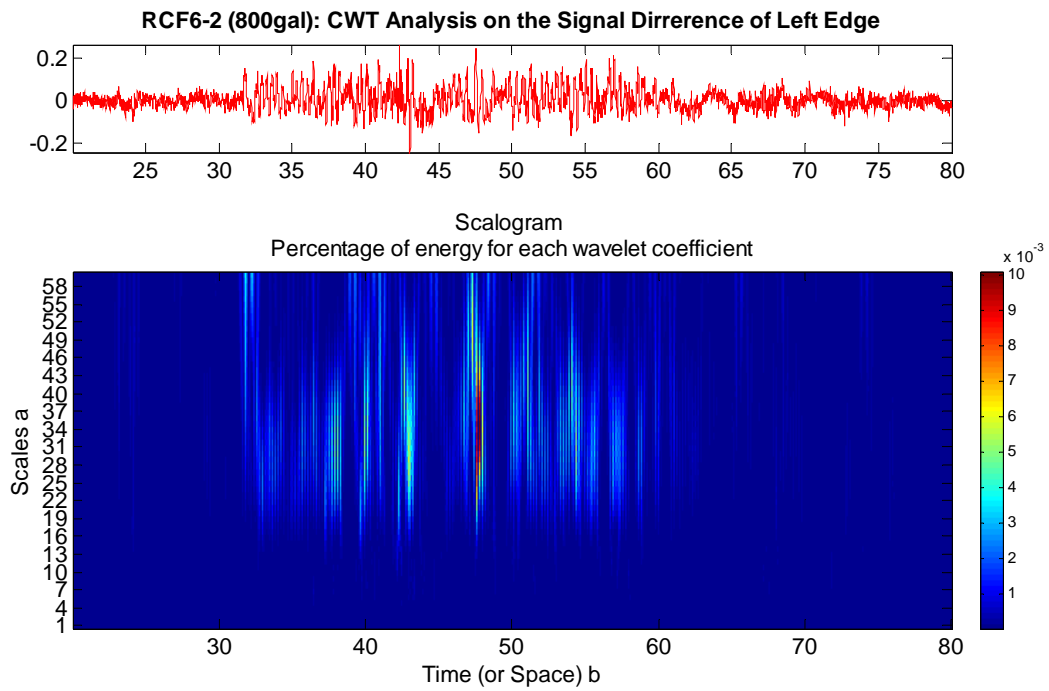
Figure 3-56 RCF6-2 CWT analysis of element B2 lef edge difference
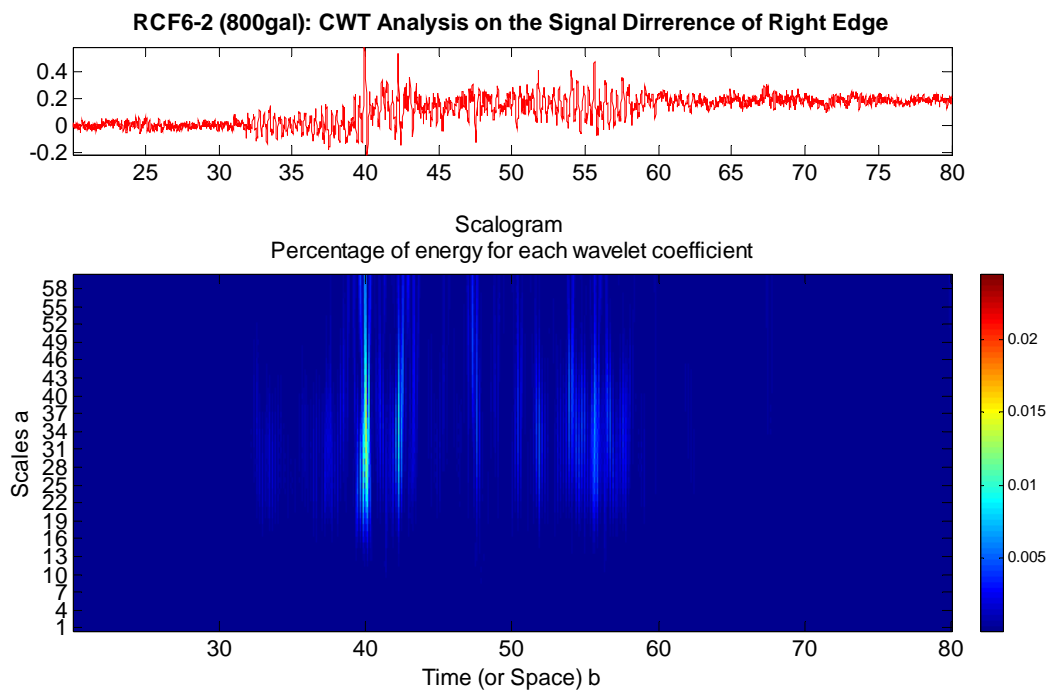
Figure 3-57 RCF6-2 CWT analysis of element B2 right edge difference
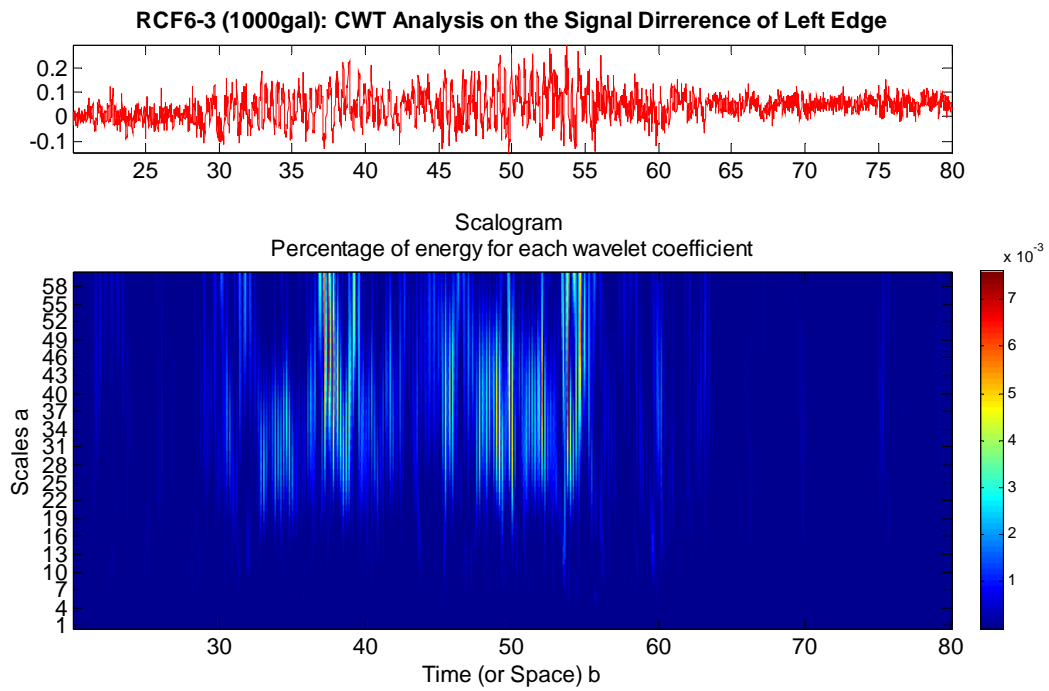
Figure 3-58 RCF6-3 CWT analysis of element B2 lef edge difference
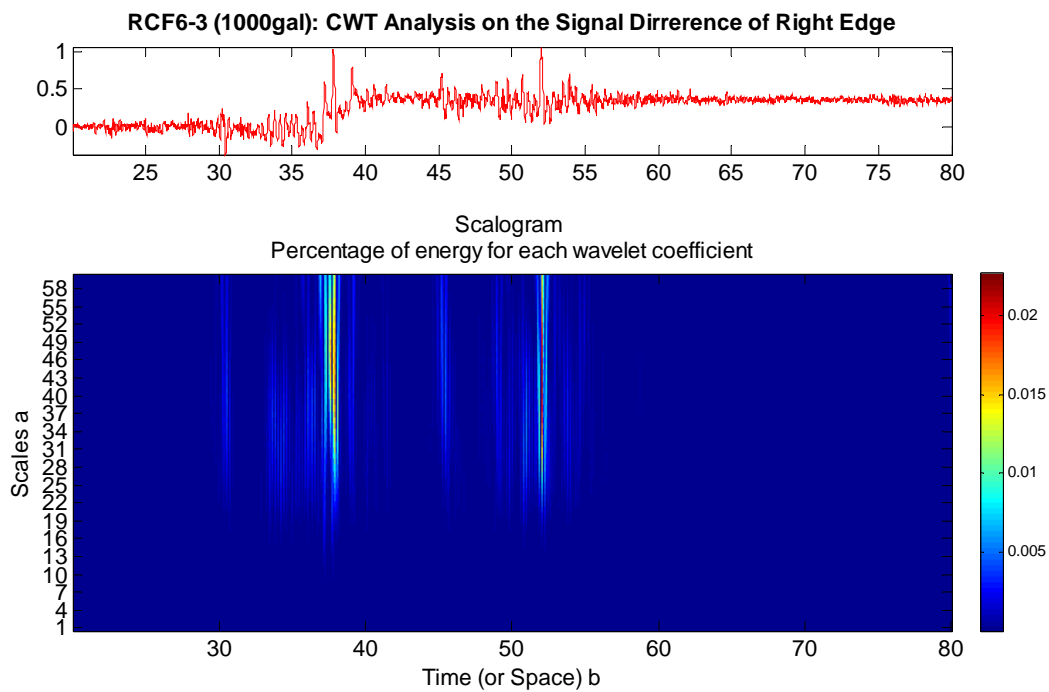
Figure 3-59 RCF6-3 CWT analysis of element B2 right edge difference

114
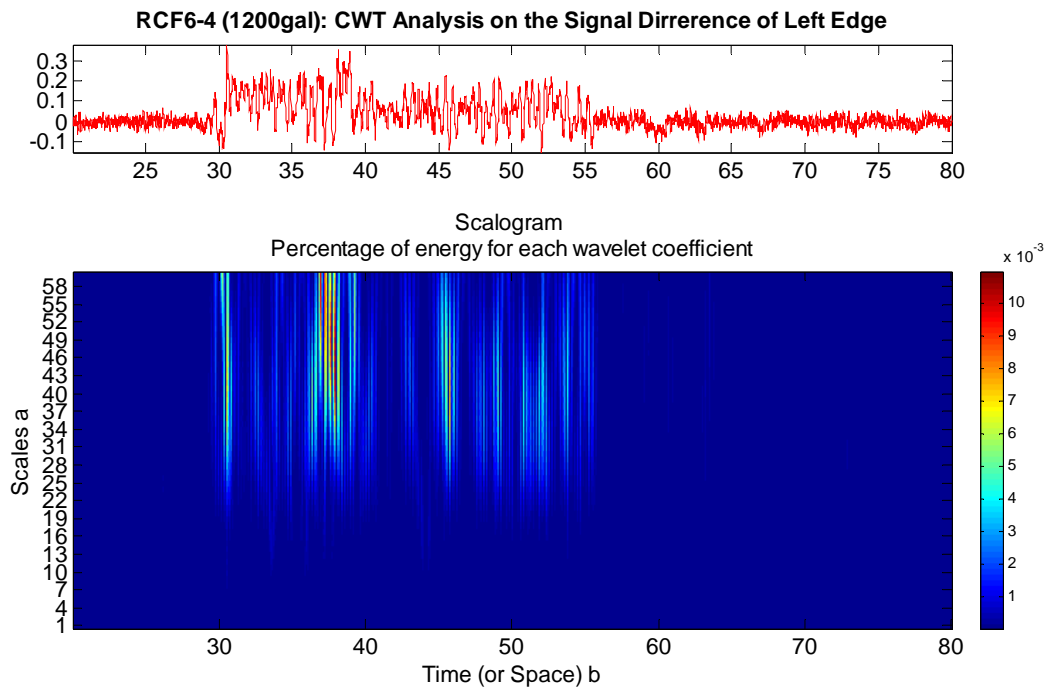
Figure 3-60 RCF6-4 CWT analysis of element B2 lef edge difference
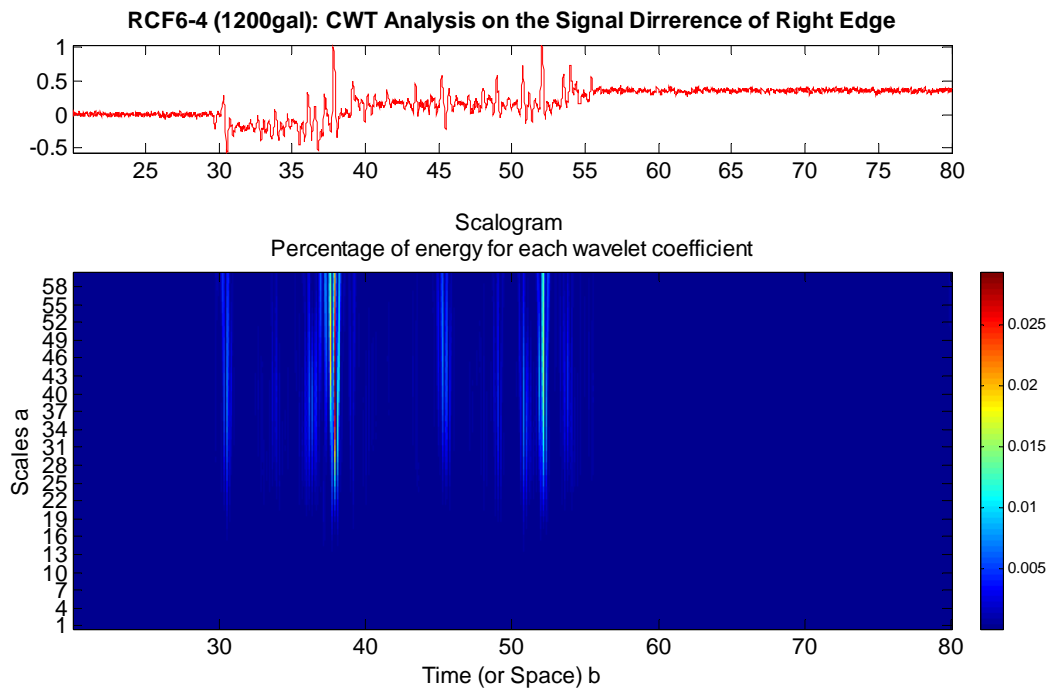
Figure 3-61 RCF6-4 CWT analysis of element B2 right edge difference

115
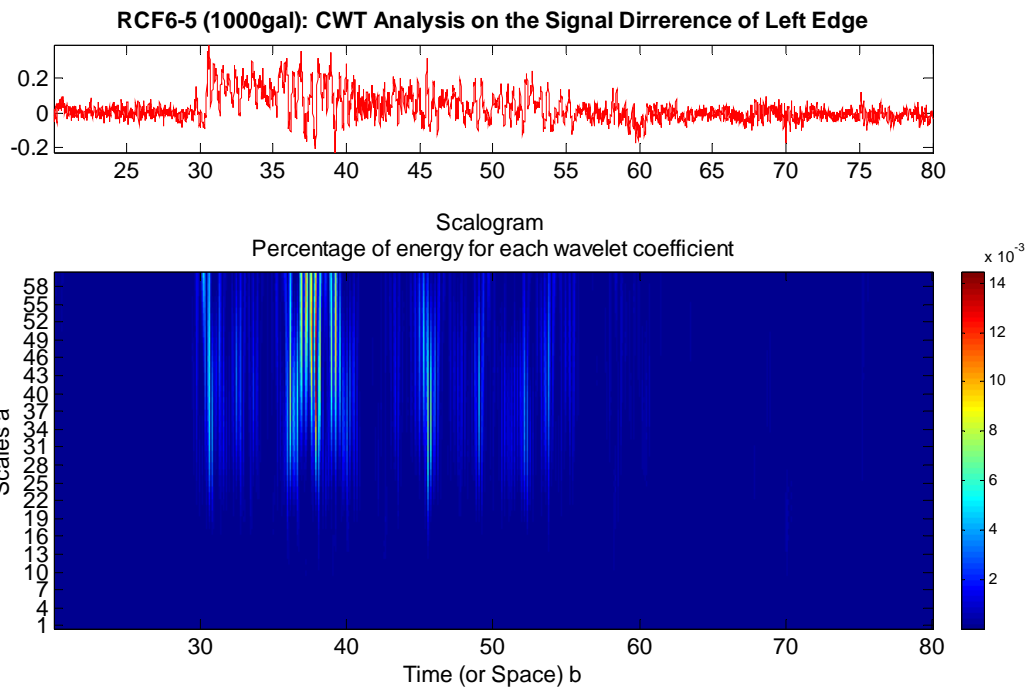
Figure 3-62 RCF6-5 CWT analysis of element B2 lef edge difference
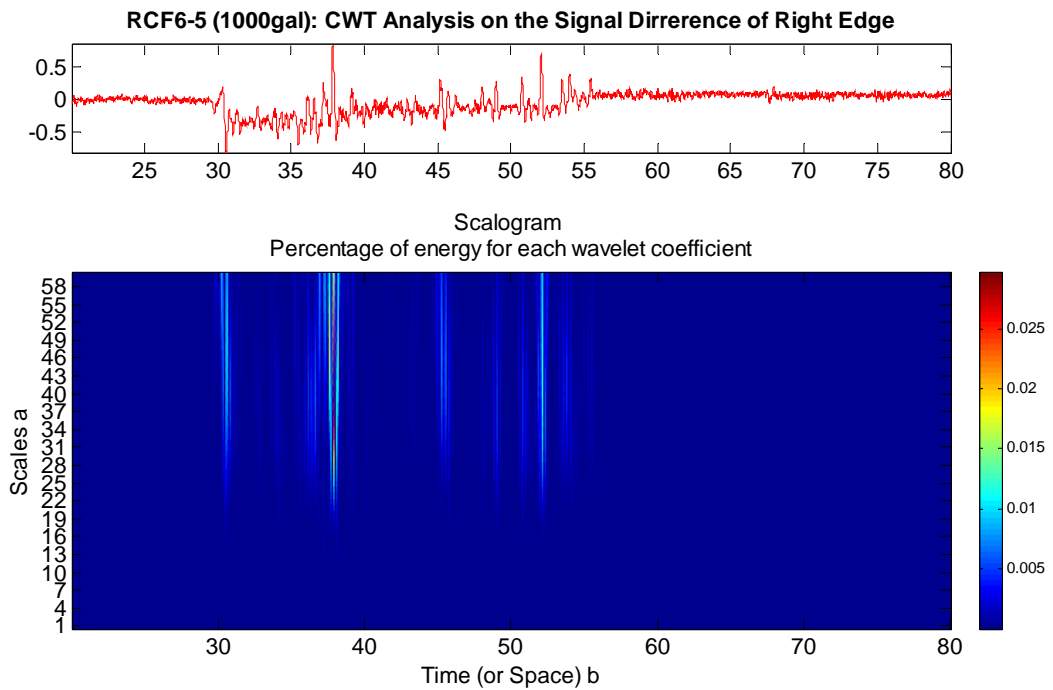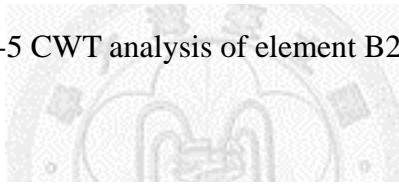
Figure 3-63 RCF6-5 CWT analysis of element B2 right edge difference
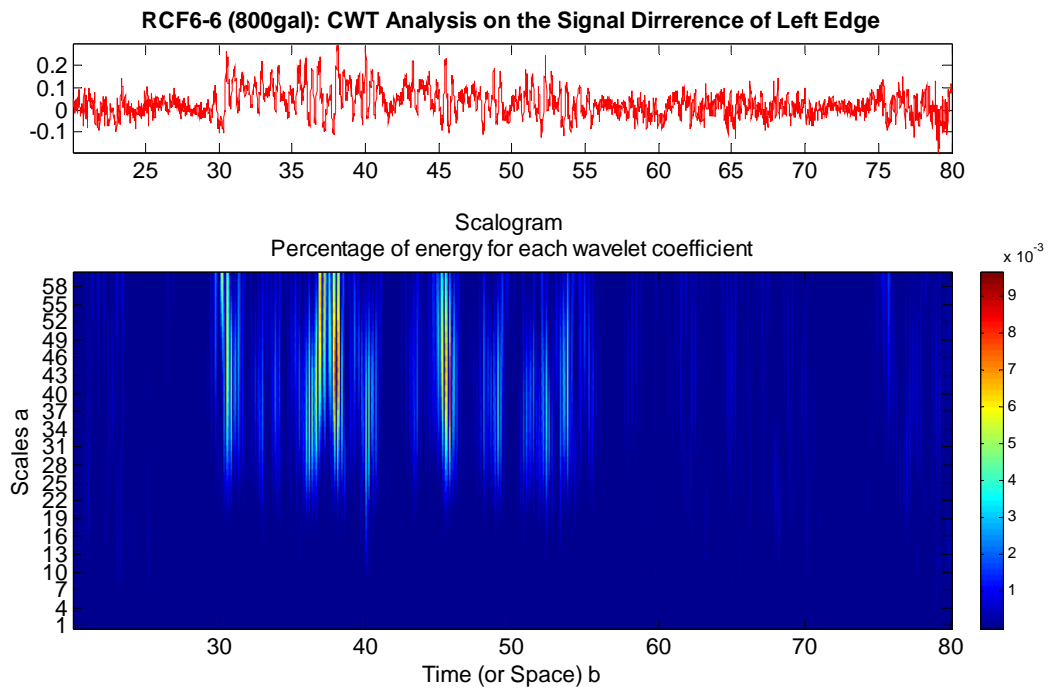
Figure 3-64 RCF6-6 CWT analysis of element B2 lef edge difference
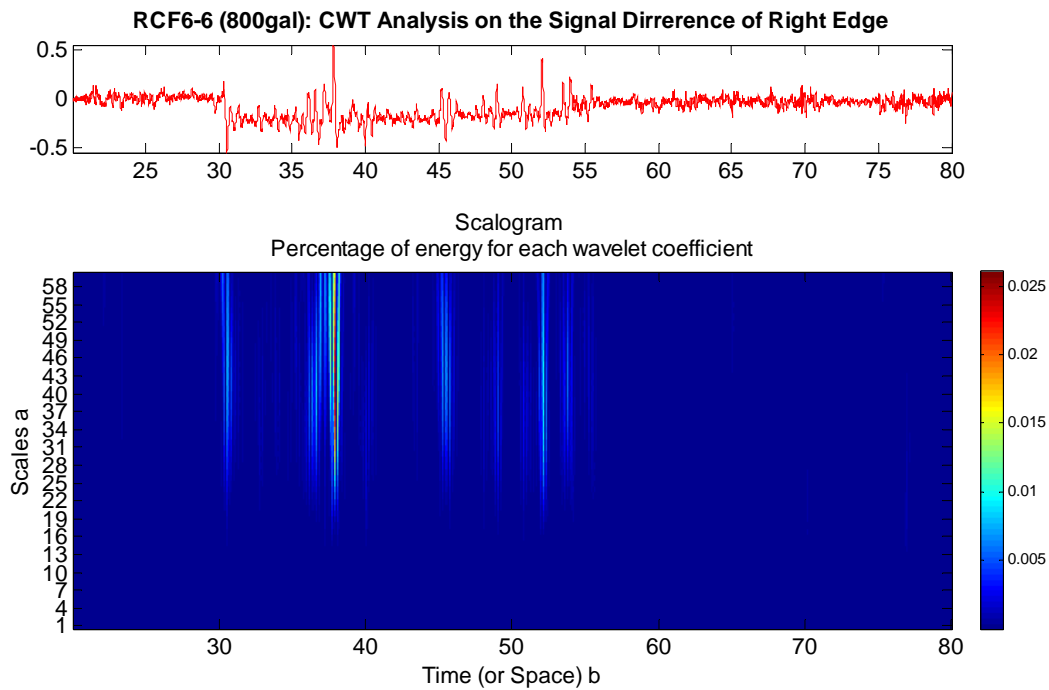
Figure 3-65 RCF6-6 CWT analysis of element B2 right edge difference
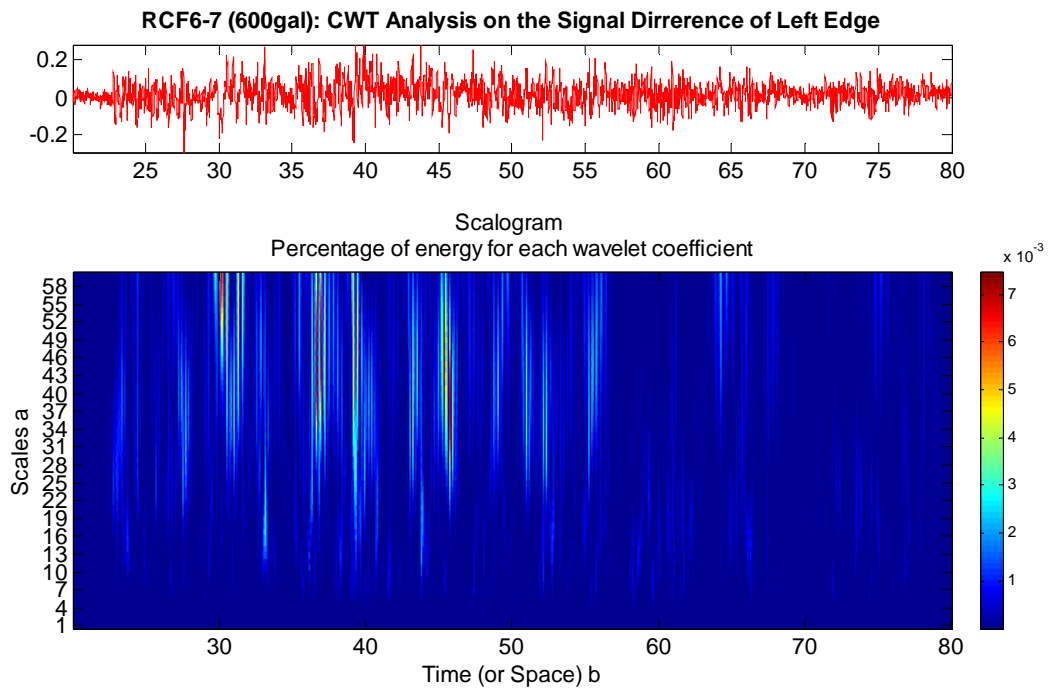
Figure 3-66 RCF6-7 CWT analysis of element B2 lef edge difference
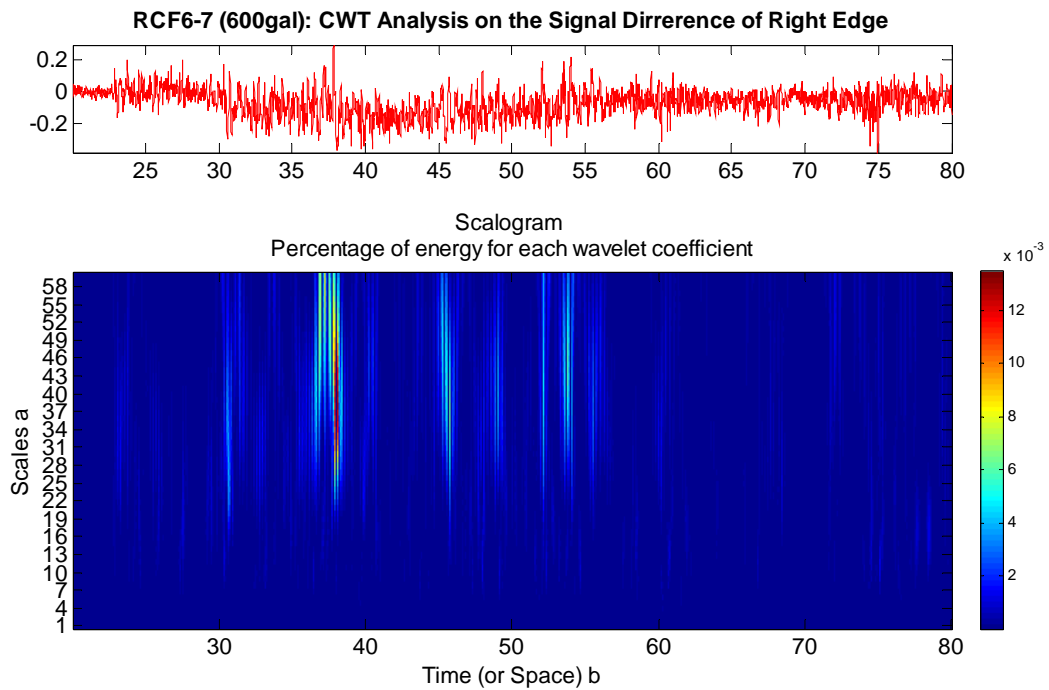
Figure 3-67 RCF6-7 CWT analysis of element B2 right edge difference

118
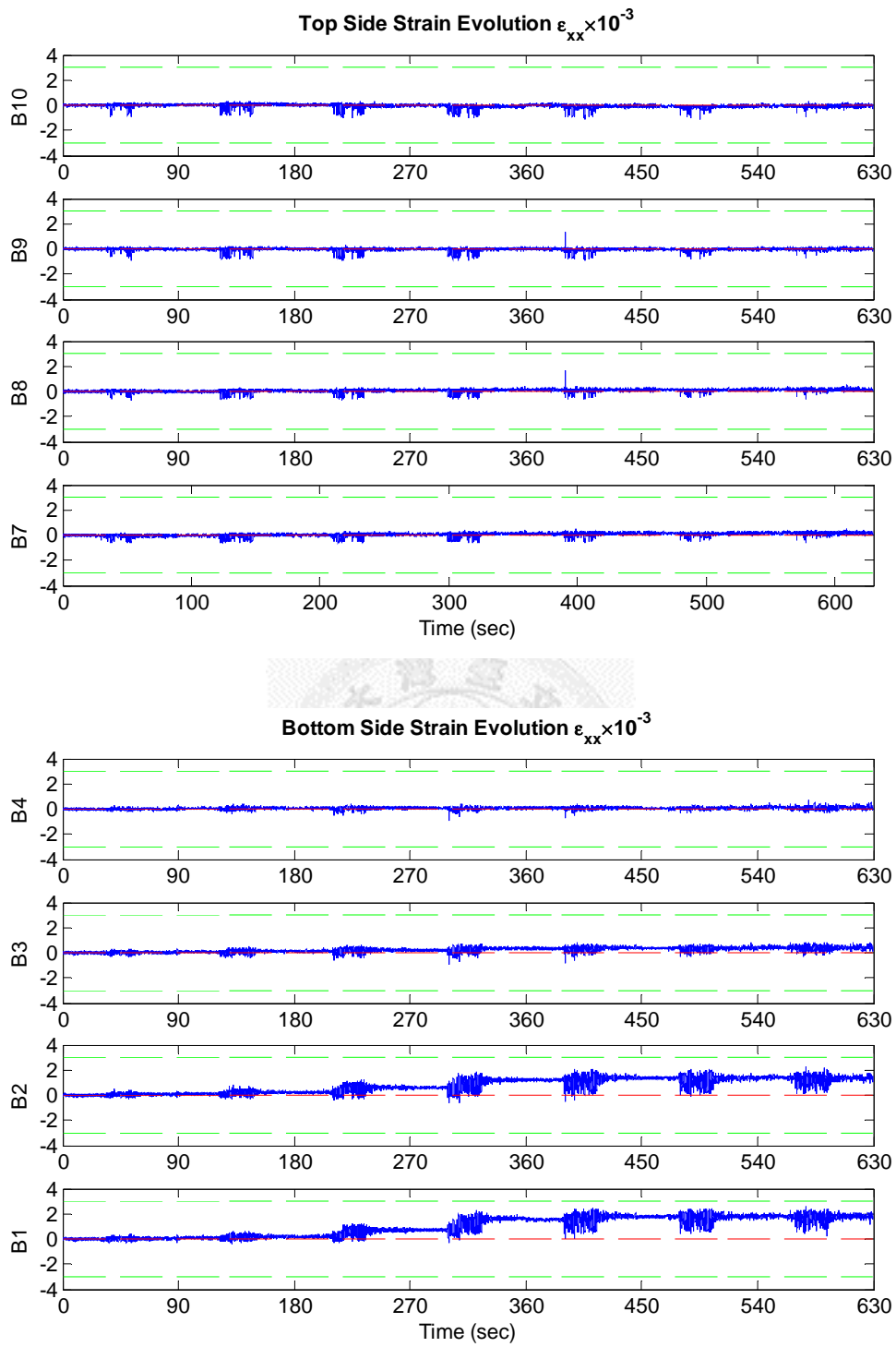
Figure 3-68 Strain field variation from RCF6-1 to RCF6-7, ε_{xx}

119
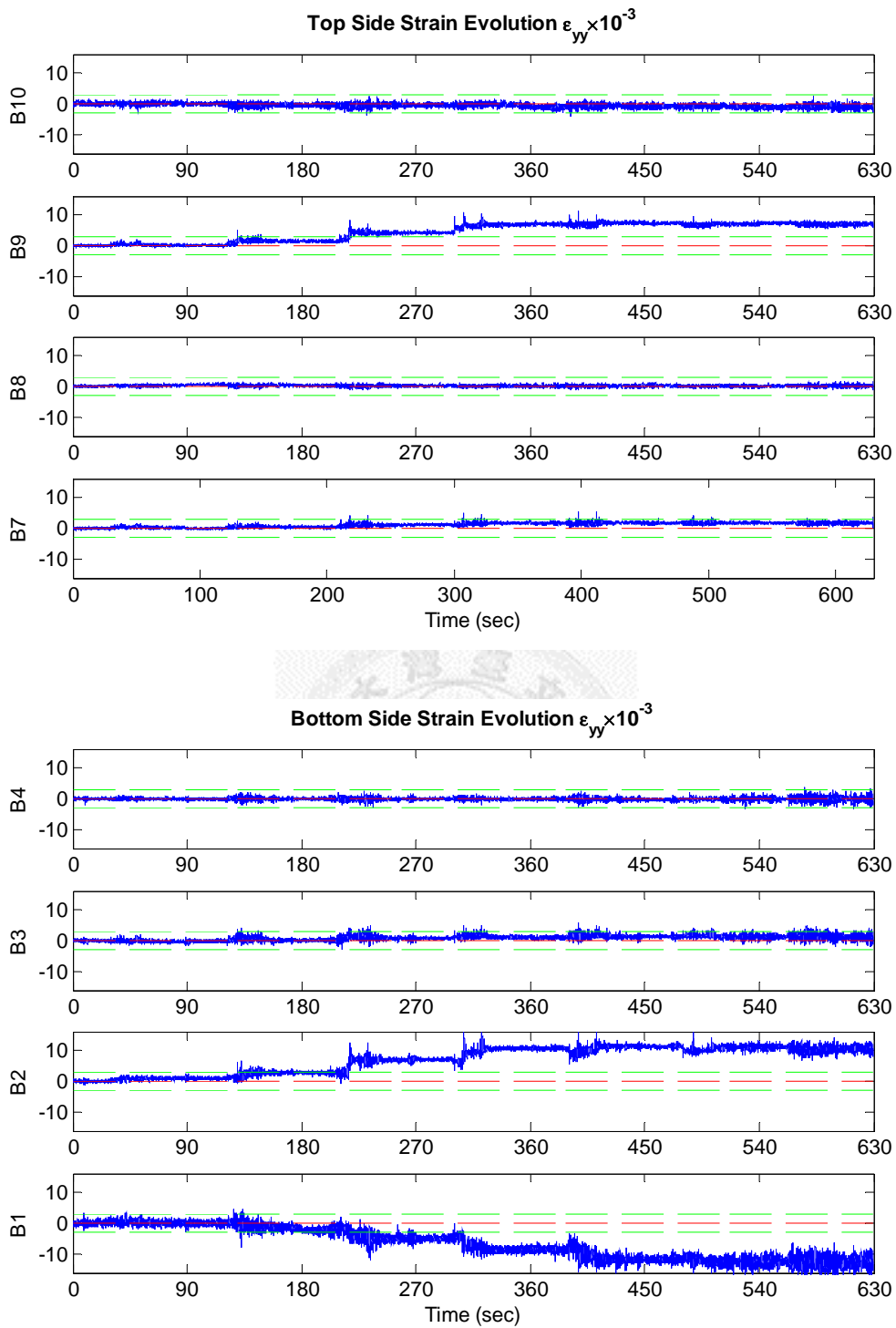
Figure 3-69 Strain field variation from RCF6-1 to RCF6-7, ε_{yy}
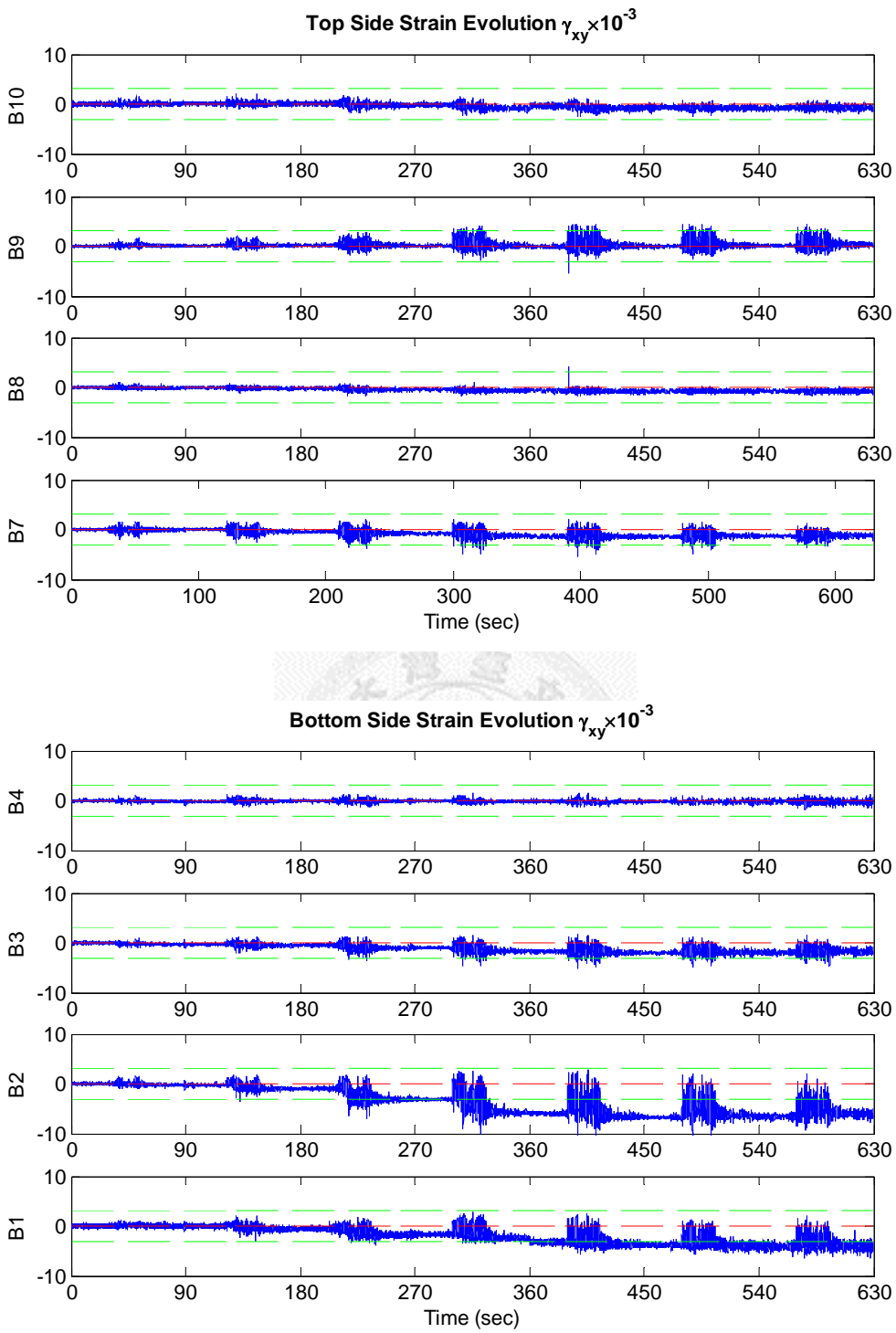
Figure 3-70 Strain field variation from RCF6-1 to RCF6-7, γ_{xy}

121

RCF6-4 (1200gal): Top Side Strain of $\varepsilon_{xx} \times 10^{-3}$

RCF6-4 (1200gal): Bottom Side Strain of $\varepsilon_{xx} \times 10^{-3}$
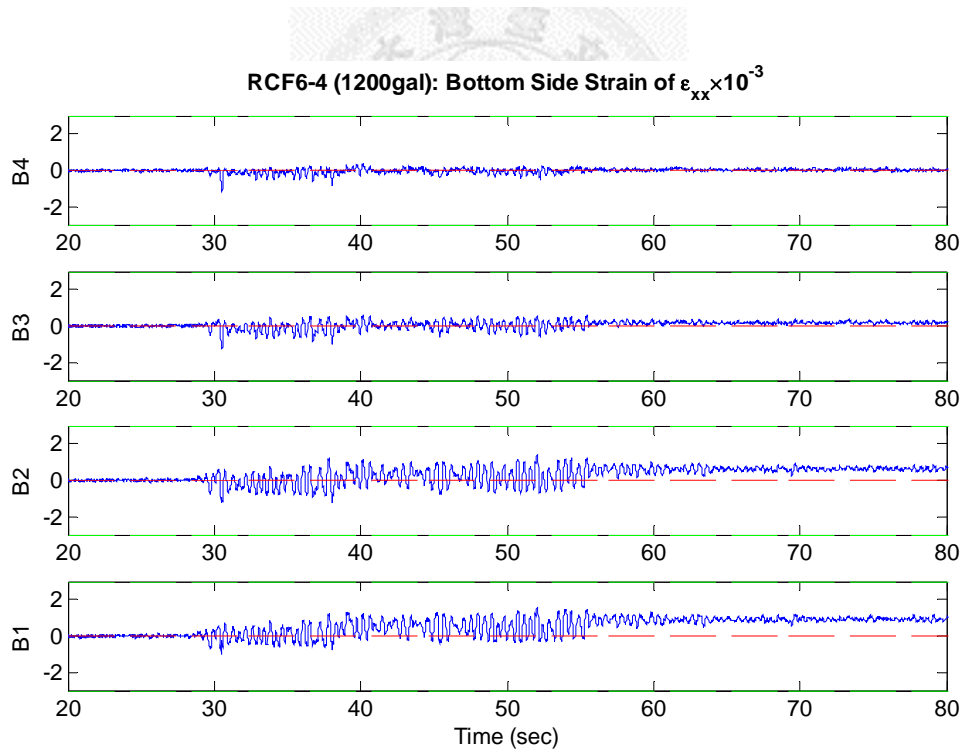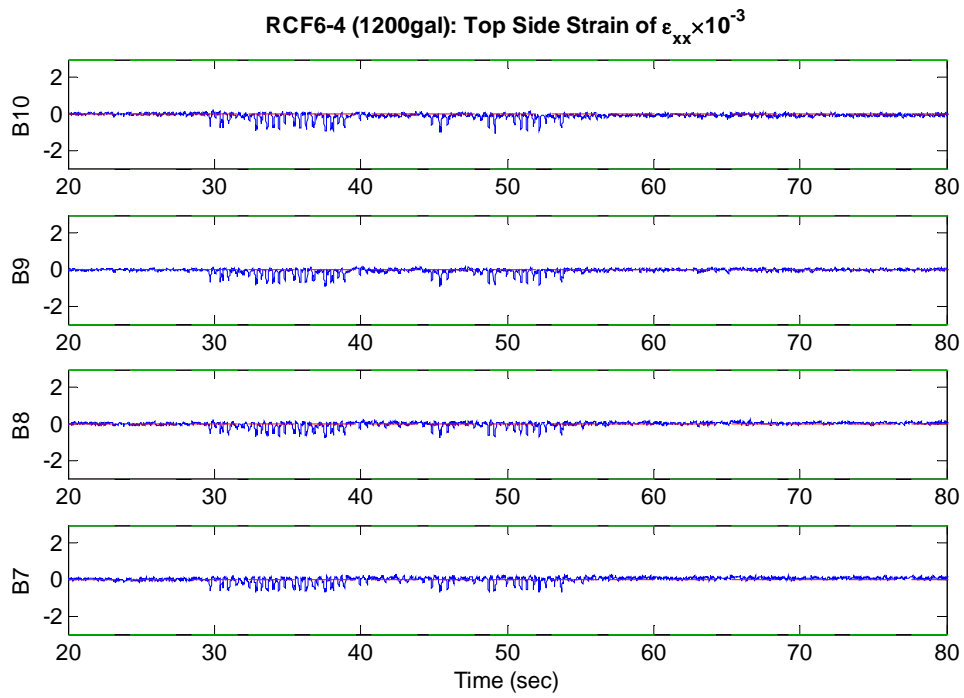
Figure 3-71 RCF6-4 Strain field trend of ε_{xx}
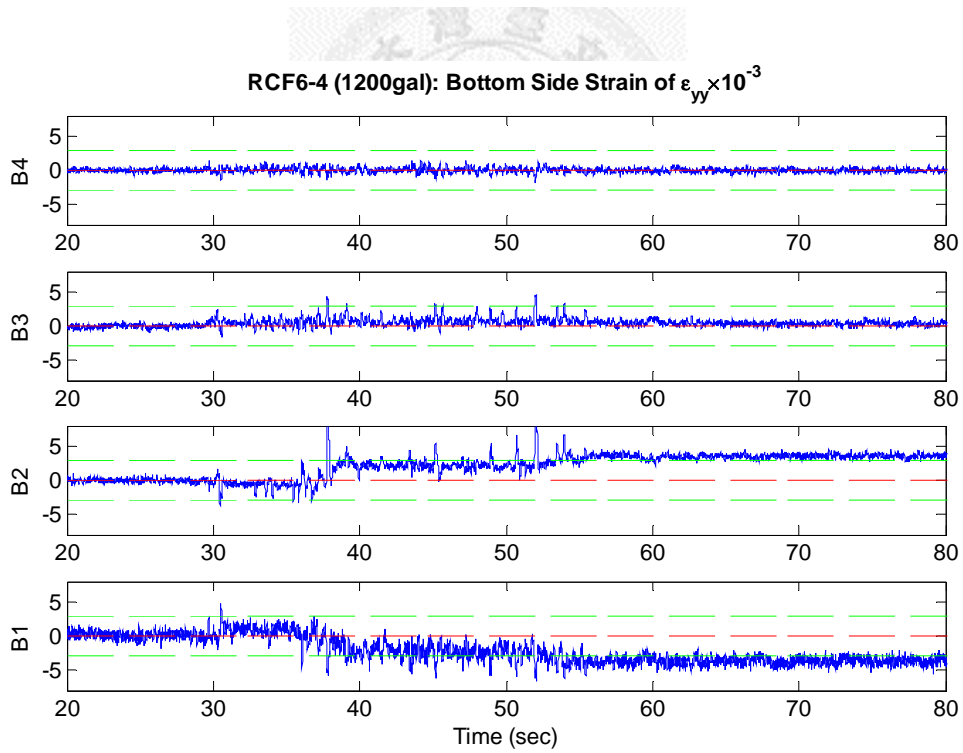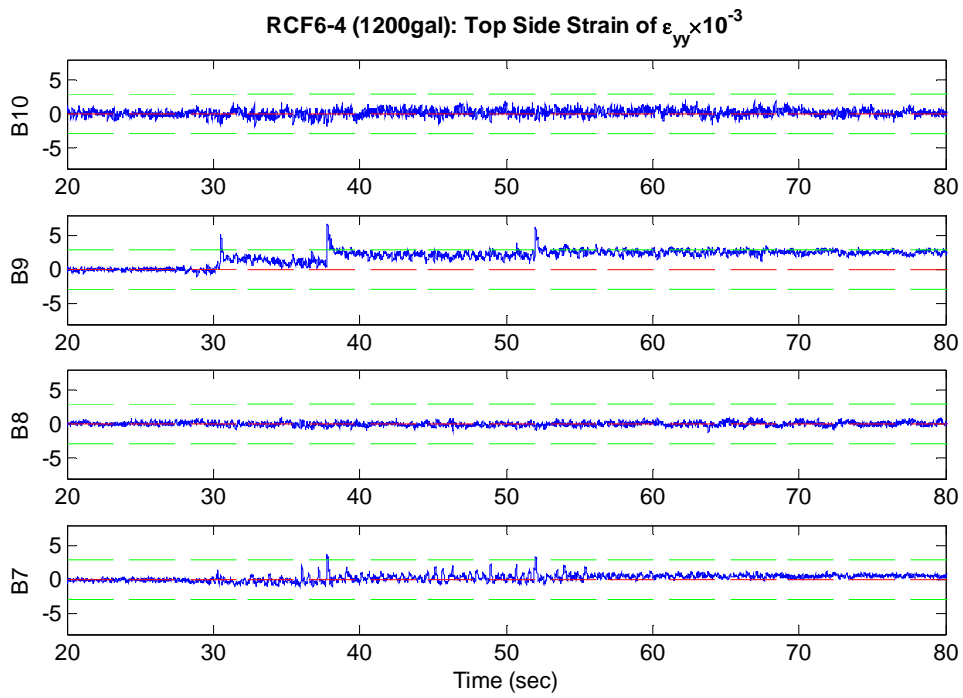
Figure 3-72 RCF6-4 Strain field trend of ε_{yy}
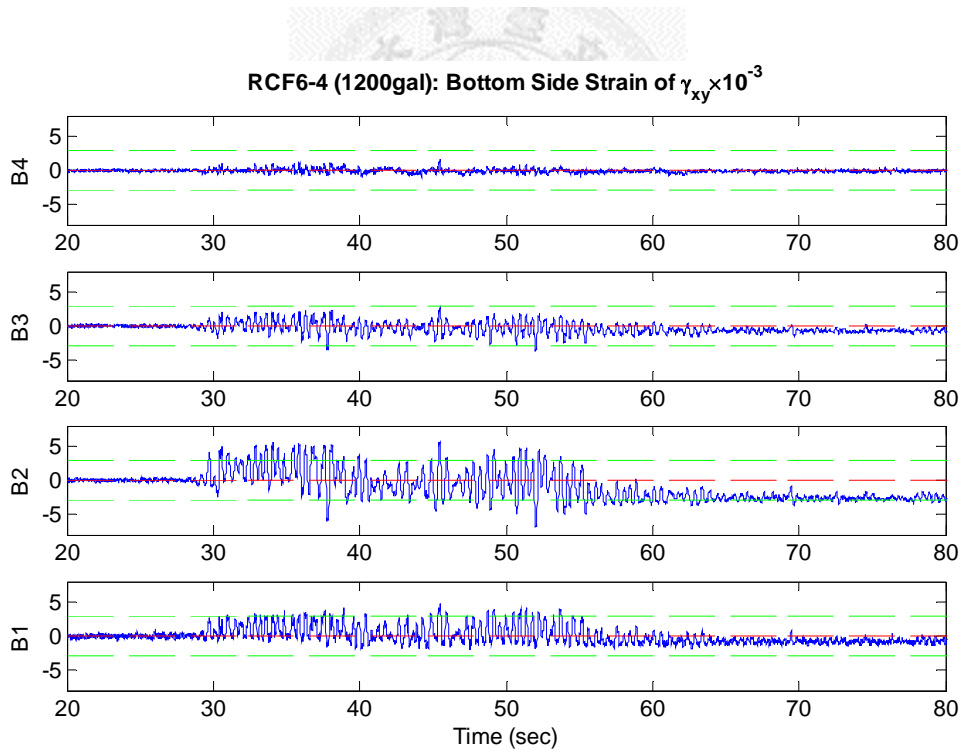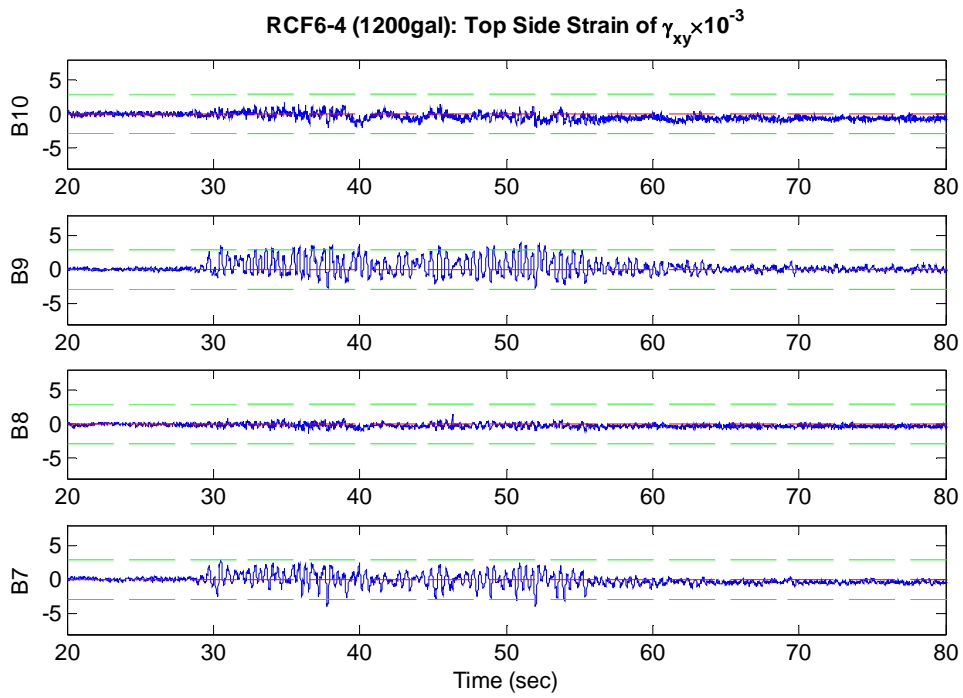
Figure 3-73 RCF6-4 Strain field trend of γ_{xy}
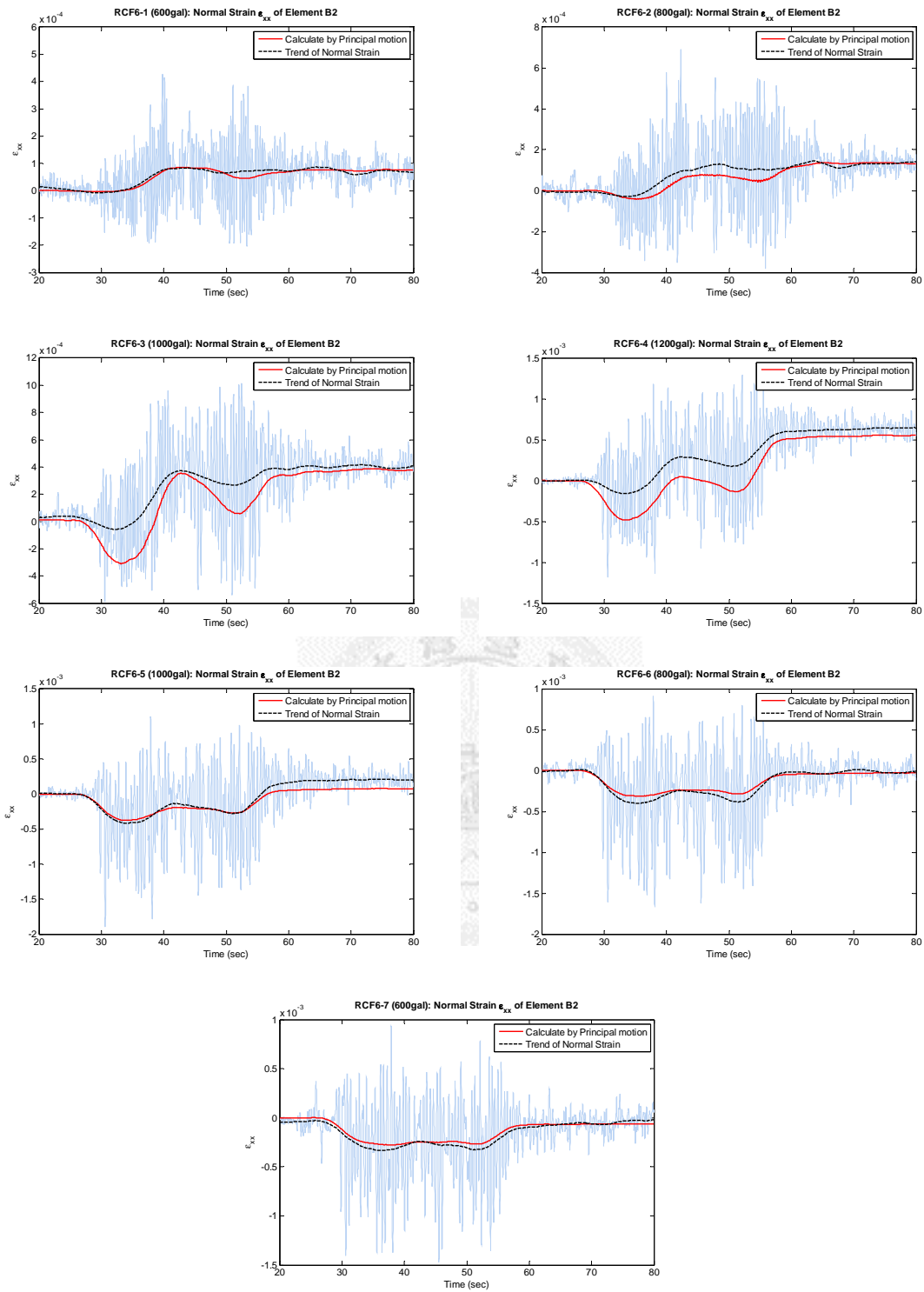
Figure 3-74 Normal strain ε_{xx} tendency approach by principal motion
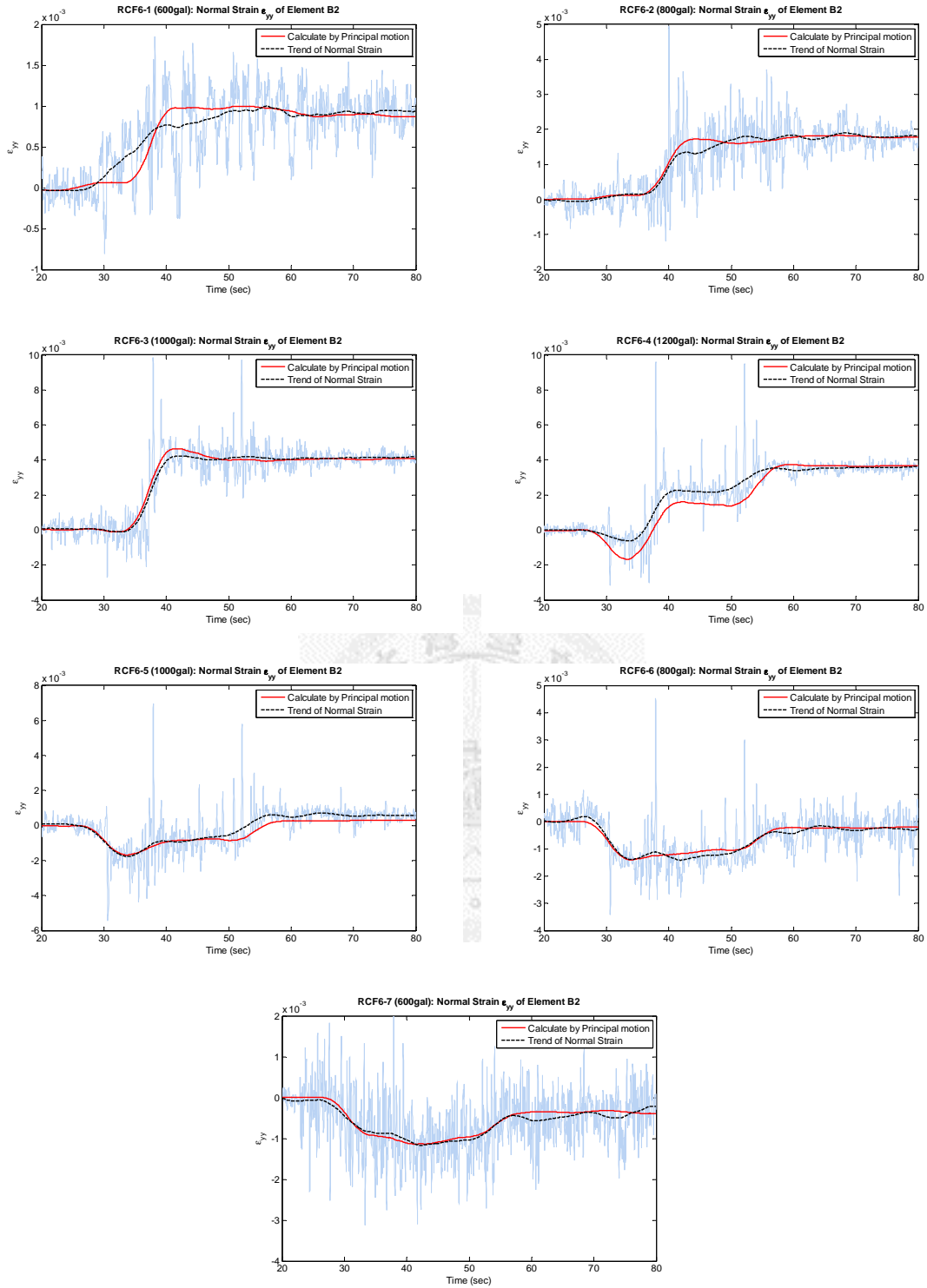
Figure 3-75 Normal strain ε_{yy} tendency approach by principal motion
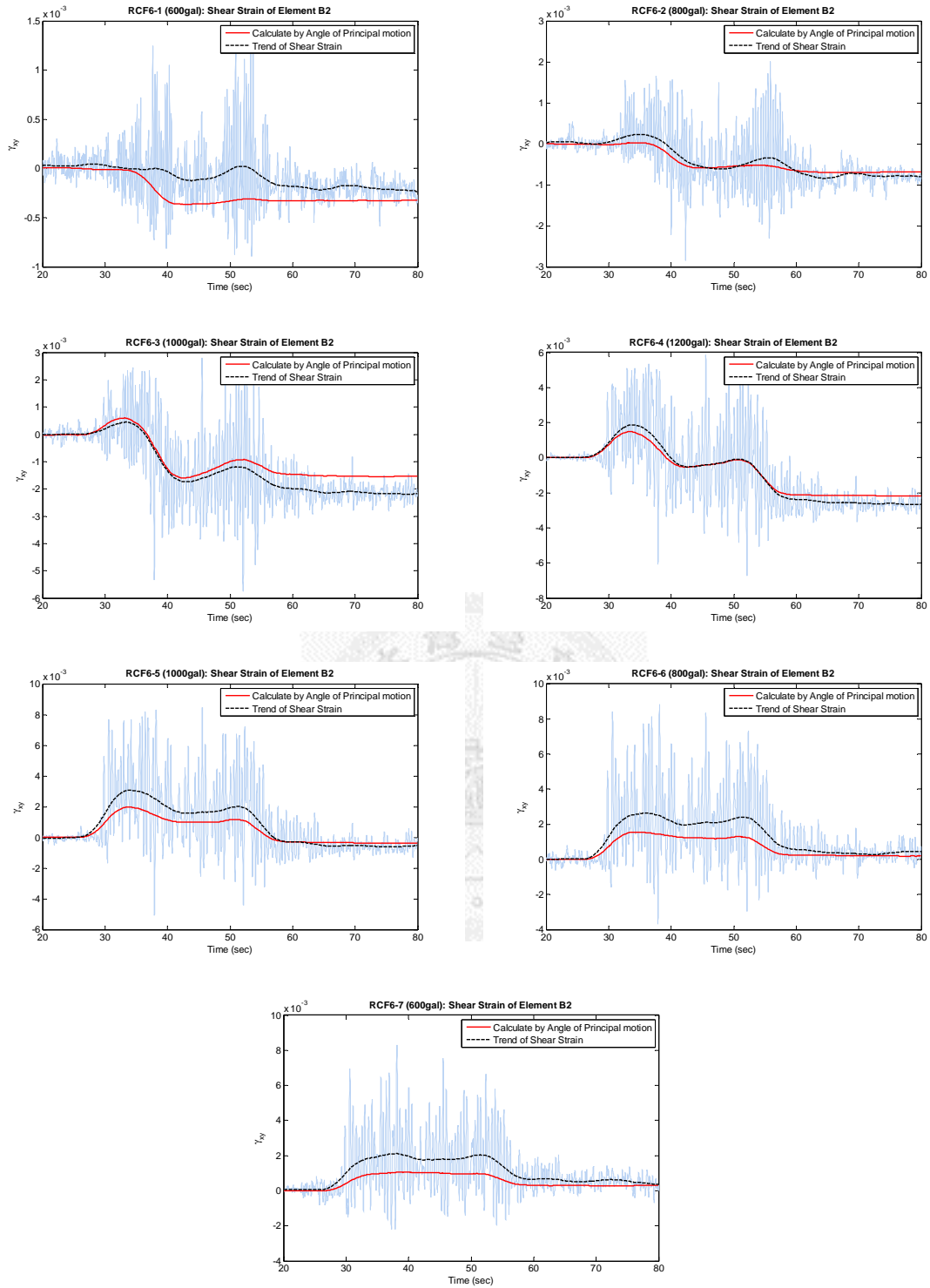
Figure 3-76 Shear strain γ_{xy} tendency approach by principal motion
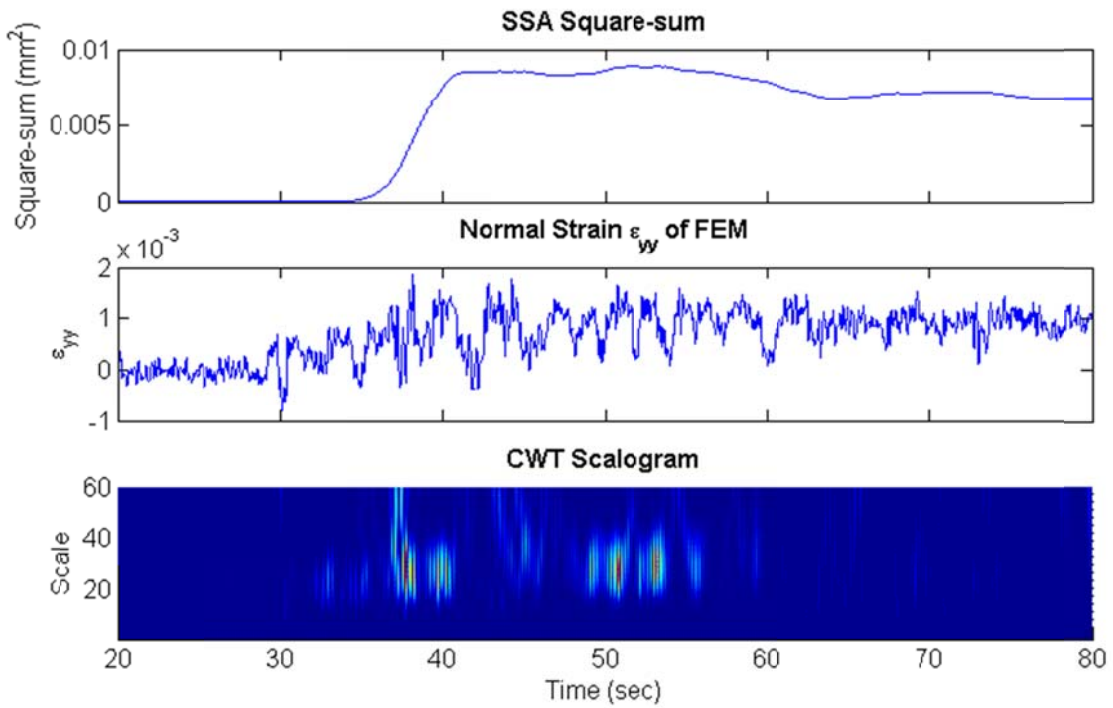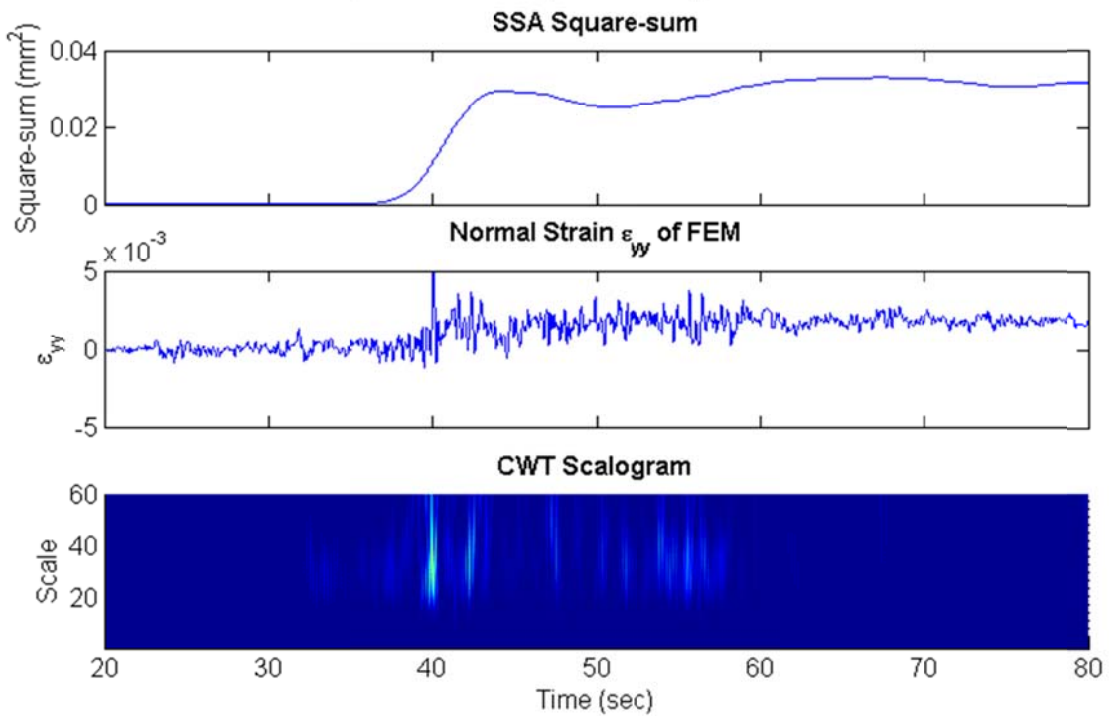
Figure 3-77 Local analysis result comparison (a)
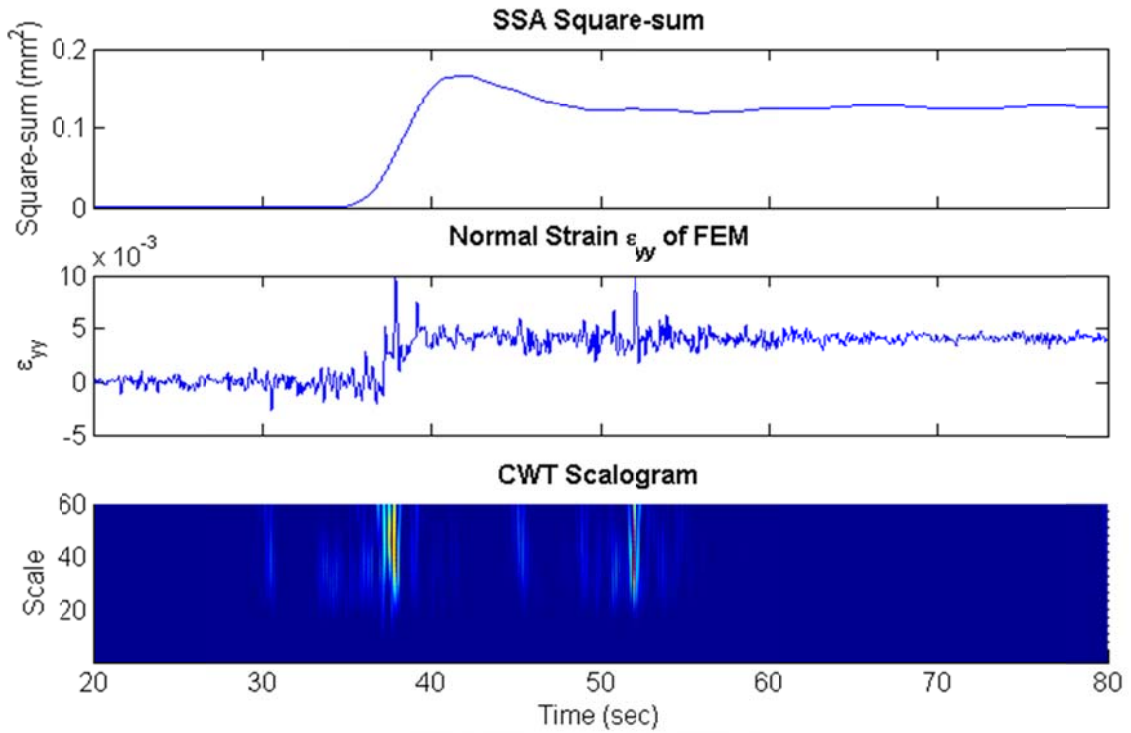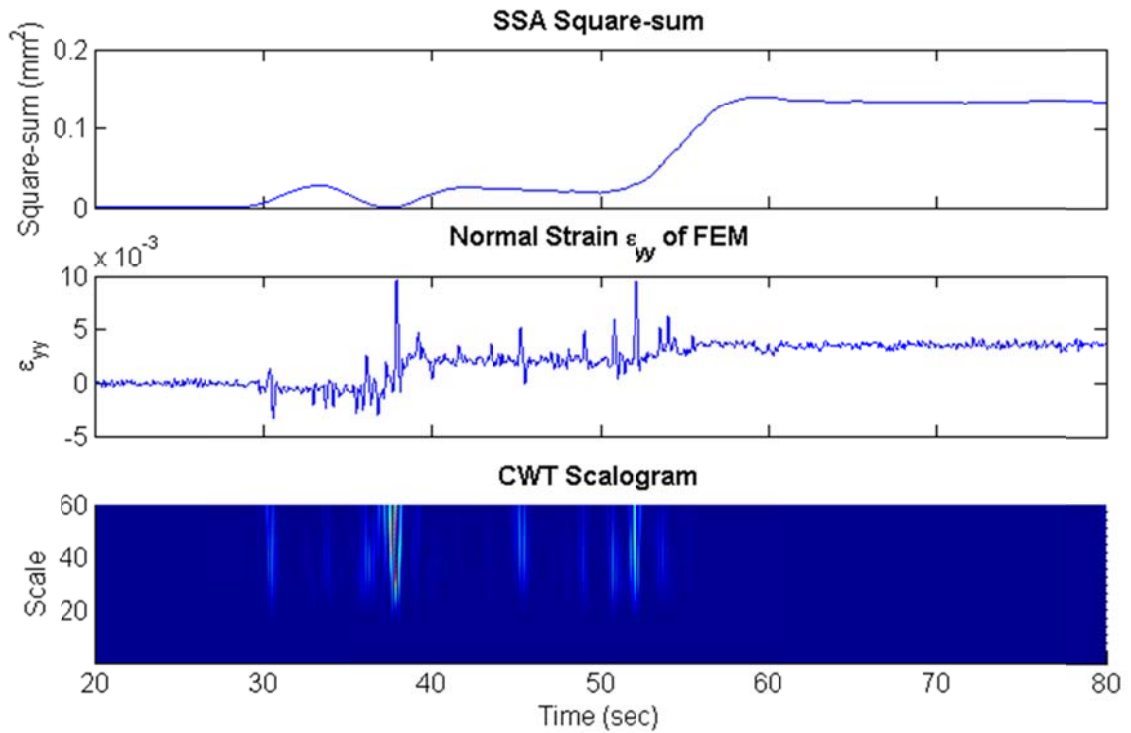
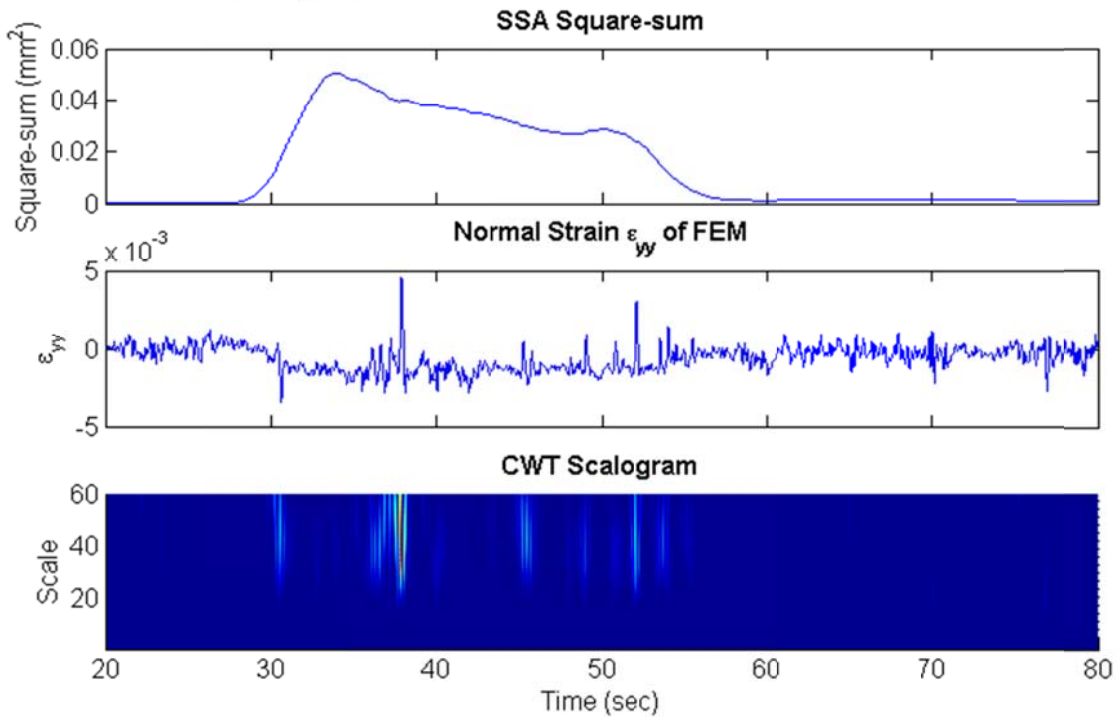Figure 3-78 Element B2 local analysis result comparison (b)

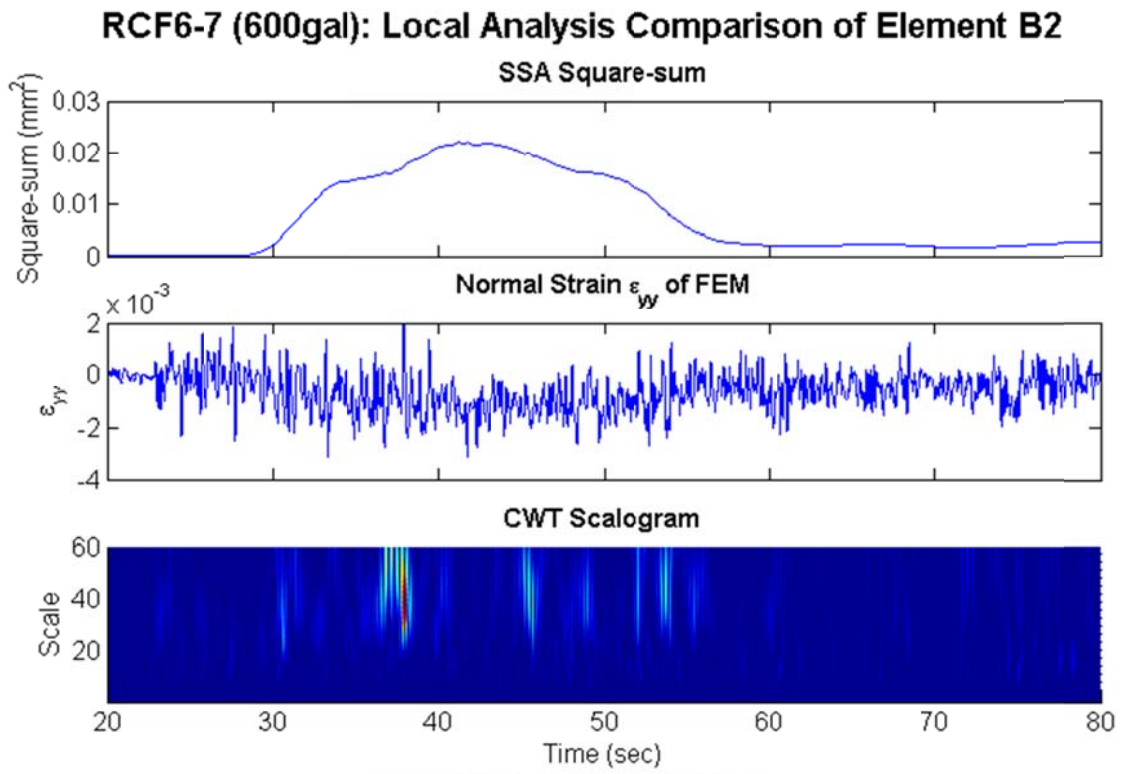129
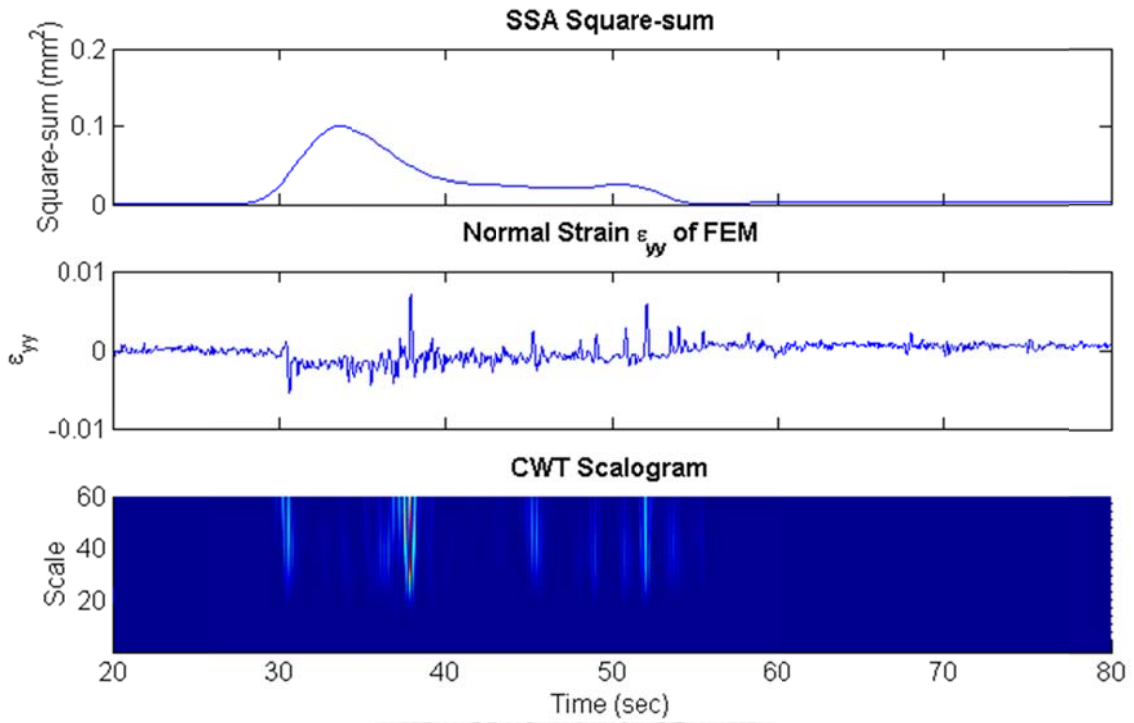
Figure 3-79 Element B2 local analysis result comparison (c)

Figure 3-80 Element B2 local analysis result comparison (d)